Universiteit Gent
Faculteit Ingenieurswetenschappen
Vakgroep Informatietechnologie

Aandrijving van geïntegreerde nanofotonische componenten door middel van de optische gradiëntkracht

Actuation of integrated nanophotonic devices through the optical gradient force

---

Joris Roels

Proefschrift tot het bekomen van de graad van
Doctor in de Ingenieurswetenschappen:
Elektrotechniek
Academiejaar 2010-2011

Universiteit Gent
Faculteit Ingenieurswetenschappen
Vakgroep Informatietechnologie

Promotoren:
Prof. Dr. Ir. Dries Van Thourhout
Prof. Dr. Ir. Bjorn Maes

Examencommissie:

Prof. Dr. Ir. Daniël De Zutter (voorzitter)	UGent, INTEC
Prof. Dr. Ir. Dries Van Thourhout (promotor)	UGent, INTEC
Prof. Dr. Ir. Bjorn Maes (promotor)	UGent, INTEC & UMons
Prof. Dr. Ir. Roel Baets (secretaris)	UGent, INTEC
Prof. Dr. Ir. Wim Bogaerts	UGent, INTEC
Prof. Dr. Ir. Kristiaan Neyts	UGent, ELIS
Prof. Dr. Tobias Kippenberg	Ecole Polytechnique Fédérale de Lausanne
Dr. Ir. Iwijn De Vlaminck	TUDelft

Universiteit Gent
Faculteit Ingenieurswetenschappen

Vakgroep Informatietechnologie
Sint-Pietersnieuwstraat 41, B-9000 Gent, België

Tel.: +32-9-264.34.48
Fax.: +32-9-264.35.93

Proefschrift tot het behalen van de graad van
Doctor in de Ingenieurswetenschappen:
Elektrotechniek
Academiejaar 2010-2011

Dankwoord

NIL volentibus arduum: voor zij die willen is niets lastig. Mijn middelbare schooltijd ligt te ver achter mij om me nog te herinneren welke auteur er in oorsprong verantwoordelijk is voor deze gevleugelde woorden, maar het is wel duidelijk dat de brave man in kwestie absoluut geen kaas moet gegeten hebben van doctoreren. Immers zelfs voor een doctoraatsstudent met ijzeren wil ligt de weg naar de opperste fotonicaroem bezaaid met hinderlagen en intriges, gecamoufleerde slangenkuilen, talrijke lesopdrachten en groepsvergaderingen. Bij een odyssee van dergelijke kaliber hoort uiteraard een ervaren gids. Deze belangrijke rol werd bij mijn doctoraat van in het prille begin ingevuld door Prof. Dries Van Thourhout. Uiteraard wil ik ook mijn dank betuigen aan co-promotor Prof. Bjorn Maes voor zijn belangrijke inbreng in de laatste jaren van het doctoraat.

Echter de meest ervaren fotonicagids in Gent en omstreken is natuurlijk prof. Roel Baets, sinds jaar en dag hoofd van de onderzoeksgroep Fotonica. Vanzelfsprekend was ook zijn invloed op cruciale punten in dit doctoraat niet te onderschatten, bijvoorbeeld toen ik in de zomer van 2009 een beetje in de euh...tang zat. In één adem wens ik ook de rest van de jury (met aan het hoofd voorzitter prof. Daniël Dezutter) en in het bijzonder de resterende leden van de leescommissie (prof. Wim Bogaerts, prof. Kristiaan Neyts, prof. Tobias Kippenberg en dr.ir. Iwijn De Vlaminck) te bedanken voor hun tijd, inzet en feedback. Iwijn verdient zeker een speciale vermelding voor zijn bepalende invloed de eerste twee jaar van het doctoraat. Die periode was voldoende om een toen (we spreken van 2007) nog knettergek idee (om optische krachtwerking aan te tonen op een chip) tot een persoonlijke missie te maken die de rest van mijn doctoraatstijd zou gaan beheersen.

Ook de partners van het 3D-camera project (prof. Maarten Kuijk, prof. Wilfried Philips, Ward, Daniël, Riemer en Ljubomir) verdienen een be-

dankje. De vaardigheden en kennis die ik in dit project tijdens mijn twee eerste doctoraatsjaren kon opbouwen zijn bij mijn later werk goed van pas gekomen.

De experimenten die in dit doctoraat zijn gebeurd zouden volstrekt onmogelijk geweest zijn zonder de noodzakelijke ondersteuning van een heleboel mensen: Steven, Mr. Yu en Liesbet voor de processing, Hendrik en Jeroen voor de metingen, Kristien en Manu voor de IT, de Ilses, Bert, Karien, Eddy en Mike voor het oplossen van talrijke administratieve en andere problemen. Een speciale vermelding in deze categorie is er voor Luc, technieker in hart en nieren die door zijn ervaring met vacuumtechnologie een onmisbaar stukje van mijn doctoraatspuzzel wist te leggen.

Geen inspanning zonder ontspanning natuurlijk, dus verdienen ook de ploegmaats en sympathisanten van volleybalclub JTV Brigand hun plaatsje in dit dankwoord. Volgens een ruwe schatting kom ik hier na 6 jaar toch aan een lijstje dat ergens ver boven de 50 namen afklokt (alfabetisch van Alain to Yves) en waarvoor ik een aparte appendix zou moeten invoeren.

Een andere belangrijke groep van mensen zou ik kort kunnen omschrijven als 'de mannen van het colleesj van Deiremonne' al dekt doorheen de jaren deze vlag al lang de lading niet meer: Kris & Lien & Fé, Els & Jeroen, Joren & Vero, Kris & Klaartje, Tom & Sarah, Lode & Marissa, Bart & Cees, Maarten & Soetkin & Ferre,. Een quizke, een verbodenwoordenspel tijdens een k-tocht met iets te veel j-kes (met of zonder de V), een pokeravondje, een vrijgezellenfuif met bijhorende trouwerij, er gewoon eens tussenuit, een houten paard dat slechts zeer occasioneel eens buitenkomt, een bbq, een gezellige nieuwjaaravond of gewoon maar eens een pintje drinken in den abo: het zijn allemaal dingen die wel eens goed willen helpen om met de gedachten eens niet bij de job te zijn.

Echter het best mogelijke medicijn tegen elke vorm van doctoraatsmoeheid is de open en amicale sfeer die steeds onder de collega's aanwezig is geweest. Ik denk dan bijvoorbeeld aan de mannen van de 'oude garde' die de groep reeds een aantal jaren verlaten hebben, maar in de begindagen steeds voor de ambiance zorgden: Bert, Kris, Ronny, D'Oos, Sam, Joris VC, Gino, Wouter VP, Peter VDS en Reinhard. De 'net iets minder oudezakken garde' nam de fakkel meer dan waardig over: Jonathan, Joost "Allez ho, nog eentje", Peter DB en natuurlijk ook Stijn, mijn voormalige thesisbegeleider die

me in de fotonicawereld heeft binnengeloodst. Samen met enkele mensen die intussen zowat tot het vaste fotonicameubilair zijn gaan behoren (Gunther “Dr. G, touch my *******”, Wim “nog een koffieke boven om af te ronden zeker?”, Peter B en Geert “vaste lunchgezellen in Sint-Jan en Brug met bijhorende maag van beton” en Dirk “deskundige eerste hulp bij meetproblemen”) zorgden ze ervoor dat Katrien “Ain’t no sunshine when she’s gone” en ikzelf in een opperbeste groepssfeer aan ons doctoraatsavontuur konden starten in augustus 2005.

Naast de start van een lovenswaardige traditie om op regelmatige basis ravissante dames aan onze overwegend mannelijke groep toe te voegen was het ook de start van de internationalisering van de groep, ingeluid door “Shank Tank” Shankar. Zijn voorbeeld werd gevolgd door vele Indiërs en Chinezen die stuk voor stuk allemaal kleurrijke namen hadden die ik niet altijd even gemakkelijk uit elkaar kon houden. Eéntje van hen was moedig genoeg om mijn werk rond MEMS diffractieroosters verder te zetten: Sukumar, I was happy to see that the pupil could exceed his master’s MEMS skills by far. Voeg bij dit alles nog een vleugje Spaanse peper “Christina”, Frans temperament “Pauline”, Vietnamese aaibaarheid “Khai-man”, oer-Hollandse gezelligheid “Thijs”, Thaise vrolijkheid “Nannicha”, Servische eruditie “Stevan”, Turkse branie “Gunay”, West-Vlaamsche doortastendheid “Danaë”, Poolse empathie “Kasia”, Iraanse charme “Shahram” en Ethiopische rustige vastheid “Nebiyu” en je krijgt al een vaag idee van het bonte allegaartje aan collega’s dat dagelijks het technicum onveilig maakte.

Bovenstaand recept komt pas goed tot zijn recht met wat jong geweld van eigen bodem. Sam, Thomas, Eva, Peter DH, Martijn, Yannick en Bart. Jullie zijn er nog niet zo lang geleden aan begonnen: keep up the good work en vooral, keep on smiling als het wat minder goed gaat, dat heb ik zelf ook altijd gedaan (ahum). Diedrik “vettig lachske”, Martin “kruip eens onder een tafel door zonder de vloer te raken” en Karel “staalkabel is my middle name” zijn al iets minder jong, maar des te meer geweldig natuurlijk.

Een welgemeende dankuwel ook aan mijn mede-eilandbewoners, willens nillens altijd de dichtsbijzijnde luisterende oren in goede en kwade dagen. Tom, Bram en Pieter, ik zal ons geleuter, gezaag en gezever heel hard missen. In de categorie “volslagen buiten categorie” tot slot horen Lieven en Dave thuis. De gangen van den 41 werden een pak stiller en minder gezellig toen jullie beslisten om andere oorden op te zoeken!

Daarmee heb ik de meeste van de collega's nu wel genoemd denk ik, maar ik kan er ook hier en daar wel een paar vergeten vernoemen zijn. Zo schieten me er in laatste instantie nu ook nog wel een Koen "medebestrijder van meetkamerperikelen in the good old days", Wout "tegengif voor mijn cynisme, maar het pakt precies toch niet altijd even goed", Marie " **** ***** ** ****-*** ;-) ", Elewout "Ik ben niet paranoïa", en Kristof "blond and boring don't go together" te binnen. Alle gekheid op een stokje, jullie zijn elk op jullie eigen manier veel meer geweest dan louter collega's, al slaat dit laatste misschien wel op een heel groot deel van bovenstaande mensen. 5 en een kwart jaar photonics was immers niet zomaar een full time job, het is ook het verhaal van nachtelijke experimenten op adrenaline, pintjes in de Vooruit, kalmerende drukpuntmassages in Turkse en Japanse stijl na alweer een mislukt experiment, chocolates@11, fruits@4, een lichtjes surrealistische avond in een Antalyaanse jacuzzi, beachvolley op de paradijselijke stranden van Mexico, Californië en Florida, een niet-voorpublicatie kalender, een hoofdrol in een fotostrip, een mislukt debuut als charmezanger en romanschrijver, pintjes in de Marimain, een memorabele week op het eiland Elba, radio Fotonica, een mysterieuze geparfumeerde brief op mijn bureau, een ongewenst nat pak in Roel's zwembad (x2), gewoon zomaar een feestje (x37), een ontroerend afscheidsfilmpje, who took my circulator?, nog veel meer chocolates@11, nasi-rollen in de Brug, een koppige kokosnoot, een terrasje aan de Gruut, who took my temperature cable?, een fietstocht richting Antwerpen die niet lang genoeg kon duren, een glaasje van plezier bij Filliers en een rits brouwerijbezoekjes, een kerstboompje versierd met wel heel speciale balletjes en zo veel meer herinneringen die maken dat ik mijn verblijf in Gent nooit zal vergeten.

Tot slot nog een woord van dank aan de familie: broer Jonas, zus Sophie, schoonbroer Kevin en uiteraard bengels Lucas en Casper (die —godzijdank— dat hele doctoraatsgedoe maar niets vinden en liever verstoppertje spelen) en uiteraard ook ma en pa. Dit boekje waar jullie vermoedelijk de toeten of blazen van begrijpen was niet mogelijk geweest zonder 29 jaar onophoudelijke steun.

Het is een behoorlijk uit de kluiten gewassen dankwoord geworden, maar op een manier zal het toch nooit helemaal compleet zijn, denk ik. Nog eens bedankt voor alles, het is hoog tijd nu om letterlijk en figuurlijk een nieuw hoofdstuk te beginnen.

Adios!

Gent, maart 2011
Joris Roels

Table of Contents

List of Figures

List of Tables

List of Acronyms

A

AC	Alternating Current
AFM	Atomic Force Microscopy
ASE	Amplified Spontaneous Emission

B

BHF	Buffered Hydrofluoric Acid
BOx	Buried Oxide Layer

C

CMOS	Complimentary Metal Oxide Semiconductor
CPD	Critical-Point-Drying
c-Si	(mono)crystalline Silicon
CW	Continuous Wave

D

DBR	Distributed Bragg Reflector
DC	Direct Current

DMD	Digital Micromirror Device
DSD	Displacement spectral density
DUT	Device under test
DUV	Deep-Ultra-Violet

E

EDFA	Erbium doped fiber amplifier
EOM	Electro-optic modulator
ESA	Electrical spectrum analyzer

F

FCA	Free carrier absorption
FSD	Force spectral density
FSR	Free spectral range
FP	Fabry-Pérot
FWHM	Full Width at Half Maximum

G

GLV	Grating Light Valve

H

HF	Hydrofluoric Acid
HMDS	Hexa-Methyl-Disilizane

I

IPA	Isopropyl Alcohol

L

LPCVD	Low Pressure Chemical Vapor Deposition

M

MEMS	Micro-Electro-Mechanical Systems
MMI	Multi-Mode Interferometer
MOEMS	Micro-Opto-Electro-Mechanical Systems
MOMS	Micro-Opto-Mechanical Systems
MZI	Mach-Zehnder Interferometer

N

NEMS	Nano-Electro-Mechanical Systems
NEP	Noise Equivalent Power
NOEMS	Nano-Opto-Electro-Mechanical Systems
NOMS	Nano-Opto-Mechanical Systems

O

OBF	Optical Bandpass Filter

P

PECVD	Plasma-Enhanced Chemical Vapor Depostion

PSD	Power spectral density

Q

Q-factor	Quality factor

R

RIE	Reactive Ion Etching
rtHz	Root Hertz $\sqrt{Hz}$

S

SEM	Scanning Electron Microscope
SI	Système International d'unités
SNR	Signal-to-noise ratio
SOI	Silicon-on-Insulator

T

TE	Transverse Electric
TLS	Tunable Laser Source
TM	Transverse Magnetic
TPA	Two Photon Absorption

Nederlandse samenvatting –Summary in Dutch–

Situering van het doctoraatsonderzoek

De tak van de wetenschap die fotonica genoemd wordt, spitst zich toe op de generatie, transmissie, modulatie, versterking, detectie en het doorschakelen van licht. Fotonica bestrijkt een heel breed toepassingsgebied, variërend van de meest geavanceerde technologische applicaties tot alledaagse gebruiksvoorwerpen.

Gedurende de laatste decennia is de precieze controle en manipulatie van licht een dagelijkse uitdaging geworden voor vele wetenschappers en ingenieurs wereldwijd. Voor al deze toepassingen is er op een of andere manier nood aan componenten die interageren met licht en het op een gecontroleerde manier manipuleren (lenzen, spiegels, modulatoren, etc.). Dikwijls is er ook actieve functionaliteit vereist waarmee we bedoelen dat de eigenschappen van de optische component op een gecontroleerde manier kunnen gewijzigd worden in de tijd via een externe stimulus.

Componenten van sub-mm afmetingen die mechanisch aangestuurd worden door een externe stimulus worden Micro-Elektro-Mechanische systemen (MEMS) genoemd. MEMS die ingezet worden om licht te manipuleren worden Micro-Opto-Elektro-Mechanische systemen (MOEMS) genoemd. Een voorbeeld van zo een MOEMS wordt getoond in Fig. 1a. Het spiegeltje kan geroteerd worden door een elektrische spanning aan te leggen.

In parallel met de voortdurende miniaturisatie in de de elektronica (resulterend in meer transistoren per chip en dus krachtigere chips), zien we dat ook in de wereld van de MOEMS naar een nog verder doorgedreven miniaturisatie wordt gestreefd. Men spreekt in dat verband ook van Nano-Opto-Elektromechanische Systemen (NOEMS).

In dit werk zijn we nog een stap verder gegaan en hebben we een op-

Figuur 1: **a**, 2D-matrix van verdraaibare microspiegeltjes. Eén van de spiegeltjes bevindt zich in de 'actieve' geroteerde toestand. (foto van Sandia National Laboratories), Een microdeeltje, gevangen in het centrum van een laserspot.

portuniteit onderzocht die gecreëerd werd precies door deze miniaturisatie. Klassieke MOEMS manipuleren enkel het licht, de beweging die benodigd is voor actieve functionaliteit moet verricht worden door middel van een externe (niet-optische!) kracht. Wij zijn op zoek gegaan naar componenten waar het licht zelf voor de externe stimulus zorgt die beweging mogelijk maakt. Dit is een extreem uitdagende opdracht want de stralingsdruk die licht uitoefent is in principe zeer klein. Toch hebben we met ons werk kunnen aantonen dat onder bepaalde omstandigheden optische aandrijfkrachten voor zeer kleine componenten op een chip geen utopie zijn. We kunnen dus spreken over Micro-Opto-Mechanische-Systemen (MOMS) of zelfs Nano-Opto-Mechanische systemen (NOMS).

Optische krachten worden momenteel al toegepast om microdeeltjes te manipuleren zoals levende cellen, DNA en bacteriën. Men spreekt in dat verband ook van een 'optisch pincet' (zie Fig. 1b). De krachten die in deze experimenten optreden zijn voorbeelden van *gradiëntkrachten*. Het interessante aan gradiëntkrachten is dat de uitgeoefende kracht niet alleen schaalt met het optische vermogen van de laser, maar ook met de gradiënt van het veld. Dit laat ons toe om relatief sterke krachtwerking te creëren met beperkt optisch vermogen. Bij klassieke stralingsdruk schaalt de grootte van de optische kracht immers met $\frac{P}{c}$ (P het optisch vermogen, c de lichtsnelheid) en kunnen we dus enkel het optisch vermogen verhogen om meer kracht op te wekken. Echter bij een optische gradiëntkracht zal de krachtwerking bij gelijk optisch vermogen toch groter worden als de intensiteit sterker varieert over kortere afstand.

In het bijzonder in het nabije veld van golfgeleiders die licht transporteren treffen we sterke veldgradiënten aan wat ons een unieke moge-

lijkheid biedt om af te rekenen met de relatieve zwakheid van stralingsdruk gerelateerde krachten. Het fysisch principe dat de kracht veroorzaakt is hierbij zeer gelijkaardig aan dat van het optisch pincet.

Aan dit nieuwe onderzoeksdomein wordt soms ook de naam 'optomechanica' toegekend. Het is in dit domein dat wij experimenteel baanbrekend pionierswerk hebben verricht, voortbouwend op eerdere theoretische voorspellingen. We hebben hierbij voorgebouwd op de stevige basis in silicium nanofotonica die reeds aanwezig was in de Onderzoeksgroep Fotonica. Omdat de sterkste optische krachtwerking gevonden wordt op afstanden van de nanofotonische golfgeleider die typisch kleiner zijn dan de golflengte van het licht was bij de fabricage van NOMS nanometer precisie nodig. In feite kunnen we dus stellen dat ons onderzoek naar NOMS een sterk multidisciplinair karakter vertoont en dus kennis van mechanica, nanotechnologie en uiteraard fotonica vergt. Het multidisciplinaire karakter van optomechanica wordt schematisch weergegeven in Fig. 2.

Toepassingen

Op fundamenteel wetenschappelijk gebied kan de optomechanica op relatief korte termijn interessante resultaten opleveren. Als er een sterke optomechanische interactie is, kan licht mechanische energie onttrekken aan een trillende structuur. Men spreekt in dat verband ook van 'optisch koelen'. Een trillende structuur die voldoende wordt afgekoeld gaat dan quantummechanisch gedrag vertonen dat normaliter alleen observeerbaar is in zeer kleine systemen zoals atomen en molecules. De optomechanica zou dus een aantal experimentele tests van de theorie van de quantummechanica kunnen opleveren.

Vanuit ingenieursstandpunt zijn we echter veeleer geïnteresseerd om de optische krachtwerking meer direct te gebruiken als alternatief aandrijfmechanisme voor geïntegreerde MOEMS. Optomechanica zou bijvoorbeeld een rol kunnen spelen bij de realisatie van een volledig optisch netwerk. Met behulp van NOMS kunnen immers optische filters en switches gemaakt worden die optisch reconfigureerbaar zijn.

Echter de meest voor de hand liggende toepassing kan waarschijnlijk gevonden worden in de wereld van de RF-MEMS oscillatoren. Deze dienen als klok voor een geïntegreerd elektronisch circuit of elke andere applicatie die een onafhankelijk tijdsreferentie nodig heeft (horloges of mobiele telefoons). Andere mogelijke toepassingen zijn smalbandige RF-filters en

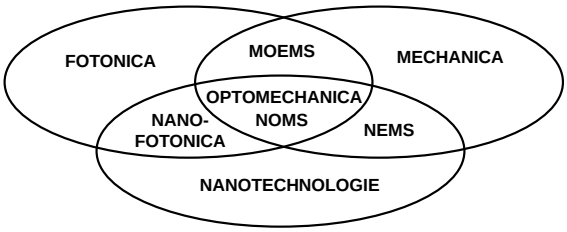

Figuur 2: Nano-Optomechanische componenten (NOMS) zijn het resultaat van de kruisbestuiving van 3 onderzoeksdomeinen: mechanica, nanotechnologie en fotonica.

uiterst gevoelige kracht-, massa- of verplaatsingssensoren.

Experimentele resultaten

Om krachtwerking op een golfgeleider te kunnen waarnemen plaatsen we een tweede ondergeëtste golfgeleider in parallel die zich in het evanescente veld van de eerste bevindt. Hierdoor vindt er koppeling tussen beide plaats en krijgen we in feite een directionele koppelaar. Dit fenomeen laat ons meteen toe om trillingen van de golfgeleiders te registreren. Immers zal een trilling de koppeling tussen beide golfgeleiders veranderen wat resulteert in een modulatie van een doorgaand optisch probesignaal. Dit modulatiesignaal zal zich dan bevinden op de frequentie van de mechanische trilling. Het kan bestudeerd worden met een oscilloscoop of elektrische spectrum analyzer nadat het optisch signaal werd omgezet in een elektrisch signaal met behulp van een fotodetector.

Het is op deze manier zelfs mogelijk om de browniaanse trilling van de ondergeëtste golfgeleiders op te pikken. Deze trilling ontstaat doordat de atomen in het materiaal onder invloed van temperatuur voortdurend trillen en dit resulteert uiteindelijk in een chaotische trilling van de golfgeleiders. Deze chaotische trilling kan echter wel perfect gebruikt worden om de optische kracht te calibreren omdat gemakkelijk kan berekend worden hoe groot de browniaanse trilling gemiddeld is.

Nu we trillingsdetectie en een calibratiemechanisme hebben kunnen we de optische krachtwerking tussen de golfgeleiders bestuderen. Twee single-mode golfgeleiders in parallel resulteren in feite in een bimodaal systeem (waarbij we alleen modes beschouwen met hun belangrijkste elektrisch

veld component parallel met het substraat): we hebben een symmetrische en een antisymmetrische mode.

De krachten die deze modes genereren op de golfgeleider kunnen op verschillende manieren berekend worden. De kennis van de velden op een oppervlak dat de golfgeleider volledig omsluit volstaat. Het resultaat van zo een berekening wijst uit dat de symmetrische mode een uitsluitend attractieve kracht genereert tussen twee parallelle golfgeleiders (per conventie negatieve waarden voor attractieve kracht). De antisymmetrische mode kan ook een repulsieve kracht opleveren voor voldoende grote afstanden.

Om attractieve en repulsieve kracht waar te nemen moeten we dus beide modes gecontroleerd exciteren. Daarom hebben we in dit werk een component ontwikkeld die afhankelijk van de golflengte de symmetrische, de antisymmetrische mode of een superpositie van beiden genereert.

Omdat de optische krachten toch nog relatief klein zijn wordt ook nog resonante excitatie toegepast. De ondergeëtste golfgeleiders kunnen we eigenlijk beschouwen als balken of snaren met een welbepaalde basisresonantiefrequentie. We zullen met behulp van de optische krachten deze snaren als het ware aanslaan op hun resonantiefrequentie. Het lichtsignaal dat de kracht uitoefent (pomp laser) moet dan wel gemoduleerd worden op de resonantiefrequentie van de snaar. Om deze reden is er ook een elektro-optische modulator in de experimentele set-up werd opgenomen. Omdat gasmolecules de beweging te sterk dempen wordt de component in een vacuümklok geplaatst voor karakterisatie (zie Fig. 3a).

Uiteindelijk konden we dan de optische krachtwerking tussen de golfgeleiders opmeten en calibreren. Het finale resultaat wordt getoond in Fig. 3b. We zien inderdaad dat de kracht met behulp van de golflengte afgesteld kan worden van aantrekkend tot afstotend en dat tussenin modesuperposities gevonden worden die tot een nulkracht leiden. Ook de kwantitatieve overeenkomst met de theorie is uitstekend. Dit resultaat kan beschouwd worden als een belangrijke doorbraak en werd dan ook gepubliceerd in het wetenschappelijke tijdschrift Nature Nanotechnology.

We hebben ook onderzocht hoe de optische kracht kan versterkt worden. Een voor de hand liggende optie was het inbouwen van de ondergeëtste golfgeleider in een optische resonator. We hebben met behulp van een racetrack resonator inderdaad kunnen vaststellen dat de optomechanische interactie versterkt wordt met de finesse van de optische resonator. Een andere interessante piste is het gebruik van sleufgolfgeleiders. Dit type golfgeleiders vertoont een klein gleufje (=slot) waarin het licht sterk geconcentreerd wordt. Onze experimenten tonen aan dat de krachtwerking tot 25

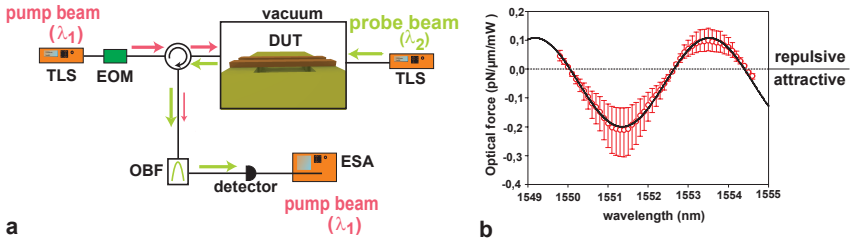

Figuur 3: **Set-up en meetresultaat met attractieve en repulsieve kracht.** **a**, Volledige set-up. Het device-under-test (DUT) wordt in een vacuümklok geplaatst om demping van trilling door lucht weg te nemen. Er zijn twee tunable laser sources (TLS), één pump en één probe laser. Het pompsignaal wordt gemoduleerd met behulp van een elektro-optische modulator (EOM) om resonante excitatie van de golfgeleidersnaren mogelijk te maken. Het probesignaal dat de trilling registreert, wordt na passage door een optisch bandpasfilter (OBF) gedetecteerd met een optisch detector en diens elektrisch uitgangssignaal wordt uiteindelijk met een elektrische spectrum analyzer (ESA) geanalyseerd. **b**, Opgemeten kracht in functie van de golflengte. We zien dat de kracht varieert van zuiver attractief naar zuiver repulsief in perfecte overeenstemming met de theorie.

keer groter is vergeleken met de parallelle golfgeleiders die we gebruikt hebben in het experiment met de aantrekkende en afstotende kracht.

English summary

Introduction

The branch of science that is called photonics is focused on the generation, transmission, modulation, amplification, detection and switching of light. Photonics is covering a broad range of applications, varying from extremely advanced technological applications to common tools.

During the last decades the precise control and manipulation of light has become a daily challenge for many scientists and engineers around the world. For all these applications components that interact with light in a controlled way are required (for examples lenses, mirrors, modulators). Very often also some kind of active functionality is desired, meaning that the properties of light (intensity, phase) can be changed in time through an external stimulus.

Components of sub-mm size that are actuated mechanically through an external stimulus are referred to as Micro-Electro-Mechanical Systems (MEMS) in literature. MEMS that are used to manipulate light are commonly called Micro-Opto-Electro-Mechanical Systems (MOEMS). In parallel with the miniaturization encountered in electronics (resulting in more transistors and hence more powerful and cheaper computer chips) we also see that in the realm of MOEMS there is a tendency to miniaturize mechanical components. Consequently one also finds the term Nano-Electro-Optical-Mechanical Systems in the literature.

In this work we went one step further and we looked into an opportunity that is created through this miniaturization. Classical MOEMS manipulate the light, where the movement that is needed for active functionality is provided by means of an external (not-optical) force. We have investigated components where light itself enables the required movement. This task is extremely challenging because radiation pressure effects in general tend to

be extremely small. Nevertheless we have demonstrated that under certain circumstances optical actuation forces on a chip are not a utopia.

Optical forces are already widely applied to manipulate microparticles such as living cells, DNA and bacteria. In this context the term 'optical tweezer' is frequently encountered. Interestingly gradient forces do not only scale with optical power, but also with the gradient of the electric field. As an important consequence it is possible to create relatively large forces for only modest optical powers. When considering classical radiation pressure effects the magnitude of the optical force simply scales with $\frac{P}{c}$ (P is the incident optical power, c is the velocity of light). In this case we can only increase the optical power to increase the exerted force. Gradient forces offer an extra degree of freedom and provide a larger force (for equal optical power) when the intensity varies more strongly over a shorter distance. Since in the near field of light transporting waveguides strong field gradients are encountered we have discovered a unique opportunity to counter the relative weakness of light forces. The physical principle that causes the gradient forces in optical waveguides is very similar to the gradient forces encountered in optical tweezers.

The research domain that investigates optical forces is often called optomechanics in the literature. In this domain we have made a significant contribution by demonstrating optical forces in a nanophotonic integrated circuit. These nanophotonic circuits have been fabricated through a silicon-on-insulator platform and using Deep-Ultra-Violet lithgraphy, thereby exploiting the core knowledge of the Photonics Research Group.

Because the strongest optical forces are found at a distance from the nanophotonic waveguide that is smaller than the wavelength of light nanoscale fabrication techniques are required. In fact optomechanics on a chip is a multi-disciplinary field that requires profound knowledge of mechanics, nanotechnology and photonics. The multi-disciplinary character of the field is illustrated in Fig. 4.

Applications

On the short term optomechanics will yield breakthroughs at the fundamental scientific level. In case we have sufficiently strong optomechanical interaction, light is able to extract energy from a vibrating structure. This process is referred to as 'optical cooling'. If a vibrating structure is cooled to a sufficiently low temperature it exhibits quantummechanical behavior, which is normally only observed in very small systems such as atoms and

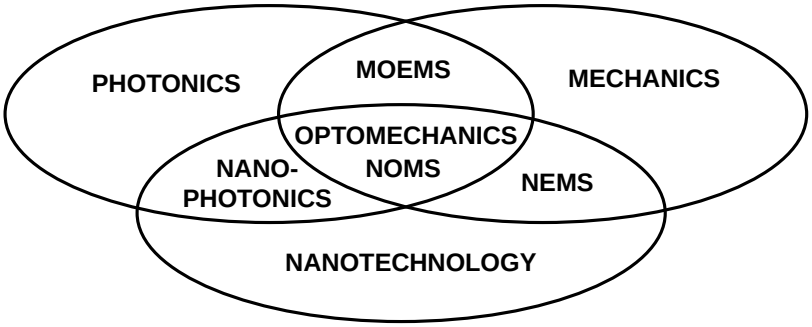

Figure 4: Venn-diagram showing schematically the three subdomains (photonics, mechanics and nanotechnology) that form the base of this multidisciplinary work. Optomechanics and Nano-opto-mechanical systems (NOMS), the subject of this Ph.D thesis, can be found at their cross-section.

molecules. By consequence optomechanics might provide a possibility for testing the fundamentals of quantum mechanics.

From engineering point of view we are rather interested to apply the optical force as an alternative actuation force for classical integrated MOEMS. Optomechanics could play a role when realizing an all-optical communication network. Optically reconfigurable filters and switches could be constructed with NOMS technology. Probably the most straightforward application can be found in the realm of RF-MEMS oscillators. These oscillators serve as reference clocks in integrated electronic circuits or any other application that requires an independent time keeping system. Other possible applications are extremely narrow band RF-filters and ultra sensitive force, mass or displacement sensors.

Experimental results

In order to detect optical forces exerted on a waveguide we place a second waveguide in parallel in the evanescent field of the first one. Consequently light couples back-and-forth between both waveguides and in fact we have created a directional coupler that enables detection of in-plane waveguide vibrations. Since a vibration changes the coupling between the waveguides a probe optical signal that is propagating through the vibrating waveguide is (power) modulated at the mechanical resonance frequency. After detec-

tion with a photodetector the probe signal can be analyzed in the electrical domain using an electrical spectrum analyzer or an oscilloscope.

With this method it is even possible to register the brownian vibration of the freestanding waveguides. The brownian force originates from the random, temperature induced vibrations of the atoms inside their lattice. The overall result of these vibrations at the atomic level is a chaotic vibration of the freestanding waveguides. However in spite of its chaotic nature the brownian vibration can be used to calibrate any other force exerted onto the waveguide because it is easy to calculate the magnitude of the brownian force analytically.

Having implemented a detection and calibration scheme we are ready to analyze the optical forces. A system with two parallel single-mode waveguides exhibits two guided modes (when only considering modes with the dominant electric field component parallel to the substrate): a symmetric (first order mode) and an anti-symmetric mode (second order mode). The forces that are generated by these modes can be calculated in different ways. In fact if we know the fields on a closed surface surrounding an object we can calculate the force exerted on the object. The calculations for the waveguide modes show that an attractive force is generated for the symmetric mode while typically a repulsive force can be associated with the anti-symmetric mode (for gaps that are sufficiently large).

In order to observe attractive and repulsive force we have to control the excitation of both modes. In this work we have designed a component that is able to excite the symmetric mode, anti-symmetric mode or a superposition of both modes, dependent on the wavelength used.

Since optical forces are relatively weak we also apply resonant excitation. The freestanding waveguides can be considered as beams or strings with a distinct resonance frequency. Using optical forces we excite these strings at their resonance frequency, so the pump laser needs to be modulated at the resonance frequency of the string. For this purpose an electro-optic modulator is inserted in the set-up. Since gas molecules tend to dampen the motion of the waveguide, we place the component in a vacuum chamber during measurement (see Fig. 5a).

Finally we were able to measure and calibrate optical forces between the waveguides. The final result is shown in Fig. 5b. We see that the force can be tuned from attractive to repulsive when sweeping the pump wavelength. We also note mode superpositions that generate a zero force in good agreement with the theory. This result was published in the scientific journal Nature Nanotechnology.

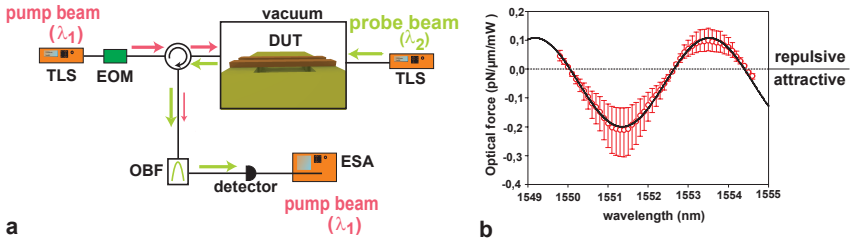

Figure 5: **Set-up and experimental result attractive vs. repulsive force. a**, Full set-up. The device-under-test (DUT) is placed in vacuum to remove air damping. Two tunable laser sources (TLS), one pump and one probe laser. The pump signal is modulated using an electro-optic modulator (EOM) to enable resonant excitation. The probe signal that registers the vibration is detected with a photodetector. Afterwards the electrical signal is analyzed using an electrical spectrum analyzer (ESA). **b**, Measured force when sweeping the pump wavelength. We notice that we obtain attractive and repulsive forces.

We have also investigated how the magnitude of the optical force can be increased. We have for example implemented an underetched waveguide in an optical resonator. Using a racetrack resonator we were able to verify that the optomechanical interaction is increased with the finesse of the resonator. Another interesting option we have explored are slot waveguides. This type of waveguides has a small slit (or slot) in its center in which light is concentrated intensively. Our experiments revealed a force in a slotted waveguide that was 25 times larger than the force experienced in the attractive-repulsive force experiment.

1 Introduction

We choose to go to the moon...we choose to go to the moon in this decade and do the other things, not because they are easy, but because they are hard, because that goal will serve to organize and measure the best of our energies and skills, because that challenge is one that we are willing to accept, one we are unwilling to postpone, and one which we intend to win, and the others too.
John F. Kennedy

1.1 Active and passive photonics

THE science of photonics includes the generation, emission, transmission, modulation, switching, amplification, detection and sensing of light. The portion of the electromagnetic radiation spectrum usually considered as light typically ranges from ultraviolet to infrared wavelengths (100 nm-3 μm). The invention of the laser in 1960 marks the early birth of this new field with lots of emerging applications of light, beyond simple lighting. Around 1980 the invention of glass fiber, a low-loss, relatively cheap transmission medium, has further instigated the widespread use of light as carrier of information, enabling large bandwidth telecommunications networks and the world wide web in particular.

Applications of photonics are however not limited to telecom. Included are all areas from everyday life to the most advanced science, e.g. displays,

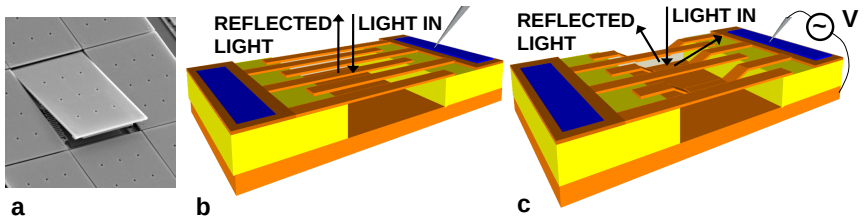

Figure 1.1: **Examples of Micro-opto-electro mechanical systems. a**, 2D-array of tiltable micromirrors with one mirror actuated, the picture is made available by Sandia National Laboratories [1]. **b**, Grating light valve (GLV) in unactuated state, light is specularly reflected in this state. **c**, When an actuation voltage is applied to the GLV a diffractive grating is created and light is diffracted into different diffraction orders.

information processing, medicine (surgery, vision correction, endoscopy, health monitoring), laser ablation (steel plate cutting), spectroscopy and a wide set of sensing applications (gas, biomolecules, distance, velocity). During the last decades the precise control and manipulation of light has turned into an everyday challenge to many scientists and photonics engineers around the globe.

Essentially light can be manipulated because of its interaction with matter and the fact that light interacts differently with materials that have different optical properties (such as refractive index and absorption coefficient). One famous example is the glass fiber we have already introduced. While in vacuum a beam of light tends to spread out and propagate in a straight line, the difference in refractive index between the core and the cladding material of the fiber causes the light to be 'guided' inside the fiber due to total internal reflection (TIR). If the bends in the fiber are not too sharp, the light will follow the bends and stay guided in the fiber core. Thanks to the fiber, light can be transported over many kilometers without spreading, attenuating or degrading too much, hence forming the backbone of telecom networks.

Such a fiber is an example of a passive structure. However for many applications photonic engineers are looking into devices with active functionality, which basically means that the passive functionality of the device can be altered in time in a controlled way. A clear example of active functionality can be found in display applications where active elements allow moving images.

Implementation of active functionality requires some external stimulus that changes the optical properties of the system. This external stimulus

can be among others an applied voltage that changes the refractive index of the material (electro-optic effect, liquid crystals) or a temperature change (thermo-optic effect). In addition when material is displaced the optical properties of the system might change drastically. Probably the most famous example is that of a moving mirror: when it is tilted an incident light beam will be deflected in a different direction. When such mirrors are scaled down to sub-mm size and put on a chip in an addressable matrix a very powerful concept arises: the Digital Micromirror Device (DMD) from Texas Instruments [2] indeed created a small revolution in the world of displays. Fig. 1.1a shows a picture of an actuated micromirror in a 2D-array. The DMD can also be used to route optical signals in a telecom network [3]. Another example of a light switching device based on moving parts is the grating light valve (GLV) [4]. The GLV basically consists of number of suspended parallel ribbons as shown in Fig. 1.1b. Incident light will mainly be specularly reflected. However when an actuation voltage is applied between a ribbon and the substrate the ribbon is pulled closer to the substrate. Leaving ribbons in turn unactuated and actuated creates an effective diffractive grating (Fig. 1.1c). In this state incident light is diffracted in different diffraction orders and hence an optical switch is created.

The commercial and scientific success of both the DMD [5] and the GLV [6, 7] illustrate the potential benefits that arise from combining photonics with mechanics. Devices of sub mm size that are mechanically actuated through an external stimulus are often referred to as Micro- Electro-Mechanical Systems (MEMS). MEMS that are used for manipulating light (such as the DMD and GLV) are commonly called Micro-Opto-Electro-Mechanical Systems (MOEMS) in the literature. In this work we go one step further and explore the cross-fertilization of photonics and mechanics with a third exciting research field that has emerged in the past decades: nanotechnology.

1.2 Photonics and mechanics at the nanoscale

1.2.1 Micro-electronics

In December 1959 physics nobel prize winner Richard Feynman gave a visionary talk at Caltech in which he stated that ”There is plenty of room at the bottom”, referring to the possibility of scaling devices to smaller sizes to increase functional density [8]. The clearest and probably most famous manifestation of this continuous shrinking process is known as Moore’s law [9], which states that the number of transistors that can be placed inexpensively on an integrated circuit doubles approximately every eighteen

months. For half a century now Moore's law has shown to be valid and currently billions of transistors can be placed on a single chip. In parallel the computing performance per unit cost has doubled every eighteen months, making relatively cheap and powerful processors financially accessible to millions of people. Moore's law has turned out to be rather an economic than a technological law and has influenced society dramatically.

1.2.2 Nanophotonics

Also in integrated photonics we observe a continuous tendency towards miniaturization, analogous to the remarkable evolution encountered in electronics. Again shrinking down the size holds the promise for increased and cheaper functionality on a single chip. In the context of fiber waveguides we have already explained that the core of a waveguide needs to have a higher refractive index than the cladding in order to achieve a guided light wave through TIR. For photonic structures miniaturization requires a higher refractive index contrast between the guiding waveguide core and its cladding. Luckily silicon —the favored semiconductor of the electronics industry— has a high refractive index in the near-infrared and visible range ($n_{Si} \approx 3.4 - 3.6$) and moreover in the telecom wavelength range ($\lambda = 1300 - 1620nm$) it has a very small absorption. In a silicon-on-insulator wafer (SOI) the top silicon layer is resting on a thin layer of silica (buried oxide layer BOx) with much lower refractive index ($n_{SiO_2} \approx 1.44$). Because of this high refractive index contrast ($\Delta n \approx 40\%$) a so-called 'photonic wire' defined in the top layer confines light strongly both in the vertical and horizontal direction. The BOx needs to be sufficiently thick in order to avoid leakage of light to the silicon substrate. A layer thickness of 2μm provides sufficient isolation. Typically a single mode waveguide has cross-section dimensions of only a few hundreds of nm and is able to take sharp bends with a bend radius of a few micrometers without excessive light loss [10]. Therefore very compact circuits are possible.

At the boundaries of the waveguide an exponentially decaying evanescent electric field can be found. In a high index contrast waveguide this evanescent field is decaying quickly with distance (to the core material) and the electric field is close to zero at distances of a few 100 nm. For this reason very strong field gradients can be found in the close neighborhood of high index contrast circuits. In chapter 4 en 5 we will see that this feature is most interesting in view of displacement sensing and generation of optical forces.

For a good control over their properties photonic wires need to be fabricated with a resolution of a few nm. For example the sidewalls need to be

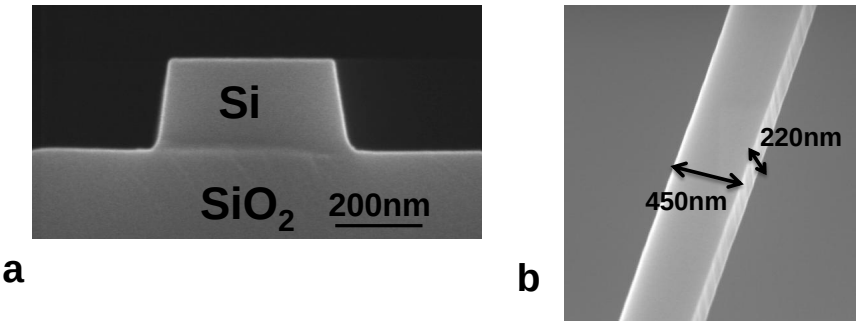

Figure 1.2: **Typical photonic wire.** **a**, Cross-section. **b** Top view with dimensions indicated. Roughness can be observed at the sidewalls. (picture courtesy: Shankar Kumar Selvaraja).

as smooth as possible in order to reduce scattering losses. Therefore, this field is often called nanophotonics. For silicon nanophotonics in particular, the know-how and expensive equipment of the CMOS-industries can be reused, hence in principle allowing cheap wafer scale mass fabrication of nanophotonic circuits, eventually integrated together with electronics on the same chip. In section 3.2 we will further elaborate on the process that is required for fabrication of nanoscale accuracy passive nanophotonic ciruits in SOI.

1.2.3 Nanomechanics

Finally also in the world of MEMS a continuous downscaling of devices has been established the last decades. Often MEMS are said to be evolving towards Nano-Electro-Mechanical Systems (NEMS) [11]. Besides increased functional density other reasons can be identified for downscaling NEMS. If we define a uniform scaling factor l_{sc} that all dimensions (width, height, length) are proportional to, one can prove that for a mechanical sensor the minimum detectable change in effective mass ∂M would scale proportional to l_{sc}^2 [12]. An intense reduction of the size would for example allow detection of single molecules attached to the mechanical sensor. Mass sensing resolutions down to the zeptogram ($10^{-21}\ g$) scale have been demonstrated with high-frequency low mass NEMS oscillators [13]. On the other hand the resonance frequency f_{res} of mechanical oscillators scales as l_{sc}^{-1} so in general smaller oscillators could be used for applications in the —for wireless communications interesting— GHz range. Such applications would include reference oscillators and RF-bandwidth filters. Coupled and syn-

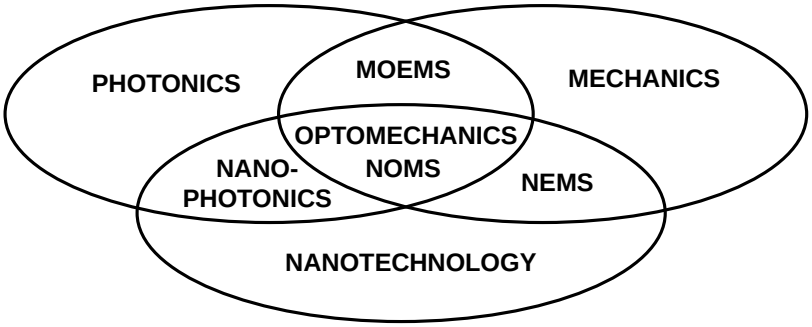

Figure 1.3: Venn-diagram showing schematically the three subdomains (photonics, mechanics and nanotechnology) that form the base of this multidisciplinary work. Optomechanics and Nano-opto-mechanical systems (NOMS), the subject of this Ph.D thesis, can be found at their cross-section

chronized mechanical oscillators have also been proposed as possible candidates to build circuits that mimic neural networks [14, 15]. These artificial neural networks could for example be used for pattern recognition, an extremely difficult task for classical computers. Again an intensive integration and miniaturization are key requirements to manage the large amount of interacting oscillators that would be needed for these circuits.

1.3 Objectives and applications

1.3.1 Device actuation through the optical gradient force

A simple downscaling of the concepts and devices encountered in MOEMS would lead us to Nano-Opto-Electro-Mechanical Systems (NOEMS). However in this work we go further and initiate a novel class of components. We want the external stimulus that actuates the mechanical structure to be *light*. This is an extremely challenging task since radiation pressure effects are in principle very small. Intuitively we think of light as imponderable and the momentum that is transferred to an object when a photon bumps into it seems negligible. Nevertheless we will see that at the nanoscale optical driving forces are not a utopia.

Light-matter interaction experiments have always been of extreme importance for the progress of fundamental physics. However when such experiments succeed in bridging the gap towards practical applications the impact is often tremendous. Optical forces for example are widely used to

manipulate microparticles such as living cells, DNA and bacteria in optical trapping and optical tweezer experiments [16]. The forces used in these experiments are *gradient* forces. One can prove that a polarizable particle will be accelerated towards higher fields regions when it experiences a field gradient, hence a force is exerted on the particle. We will discuss the optical gradient force in further detail in chapter 5. Only recently it was realized that the strong field gradient in the near field of guided wave structures could also be exploited for actuating optomechanical devices on a chip [17]. This way a novel class of components (which operate all-optical) was initiated. We will name these nanoscale light-manipulating mechanical structures that are actuated through optical forces Nano-Opto-Mechanical Systems (NOMS). In figure 1.3 we have shown schematically the multidisciplinary nature of NOMS.

1.3.2 NOMS applications

On the application side the first idea that pops up for all-optical components might be the exploitation as a building block in all-optical switch matrices or optically reconfigurable networks, although in that case unavoidably the question rises which switching speeds can be achieved using mechanical structures. It is indeed unsure to which extent optomechanical systems will be able to equal the speed of alternative systems based on other physical effects such as carrier injection [18] or depletion [19]. Nevertheless some salient advantages such as the potentially large tuning range and the fact that an optomechanical tuning process is purely dispersive and therefore potentially induces no optical losses are in favor of optomechanics. One can of course argue that the switching speed of mechanical devices is currently limited by efficient motion transduction. Faster switching speed comes at the cost of higher stiffness and stiffer devices show less displacement for a given force. So far motion transduction is limited by technology limitations rather than fundamental limits [12], so it is expected that advances in technology will also increase the operational speed of mechanical devices. Besides switching also wavelength conversion is another important function in all-optical networks which has been theoretically proposed using optomechanics [20], however still awaiting experimental verification.

MEMS oscillators also act as integrated high frequency reference oscillators, clocks or narrow RF-bandpass filters for wireless communication systems such as GSM [21–23]. Over the last years bulky off-chip reference quartz oscillators are indeed gradually replaced by integrated MEMS. Building electronics bandpass-filters with similar high-frequency high quality factor characteristics as achieved with MEMS is simply not possible.

Companies like Discera [24], SiTime [25] and SiLabs [26] have already brought this type of MEMS components to a commercial level and offer devices with typical operating frequencies up to a few hundreds of MHz.

For this type of products NOMS might provide the key for moving into the GHz region. NOMS could be used to create a reference signal or RF-filter directly in the optical domain because for very high frequency applications NEMS might still suffer from typical problems encountered with high frequency electronics: parasitic capacitances, unwanted transmission line effects, electromagnetic interference and radiation hardness (in particular for space applications). Better optical motion transduction and the possibility to use optical backaction effects (see further) to tune the band-pass filter width (to potentially very narrow line width) might be additional drivers here. The limited operational bandwidth for electrically actuated devices is also limiting the application of NEMS as sensing devices. Mass spectroscopy, charge sensing and weak force detection are strong candidates for potential sensing applications. Again access to smaller mass oscillators and hence higher resonator frequencies ($f_0 \sim l_{sc}^{-1}$) together with potentially better optical motion transduction would allow further improvements ($\partial M \sim l_{sc}^2$).

In the previous paragraph we have briefly introduced the attempts to use MEMS for the implementation of artificial neural networks. Remarkably very recently it has been proposed to use photonic circuits ('reservoirs') to achieve more or less the same goal [27]. Logically the question comes up whether we could benefit from the strong interplay between optics and mechanics encountered in optomechanical structures and merge the two approaches. Important advances will first have to be made in the fields of neural MEMS, photonic reservoirs and optomechanics to formulate an answer to this highly speculative question in the next years.

However the largest impact of optomechanics on the short and middle long term might be found at the more fundamental level. When a mechanical oscillator is part of an optical cavity such that the mechanical oscillation is influencing the cavity field and vice versa, dynamical back-action takes place [28]. In particular in the regime where the cavity life time approaches the mechanical oscillation period, interesting effects come into play. By tuning the pump wavelength to the blue side of the cavity amplification of the mechanical oscillations is possible through phonon-photon coupling [29, 30]. In fact the damping of the mechanical oscillation is reduced and the oscillation becomes more coherent, resulting in a smaller linewidth, hence an RF-filter with tunable bandwidth is created. A red detuned cavity shows the opposite behavior. The photons will now absorb phonons and thermal energy is removed from the oscillator. This process

is often referred to as optical cooling and shows great similarity with the optical cooling of atoms [31].

When sufficient thermal energy is removed from the oscillator it will fall back to its ground state and quantum mechanical behavior is observed [32]. Indeed recently a mechanical mode of a cantilever was cooled cryogenically to its quantum ground state such that its spatial position was a superposition of two different positions, so can one think of this cantilever as being at two positions at the same time [33]. This is a remarkable achievement because this cantilever is in fact a macroscopic object showing quantum mechanical behavior. We should however mention that some controversy exists on how to interprete the experiment exactly [34]. An in-depth analysis of the experiment is far beyond the scope of this thesis. Nevertheless the application of quantum mechanics to macroscopic objects will certainly lead to some thorough tests of quantum mechanics theory and undoubtedly to better insights. On the very long term the implementation of qubits on a chip (consisting of micromechanical oscillators) might no longer be a utopia and ultimately lead to powerful quantum computing or quantum cryptography schemes [35]. Also worth mentioning is the recent demonstration of optomechanically-induced transparency, the optomechanical equivalent of electromagnetically induced transparency [36].

1.3.3 Objectives of this work

In spite of the fascinating physics related to optical cooling we will mainly focus in this thesis on the gradient force as a novel actuation method for nanomechanical systems. However before delivering possible applications, we first need to learn how to walk before we can run. In other words we need to control and understand the very basic properties of optical gradient forces on a chip. So the main objective of this pioneering work is the demonstration and elementary characterization of optical gradient forces exerted on a nanophotonic structure by a guided light wave. We start our analysis with simple waveguides and look further into structures that potentially enhance the optical force (e.g. slotted waveguides, ring resonators) or structures that allow tuning of the force from attractive to repulsive. Elementary characterization also includes calibration (experimentally estimating the magnitude of the force) and comparison of the experimentally obtained values to numerical values obtained through theoretical models.

1.4 Thesis outline

In order to achieve our goal a number of subtasks need to be fulfilled which are reflected in the content of the different chapters. We choose to start with a thorough review of continuum mechanics in chapter 2. The reader with a rather limited background in mechanics is given the opportunity to catch up with the mechanical concepts needed to understand the following chapters. Chapter 3 is dedicated to the fabrication issues encountered with the fabrication of freestanding structures on the nanoscale. In chapter 4 we discuss motion transduction and introduce the brownian motion of mechanical structures. Both concepts are important in view of the above mentioned calibration of the optical gradient force. As we discussed earlier motion transduction might be a key element to practical high-frequency applications so we look at the integrated motion transduction techniques used and developed in this work in great detail. In chapter 5 we first discuss the theoretical aspects of optical gradient forces on a silicon-on-insulator chip and subsequently we show experimental results. These experiments can be considered to be the major achievements of this work. Finally in chapter 6 we implemented a system with optomechanical feedback to create strongly amplified regenerative oscillations.

1.5 Publications

The results that were obtained within this work were presented at several national and international conferences and published in various peer reviewed journals. Also 2 scientific awards were awarded for the research described in this thesis.

Publications in international journals

1. D. Van Thourhout, J. Roels, "Optomechanical device actuation through the optical gradient force", *Nature Photonics*, **invited**, vol. 4(4), pp. 211-217, (2010).

2. S. Rudra, J. Roels, G. Bryce, L. Haspeslagh , A. Witvrouw , D. Van Thourhout, "SiGe based Grating Light Valves: A leap towards monolithic integration of MOEMS", *Microelectronic Engineering*, 87, pp. 1195-1197, (2010).

3. N.A Yebo, D. Taillaert, J. Roels, D. Lahem, M. Debliquy, D. Van Thourhout, R. Baets, "Silicon-on-Insulator (SOI) Ring Resonator-

Based Integrated Optical Hydrogen Sensor", *IEEE Photonics Technology Letters*, vol. 21(14), pp. 960-962, (2009).

4. J. Roels, I. De Vlaminck, L. Lagae, B. Maes, D. Van Thourhout, R. Baets, "Tunable optical forces between nanophotonic waveguides", *Nature Nanotechnology*, 4, pp. 510-513, (2009).

5. J. Roels, W. Van Der Tempel, D. Van Nieuwenhove, R. Grootjans, M. Kuijk, D. Van Thourhout, R. Baets, "Continuous Time-of-Flight ranging using a MEMS diffractive subwavelength period grating demodulator", *Photonics Technology Letters*, 20(22), pp. 1827-1829, (2008).

6. I. De Vlaminck, J. Roels, D. Taillaert, D. Van Thourhout, R. Baets, L. Lagae, G. Borghs, "Detection of nanomechanical motion by evanescent light wave coupling", *Applied Physics Letters*, 90, (2007).

Publications in international conferences

1. J. Roels, B. Maes, R. Baets, D. Van Thourhout, "Integrated optomechanical circuits", *Integrated Photonics Research, Silicon and Nano Photonics (IPR)*, **invited**, Monterey, United States, (2010).

2. N.A Yebo, D. Taillaert, J. Roels, D. Lahem, M. Debliquy, Z. Hens, R. Baets, "Integrated optical gas sensors on silicon-on-insulator platform", *Integrated Photonics Research, Silicon and Nano Photonics (IPR)*, United States, pp. JTuB.17.pdf (3 pages), (2010).

3. J. Roels, B. Maes, R. Baets, D. Van Thourhout, "Silicon Optomechanics", *IEEE Photonics Society Summer Topicals*, **invited**, Playa Del Carmen, Mexico, pp. 90-91 (2010).

4. J. Roels, B. Maes, D. Van Thourhout, R. Baets, "Optical gradient dipole forces for nanophotonic devices on a silicon-on-insulator chip", *Proceedings of the 2009 Annual Symposium of the IEEE Photononics Benelux Chapter*, Belgium, pp. 21-24, (2009).

5. S. Rudra, J. Roels, G. Bryce, S. Severi, A. Witvrouw, R. Baets, D. Van Thourhout, "Grating light valves: a SiGe based approach towards monolithic integration of MOEMS", *Proceedings of the 2009 Annual Symposium of the IEEE Photononics Benelux Chapter*, Belgium, pp. 109-112, (2009).

6. N.A Yebo, D. Taillaert, J. Roels, M. Debliquy, D. Lahem, P. Lommens, Z. Hens, D. Van Thourhout, R. Baets, "Integrated optical gas sensors on silicon-on-insulator platform ", *Proceedings of the 2009 Annual Symposium of the IEEE Photonics Benelux Chapter*, Belgium, pp. 153-156, (2009).

7. J. Roels, B. Maes, D. Van Thourhout, R. Baets, "Optical gradient force in a slot waveguide on a Silicon-on-insulator-chip", *22nd Annual Meeting of the IEEE Photonics Society*, Turkey, pp. 223-224, (2009).

8. J. Roels, D. Van Thourhout, "Silicon optomechanics", *13th IEEE Photonics Society Benelux Annual Workshop*, **invited**, Netherlands, (2009).

9. J. Roels, I. De Vlaminck, L. Lagae, B. Maes, D. Van Thourhout, R. Baets, "Optomechanical interactions between nanophotonic wires on a silicon-on-insulator-chip", *Optical MEMS and Nanophotonics*, United States, pp. 33-34, (2009).

10. J. Roels, I. De Vlaminck, L. Lagae, B. Maes, D. Van Thourhout, R. Baets, "Attractive and repulsive optical gradient forces between silicon waveguides", *Quantum Optics of Nano-and Micromechanical Systems*, Germany, (2009).

11. J. Roels, W. Van der Tempel, D. Van Nieuwenhove, R. Grootjans, M. Kuijk, D. Van Thourhout, R. Baets, A dynamic subwavelength pitch grating modulator for continuous Time-Of-Flight ranging with optical mixing, *Optical MEMS and Nanophotonics*, Germany, p.176-177, (2008).

12. J. Roels, W. Van Der Tempel, D. Van Nieuwenhove, R. Grootjans, M. Kuijk, D. Van Thourhout, R. Baets, Measuring the time-of-flight with an optical MEMS-modulator, *ePIXnetSpring School 2008*, *Technology for Photonics Integration*, Italy, p.40, poster nr. 8, (2008).

13. W. van der Tempel, D. Van Nieuwenhove, R. Grootjans, Ljubomir Jovanov, J. Roels, Aleksandra Pizurica, D. Van Thourhout, R. Baets, Wilfried Philips, Maarten Kuijk, State-of-the-art modulator approaches for Continuous Time-of-Flight range finding,*IEEE/LEOS Symposium Benelux Chapter Proceedings*, Belgium, p.63-66, (2007).

14. I. De Vlaminck, J. Roels, D. Taillaert, D. Van Thourhout, L. Lagae, R. Baets, G. Borghs, Integrated nanomechanical motion detection

by evanescent light-wave coupling, *SPIE Photonics West (MOEM-S/MEMS)*, United States, (2007).

15. J. Roels, I. De Vlaminck, D. Van Thourhout, L. Lagae, D. Taillaert, R. Baets, A nanophotonic NEMS-modulator in Silicon-on-Insulator, *Annual Symposium of the IEEE/LEOS Benelux Chapter*, Netherlands, (2006).

16. J. Roels, D. Van Thourhout, R. Baets, Nanophotonic NEMS modulators in Silicon-on-insulator, *ePIXnet Winter School*, *Optoelectronic Integration - Technology and Applications*, Switzerland, p.75, (2006).

Publications in national conferences

1. J. Roels, I. De Vlaminck, D. Van Thourhout, L. Lagae, D. Taillaert, R. Baets, "A nanophotonic NEMS-modulator in silicon-on-insulator", 7e UGent-FirW Doctoraatssymposium, interactive poster session, Gent, Belgium, 2006.

2. J. Roels, B. Maes, R. Baets, D. Van Thourhout, "The force of light", 10e Ugent-Firw Doctoraatssymposium, Gent, Belgium, 2009.

Awards

1. IEEE Photonics Society graduate student fellowship 2010.

2. Barco High Tech Award for scientific research 2010.

Bibliography

[1] http://www.sandia.gov/media/NewsRel/NR1999/images/jpg.

[2] D.R. Collins, J.B. Sampsell, L.J. Hornbeck, J.M. Florence, P.A. Penz, and M.T. Gately. Deformable mirror device spatial light modulators and their applicability to optical neural networks. *Applied Optics*, 28(22):4900–4907, 1989.

[3] L.Y. Lin, E.L. Goldstein, and R.W. Tkach. Free-space micromachined optical switches with submillisecond switching time for large-scale optical crossconnects. *IEEE Photonics Technology Letters*, 10(4):525–527, 1998.

[4] O. Solgaard, F.S.A. Sandejas, and D.M. Bloom. Deformable grating optical modulator. *Optics Letters*, 17(9):688–690, 1992.

[5] J.B. Sampsell. Digital micromirror device and its application to projection displays. *Journal of Vacuum Science & Technology B*, 12(6):3242–3246, 1994. 38th International Symposium on Electron, Ion and Photon Beams, New Orleans, May 31-Jun 03, 1994.

[6] S. Rudra, J. Roels, G. Bryce, L. Haspeslagh, A. Witvrouw, and D. Van Thourhout. SiGe based grating light valves: A leap towards monolithic integration of MOEMS. *Microelectronic Engineering*, 87(5-9):1195–1197, 2008. The 35th International Conference on Micro- and Nano-Engineering, MNE.

[7] J. Roels, W. Van der Tempel, D. Van Nieuwenhove, R. Grootjans, M. Kuijk, D. Van Thourhout, and R. Baets. Continuous Time-of-Flight Ranging using a MEMS diffractive subwavelength period grating demodulator. *IEEE Photonics Technology Letters*, 20(21-24):1827–1829, 2008.

[8] R. Feynman. Plenty of room at the bottom, 1959, a transcript of Feynman's speech is available at http://www.its.caltech.edu/ feynman/-plenty.html.

[9] G.E. Moore. Cramming more components onto integrated circuits. *Electronics*, 38(8), 1965.

[10] W. Bogaerts, R. Baets, P. Dumon, V. Wiaux, S. Beckx, D. Taillaert, B. Luyssaert, J. Van Campenhout, P. Bienstman, and D. Van Thourhout. Nanophotonic waveguides in silicon-on-insulator fabricated with CMOS technology. *Journal of lightwave technology*, 23(1):401–412, 2005.

[11] K.L. Ekinci and M.L. Roukes. Nanoelectromechanical systems. *Review of Scientific Instruments*, 76(6), 2005.

[12] I. De Vlaminck. *Nanoscale resonators in optics and mechanics: development of electromechanical and optoelectronic transducers*. PhD thesis, Katholieke Universiteit Leuven, Leuven, Belgium, 2008.

[13] Y.T. Yang, C. Callegari, X.L. Feng, K.L. Ekinci, and M.L. Roukes. Zeptogram-scale nanomechanical mass sensing. *Nano Letters*, 6(4):583–586, 2006.

[14] S.B. Shim, M. Imboden, and P. Mohanty. Synchronized oscillation in coupled nanomechanical oscillators. *Science*, 316(5821):95–99, 2007.

[15] F.C. Hoppensteadt and E.M. Izhikevich. Synchronization of MEMS resonators and mechanical neurocomputing. *IEEE Transactions on circuits and systems I-Fundamental theory and applications*, 48(2):133–138, 2001.

[16] S. Chu. Laser manipulation of atoms and particles. *Science*, 253(5022):861–866, 1991.

[17] M.L. Povinelli, M. Loncar, M. Ibanescu, E.J. Smythe, S.G. Johnson, F. Capasso, and J.D. Joannopoulos. Evanescent-wave bonding between optical waveguides. *Optics letters*, 30(22):3042–3044, 2005.

[18] Q. Xu, S. Manipatruni, B. Schmidt, J. Shakya, and M. Lipson. 12.5 Gbit/s carrier-injection-based silicon micro-ring silicon modulators. *Optics express*, 15(2):430–436, 2007.

[19] D. Marris-Morini, X. Le Roux, L. Vivien, E. Cassan, D. Pascal, M. Halbwax, S. Maine, S. Laval, J.M. Fedeli, and J.F. Damlencourt. Optical modulation by carrier depletion in a silicon PIN diode. *Optics Express*, 14(22):10838–10843, 2006.

[20] M. Notomi, H. Taniyama, S. Mitsugi, and E. Kuramochi. Optomechanical wavelength and energy conversion in high-Q double-layer cavities of photonic crystal slabs. *Physical review letters*, 97(2), 2006.

[21] C. Nguyen. Vibrating RF MEMS for next generation wireless applications. pages 257–264, 2004. IEEE Custom Integrated Circuits Conference, Orlando, FL, 2004.

[22] Wan-Thai Hsu. Vibrating RF MEMS for timing and frequency references. pages 672–675, 2006. IEEE MTT-S International Microwave Symposium, San Francisco, CA, 2006.

[23] H.J. De Los Santos, G. Fischer, H.A.C. Tilmans, and J.T.M. van Beek. RF MEMS for ubiquitous wireless connectivity: Part 2 - Application. *IEEE Microwave Magazine*, 5(4):50–65, 2004.

[24] http://www.discera.com.

[25] http://www.sitime.com.

[26] http://www.silabs.com.

[27] K. Vandoorne, W. Dierckx, B. Schrauwen, D. Verstraeten, R. Baets, P. Bienstman, and J. Van Campenhout. Toward optical signal processing using Photonic Reservoir Computing. *Optics Express*, 16(15):11182–11192, 2008.

[28] V.B. Braginsky. Classical and quantum restrictions on detection of weak distrubances of a macroscropic oscillator. *Soviet Physics JETP-USSR*, 26(4):831–836, 1968.

[29] T. J. Kippenberg and K. J. Vahala. Cavity optomechanics: Back-action at the mesoscale. *Science*, 321(5893):1172–1176, 2008.

[30] Tobias J. Kippenberg and Kerry J. Vahala. Cavity opto-mechanics. *Optics Express*, 15(25):17172–17205, 2007.

[31] H.J. Metcalf and P. Van der Straten. Laser cooling and trapping of atoms. *Journal of the Optical Society of America B-Optical Physics*, 20(5):887–908, 2003.

[32] K.C. Schwab and M.L. Roukes. Putting mechanics into quantum mechanics. *Physics Today*, 58(7):36–42, 2005.

[33] A. D. O'Connell, M. Hofheinz, M. Ansmann, Radoslaw C. Bialczak, M. Lenander, E. Lucero, M. Neeley, D. Sank, H. Wang, M. Weides, J. Wenner, John M. Martinis, and A. N. Cleland. Quantum ground state and single-phonon control of a mechanical resonator. *Nature*, 464(7289):697–703, 2010.

[34] Adrian Cho. Faintest Thrum Heralds Quantum Machines. *Science*, 327(5965):516–518, JAN 29 2010.

[35] Peter W. Shor. Polynomial-time algorithms for prime factorization and discrete logarithms on a quantum computer. *SIAM Review*, 41(2):303–332, 1999.

[36] S. Weis, R. Riviere, S. Deleglise, E. Gavartin, O. Arcizet, A. Schliesser, and T. J. Kippenberg. Optomechanically Induced Transparency. *Science*, 330(6010):1520–1523, DEC 10 2010.

2
Continuum Mechanics

Two roads diverged in a wood, and I -
I took the one less traveled by,
And that has made all the difference.
Robert Frost

2.1 Introduction to the chapter

FROM the introductory chapter it is clear that we can benefit from combining photonics and mechanics. In this chapter we focus on mechanics and introduce the basics of beam theory. In fact most of the content of this chapter can be found in the literature, however we included it in this thesis because these essential concepts are necessary for the reader to understand the following chapters. We first derive the Euler beam equation and discuss static solutions and the influence of residual stresses in the beam. We also look into the beam's dynamic behavior and introduce a lumped parameter model which facilitates the mathematical analysis. Finally we give an overview of the several damping mechanisms in mechanical resonators and finish the chapter with a short explanation on non-linear mechanics.

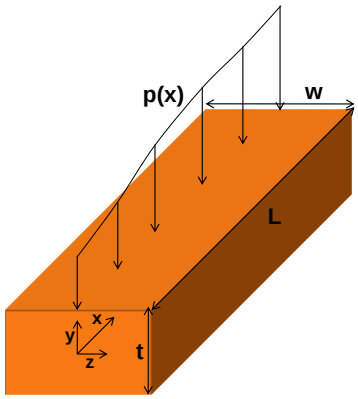

Figure 2.1: A simple beam with length L, width w, thickness t and an external load distribution p(x)

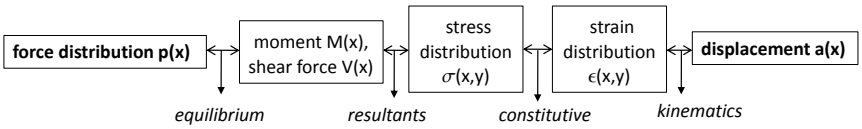

Figure 2.2: Scheme for the derivation of the beam equation

2.2 Static beam equation

We will consider the beam depicted in Fig. 2.1 with a rectangular cross-section (thickness t, width w) that is invariant in the x-direction (length L) and consisting of only one uniform material, assumptions that are highly relevant for the waveguide structures we will discuss in our work. When subjected to an external force internal forces will be generated inside the beam which counteract the external force so the beam responds with a certain internal 'stiffness'. Essentially we want to connect a force distribution $p(x)$ with a (vertical) displacement $a(x)$. For achieving this goal we will use four distinct subsets of beam theory [1]: equilibrium equations, resultants, constitutive laws and kinematics. In Fig. 2.2 it is shown schematically how $p(x)$ and $a(x)$ are connected through these four distinct subsets of beam theory.

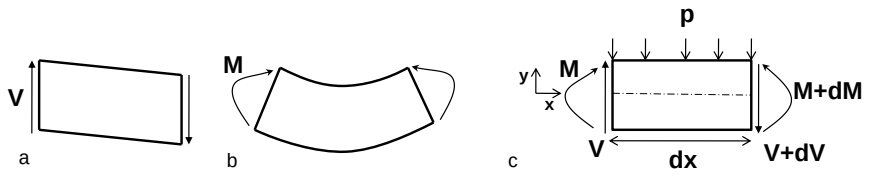

Figure 2.3: **Shear forces and bending moments acting on a differential beam element. a**, Shear force V. **b**, Bending moment M. **c**, Fully loaded differential element with length $\mathrm{d}x$.

2.2.1 Equilibrium equations

The equilibrium equations describe how the beam connects an external load with internal shear forces and bending moments. As shown in Fig. 2.3a and b a shear force pair (unit N, symbol V) tends to rotate the beam element while bending moments (unit Nm, symbol M) try to bend it. Shear forces are forces which act along the face of a surface. Direct forces act perpendicular to a surface. A fully loaded differential element with length $\mathrm{d}x$ is shown in Fig. 2.3c. To obtain force equilibrium the forces acting on the element must cancel out each other so $p\,\mathrm{d}x + (V + \mathrm{d}V) = V$ leading to:

$$-p = \frac{\mathrm{d}V}{\mathrm{d}x} \tag{2.1}$$

We also require moment equilibrium (for example on the left side of the beam element) so $M = M + \mathrm{d}M - (V + \mathrm{d}V)\mathrm{d}x - p\frac{\mathrm{d}x^2}{2}$. Ignoring the terms with a product of two differentials we obtain:

$$V = \frac{\mathrm{d}M}{\mathrm{d}x} \tag{2.2}$$

2.2.2 Resultants

Stress is defined microscopically as the force per unit area acting on the surface of a differential volume element as shown in Fig. 2.4a. At this microscopic level we assume that the stress acts uniformly across the entire surface of the element. We denote normal and shear stresses. Normal stresses act perpendicular to the surfaces of the volume element. They are (symbol σ, the subscript identifies the axis along which the stress acts) and shear stresses (acting along the surfaces, symbol τ with the first subscript identifying the face and the second one identifying the direction). Consider the cross-section of a beam at a certain point x where we find a distribution

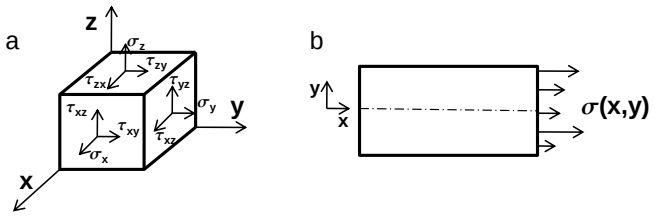

Figure 2.4: **Definition of stress and stress distribution.** **a**, Differential volume element with definition of normal and shear stresses. **b**, Stress distribution $\sigma(x, y)$ over the beam cross-section.

of normal stresses $\sigma(x, y)$ (Fig. 2.4b). An asymmetric distribution (with respect to the x-axis) of normal stresses might create a net non-zero moment resultant $M(x)$ about the $y = 0$ plane:

$$M(x) = \iint y\, \sigma_x(x, y)\, \mathrm{d}y\, \mathrm{d}z \tag{2.3}$$

The shear resultant $V(x)$ is defined as:

$$V(x) = \iint \tau_{xy}(x, y)\, \mathrm{d}y\, \mathrm{d}z \tag{2.4}$$

The convenience of the resultants lies in them being dependent only of x instead of both x and y. In addition formula 2.2 provides us with a relation between the two resultants $M(x)$ and $V(x)$ so within the assumptions made to derive the equilibrium equations we will only need one of the resultants.

2.2.3 Constitutive material laws

A material under stress can deform and the unitless relative deformation is called strain [2]. Typically an element with length L undergoes a deformation ΔL and the (uniaxial) strain reads as: $\epsilon = \frac{\Delta L}{L}$. Analogous to stresses both normal and shear strains can be defined. For the construction of our beam model we will assume a Hooke law like equation with E Young's modulus (GPa):

$$\sigma(x, y) = E\, \epsilon(x, y) \tag{2.5}$$

For an anisotropic crystal however the stress-strain relation is in general much more complicated and should be described by a 6 by 6 tensor. This is the case for monocrystalline silicon, the relevant material for our work. We

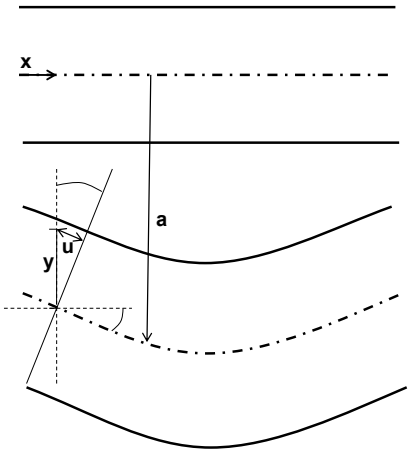

Figure 2.5: Straight and bent beam. The beam displacement a(x) can finally be tied to the longitudinal strain $\epsilon(x,y) = -\frac{\mathrm{d}u}{\mathrm{d}x}$

will address this issue at the appropriate moment and deal with equation 2.5 for now.

2.2.4 Kinematics

Consider the beam in Fig. 2.5, which is bent according to a profile a(x). The dash-dotted line denotes the neutral axis. Along this axis there are no longitudinal (x-direction) stresses even if the beam is bent. Due to the bending a point in the beam cross-section that was originally at the coordinates (x,y) is translated. In the limit of small bending we can safely ignore the strain in the y-direction and beam's stiffness is governed by strain in the x-direction. Indeed the point which was originally at coordinates (x,y) is translated in the x-direction over a distance $u(x,y)$ resulting in a longitudinal strain $\epsilon(x,y) = -\frac{\mathrm{d}u}{\mathrm{d}x}$. Using simple geometric laws we find the bending induced displacement in the x-direction to be $u(x,y) = y\,\chi(x)$ Finally noting that $\chi \approx \theta$ (see Fig. 2.5 for the definition of the angles χ and θ) and $\theta = \frac{\mathrm{d}a}{\mathrm{d}x}$ we can tie the beam displacement $a(x)$ to the strain $\epsilon(x,y)$:

$$\epsilon(x,y) = -\frac{\mathrm{d}^2 a}{\mathrm{d}x^2}\, y \tag{2.6}$$

2.2.5 The Euler beam equation

Starting from equation 2.6 we eliminate strain in favor of stress using formula 2.5. Multiplying both sides of the equation with y and integrating over the beam cross-section yields: $\iint y\,\sigma(x,y)\,dy\,dz = -E\iint y^2\frac{\mathrm{d}^2a}{\mathrm{d}x^2}\,dy\,dz$. The left hand side of this equation equals equation 2.3, i.e. the resultant $M(x)$. In the right part we recognize the definition of the beam's area moment of inertia, defined as

$$I = \iint y^2\,dy\,dz = \int_{\frac{-w}{2}}^{\frac{w}{2}}\int_{\frac{-t}{2}}^{\frac{t}{2}} y^2\,dy\,dz = \frac{wt^3}{12} \tag{2.7}$$

so we obtain:

$$M = -E\,I\,\frac{\mathrm{d}^2a}{\mathrm{d}x^2} \tag{2.8}$$

Taking the second derivative for x at both sides and eliminating M in favor of p using the equilibrium equations 2.2 and 2.1 we finally find:

$$p(x) = \frac{\mathrm{d}(I\,E\,\frac{\mathrm{d}^2a}{\mathrm{d}x^2})}{\mathrm{d}x^2} = E\,I\,\frac{\mathrm{d}^4a}{\mathrm{d}x^4} \tag{2.9}$$

The last term in this equation is a valid simplification if both E and I are invariant along x, which is a feasible assumption for the structures discussed in this work.

2.2.6 Solving the static Euler beam equation

Looking at equation 2.9 and assuming a uniform load distribution p independent of x we can see that $a(x)$ must be given by a fourth-order polynomial:

$$a(x) = \frac{px^4}{24EI} + C_1\,x^3 + C_2\,x^2 + C_3\,x + C_4 \tag{2.10}$$

The constants C_1,C_2,C_3 and C_4 are determined by considering the boundary conditions of the problem. Typically two conditions are applied at each of the two ends of the beam (at x=0 and x=L) so we can solve for these four constants. Three types of end conditions have a practical significant physical meaning: fixed, hinged and free ends, enabling six possible beam types [3]. Beams with one free end are commonly called cantilevers. Fixed boundary conditions allow no displacement or rotation:

$$a = 0;\quad \frac{\mathrm{d}a}{\mathrm{d}x} = 0 \tag{2.11}$$

Hinged boundary conditions allow rotation but no displacement and also the bending moment and by consequence $\frac{\mathrm{d}^2 a}{\mathrm{d}x^2}$ (see equation 2.8) must be zero:

$$a = 0; \quad \frac{\mathrm{d}^2 a}{\mathrm{d}x^2} = 0 \tag{2.12}$$

At a free end of the beam no bending moment or shear force is present so (see again equation 2.8 and 2.2):

$$\frac{\mathrm{d}^3 a}{\mathrm{d}x^3} = 0; \quad \frac{\mathrm{d}^2 a}{\mathrm{d}x^2} = 0 \tag{2.13}$$

In the context of this work we are mainly interested in two particular cases: fixed ends at both sides of the beam (fixed-fixed) and hinged ends at both ends (hinged-hinged). Solving for the unknown constants in formula 2.10 for a fixed-fixed beam we find:

$$a_{ff}(x) = \frac{x^2 p(L-x)^2}{24EI} \tag{2.14}$$

For a hinged-hinged beam:

$$a_{hh}(x) = \frac{px(-x+L)(-x^2+Lx+L^2)}{24EI} \tag{2.15}$$

Noting that pL is the total force F on the beam and considering the (maximum) deflection in the middle of the beam ($x = \frac{L}{2}$) both equations 2.14 and 2.15 can be interpreted as a Hooke-like law $a(\frac{L}{2}) = \frac{F}{k}$ with the following spring constants:

$$k_{ff}(x) = \frac{384EI}{L^3} \tag{2.16}$$

$$k_{hh}(x) = \frac{384EI}{5L^3} \tag{2.17}$$

The spring constant is 5 times lower for hinged ends compared to fixed ends because rotation is permitted at the clamping points in the former case. This is also illustrated in Fig. 2.6 where the normalized (such that the maximum deflection is 1) bending profile for a fixed-fixed beam with unit length is shown. The profile for a hinged-hinged beam with the same parameters is also shown. If we replace the distributed force by a point load F in the middle of the beam the spring constant reduces with a factor of 2 for the fixed-fixed beam and a factor 1.6 for the hinged-hinged beam, indicating that the beam is more susceptible to forces applied in its center. Given the cubic dependence on L in the denominator of equations 2.16 and 2.17 and the sharp contrast between the curves in Fig. 2.6 it is already clear that the mechanical properties of the beams might depend strongly on subtle differences in the fabrication process.

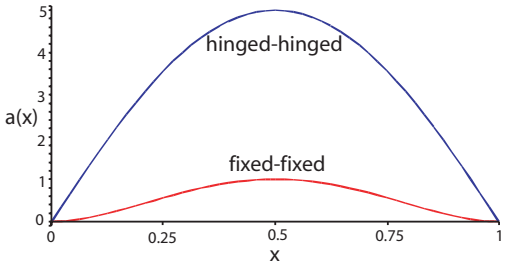

Figure 2.6: **Static bending profiles for beams with unit length. a**, Fixed-fixed (red curve). **b**, Hinged-hinged (blue curve).

2.3 Influence of residual axial stress

2.3.1 Euler beam equation with stress

Residual stress might be introduced in a freestanding structure during the fabrication process. Alternatively a stress free fixed-fixed beam will encounter compressive (tensile) stress when the temperature is increased (decreased) and differential thermal material expansion takes place. The induced stress can be written as $\sigma = -\alpha\,\Delta T\,E$ with α (K^{-1}) the material's thermal expansion coefficient and ΔT a temperature shift. When no force is exerted on the (flat) beam the stress is of no influence at all, however when the beams bends an additional load is created proportional to the local curvature [2]. This can be understood by noting that for small bending the axial force $\sigma\,S = N$ (S the beam cross-section and N is called tension) creates a vertical force component on an elementary piece of beam $\mathrm{d}x$ equal to $\sigma S \frac{\mathrm{d}a}{\mathrm{d}x} = p_{stress}\mathrm{d}x$ (Fig. 2.7). Hence an effective load $p_{stress} = \sigma\,S\,\frac{\mathrm{d}^2a}{\mathrm{d}x^2} = N\frac{\mathrm{d}^2a}{\mathrm{d}x^2}$ is obtained which simply adds to the load p in equation 2.9.

$$p + \sigma\,S\,\frac{\mathrm{d}^2a}{\mathrm{d}x^2} = E\,I\,\frac{\mathrm{d}^4a}{\mathrm{d}x^4} \tag{2.18}$$

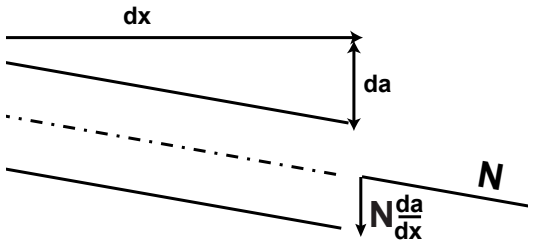

Figure 2.7: **Stress on an elementary piece of beam, creating a vertical load.**

We can solve for $a(x)$ using the laplace transform technique and applying fixed boundary conditions in $\pm\frac{L}{2}$:

$$\begin{aligned} a(x) =& \frac{p}{8N\left(2\alpha\sqrt{EIN} - NL\beta\right)\alpha}(6\sqrt{EIN}L^2\beta^2 - 2\sqrt{EIN}L^2 \\ & - \alpha NL^3\beta - 8L\alpha\beta EI - 8x^2\sqrt{EIN}\beta^2 + 8x^2\sqrt{EIN} + 4x^2\alpha NL\beta \\ & + 8LIE\cosh\left(x\sqrt{\frac{N}{EI}}\right)\alpha - 4L^2\cosh\left(x\sqrt{\frac{N}{EI}}\right)\sqrt{EIN}\beta) \end{aligned} \tag{2.19}$$

In this formula we have introduced the constants $\alpha = \sinh(\frac{L}{2}\sqrt{\frac{N}{EI}})$ and $\beta = \cosh(\frac{L}{2}\sqrt{\frac{N}{EI}})$. In spite of the roots $\sqrt{EIN}$ the formula yields real values for both positive (tensile stress) and negative N (compressive stress) because the imaginary values of the roots $\sqrt{EIN}$ for negative N are canceled out by the imaginary values for $\sinh(\frac{L}{2}\sqrt{\frac{N}{EI}})$. Similar to the analysis in the previous section we can obtain an effective spring constant by con-

sidering the point of maximum deflection $a_{MAX} = a(x = 0)$ yielding:

$$k_{tot,stress} = \frac{8N(-2\alpha\sqrt{EIN} + NL\beta)\alpha}{\sqrt{EIN}(-6L\beta^2 + 2L + \frac{\alpha NL^2\beta}{\sqrt{EIN}} + \frac{\alpha\beta EI}{\sqrt{EIN}} - \frac{8EI\alpha}{\sqrt{EIN}} + 4L\beta)} \tag{2.20}$$

The validity of these formulas can be checked by taking the limits $\lim_{N\to 0} k_{tot,stress}$ and $\lim_{N\to 0} a(x)$ which indeed yield equivalent expressions to 2.16 and 2.14. A cumbersome formula like 2.20 does not provide us with much physical insight though. In the following subsection we will illustrate that much more transparent approximate expressions can be obtained through the principle of virtual work and a variational approach using trial functions [4].

2.3.2 Variational method

Assume we have a trial function $\hat{a}(x, c_1, c_2...c_n) =$ describing the beam displacement where c_1 to c_n are a set of n parameters that appear in the trial function. We also introduce $\mathcal{U}$ denoting the potential energy of the system:

$$\mathcal{U} = \text{stored energy} - \text{work done} \tag{2.21}$$

The principle of virtual work states that $\mathcal{U}$ must be stationary with respect to any virtual displacement so $\frac{\partial \mathcal{U}}{\partial c_j} = 0, j = 1..n$ leading to n equations. Solving these n equations yields the n values c_j that minimize the potential energy $\mathcal{U}$. Hence they represent the best approximation $\hat{a}(x, c_1, c_2...c_n)$ to the equilibrium displacement $a(x)$ we can make within the set of trial functions we started with.

We propose a cosine shape as a trial function: $\frac{c}{2}[1 + \cos(\frac{2\pi x}{L})]$. This shape is symmetric around x=0 and fixed boundary conditions are fulfilled in both $x = \pm\frac{L}{2}$. The maximum deflection c is the only available parameter for our variational problem. With this trial function the work done simply reads as (for a uniform load p):

$$\text{work done} = pL \int_{\frac{-L}{2}}^{\frac{L}{2}} \frac{c}{2}[1 + \cos(\frac{2\pi x}{L})]\mathrm{d}\frac{x}{L} = \frac{pLc}{2} \tag{2.22}$$

Determining the stored elastic energy in the beam is a slightly more complicated problem. First we note that the stress-strain product (dimension $Nm^{-2} = Jm^{-3}$) can be interpreted as an energy density function:

$$\mathcal{W}(x, y, z) = \int_0^{\epsilon(x,y,z)} (\sigma(\epsilon) + \sigma_0)\mathrm{d}\epsilon = \frac{E\epsilon^2}{2} + \sigma_0\epsilon \tag{2.23}$$

In this equation σ_0 denotes a residual axial stress.

In subsection 2.2.4 we have already found the axial strain due to beam bending:

$$\epsilon_{bend} = -\frac{\mathrm{d}^2\hat{a}}{\mathrm{d}x^2}\, y \tag{2.24}$$

However when the displacement is sufficiently large the beam lengthens which induces extra strain. From elementary function theory we know that the curve length s of a function $\hat{a}(x)$ over an interval $[-\frac{L}{2}, \frac{L}{2}]$ can be calculated through $s = \int_{-\frac{L}{2}}^{\frac{L}{2}} \sqrt{1 + (\frac{\mathrm{d}\hat{a}}{\mathrm{d}x})^2}\mathrm{d}x \approx \int_{-\frac{L}{2}}^{\frac{L}{2}} 1 + \frac{1}{2}(\frac{\mathrm{d}\hat{a}}{\mathrm{d}x})^2\mathrm{d}x = L + \frac{1}{2}\int_{-\frac{L}{2}}^{\frac{L}{2}}(\frac{\mathrm{d}\hat{a}}{\mathrm{d}x})^2\mathrm{d}x$ The approximation being valid for $1 \gg (\frac{\mathrm{d}\hat{a}}{\mathrm{d}x})^2$ we substitute our trial function and using the definition of strain $(\frac{s-L}{L})$ we obtain:

$$\epsilon_{stretch} = (\frac{\pi c}{2L})^2 \tag{2.25}$$

Taking the volume integral of $\mathcal{W}(x, y, z)$ over the beam dimensions returns the total stored elastic energy in the beam. Using equation 2.23 for the energy density and taking $\epsilon = \epsilon_{bend} + \epsilon_{stretch}$ we find:

$$\begin{aligned}
&\text{stored energy} = \int_{\frac{-w}{2}}^{\frac{w}{2}}\int_{\frac{-t}{2}}^{\frac{t}{2}}\int_{\frac{-L}{2}}^{\frac{L}{2}} \mathcal{W}(x,y,z)\,\mathrm{d}x\mathrm{d}y\mathrm{d}z \\
&\int_{\frac{-w}{2}}^{\frac{w}{2}}\int_{\frac{-t}{2}}^{\frac{t}{2}}\int_{\frac{-L}{2}}^{\frac{L}{2}} \frac{E(\epsilon_{bend}+\epsilon_{stretch})^2}{2} + \sigma_0(\epsilon_{bend}+\epsilon_{stretch})\mathrm{d}x\mathrm{d}y\mathrm{d}z \\
&= \int_{\frac{-w}{2}}^{\frac{w}{2}}\int_{\frac{-t}{2}}^{\frac{t}{2}}\int_{\frac{-L}{2}}^{\frac{L}{2}} \frac{E\epsilon_{bend}^2}{2} + \sigma_0\epsilon_{stretch} + \frac{E\epsilon_{stretch}^2}{2}\mathrm{d}x\mathrm{d}y\mathrm{d}z \\
&= \frac{\pi^4 EI}{L^3}c^2 + \frac{\pi^2\sigma_0 wtc^2}{4L} + \frac{\pi^4 Ewtc^4}{32L^3}
\end{aligned} \tag{2.26}$$

As can be seen only three contributions in this integral are non-zero. We can easily construct the potential energy now using equations 2.21, 2.22 and 2.26:

$$\mathcal{U}(c) = \frac{\pi^4 EI}{L^3}c^2 + \frac{\pi^2\sigma_0 wtc^2}{4L} + \frac{\pi^4 Ewtc^4}{32L^3} - \frac{pLc}{2} \tag{2.27}$$

Solving $\frac{\partial\mathcal{U}}{\partial c} = 0$ for $\frac{pL}{c} = \frac{F}{c}$ returns an effective spring constant:

$$k_{eff} = k_{geom} + k_{stress} + k_{nl}c^2 = \frac{4\pi^4 EI}{L^3} + \frac{\pi^2\sigma_0 wt}{L} + \frac{\pi^4 twE}{4L^3}c^2 \tag{2.28}$$

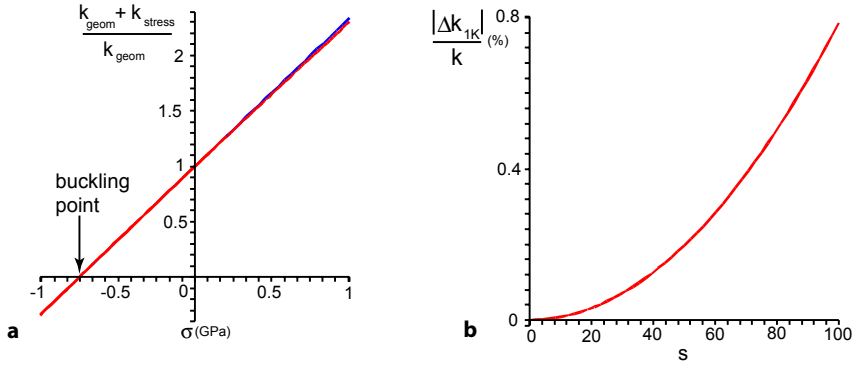

Figure 2.8: **Influence of residual axial stress. a**, The total spring constant ($k_{geom} + k_{stress}$) vs. stress (σ) is plotted for a fixed-fixed beam, normalized to k_{geom}. At the critical stress the stiffness becomes zero (buckling point). The red curve is the exact solution (equation 2.20) , the blue curve is the approximative solution of equation 2.28 showing almost perfect match (parameters: beam length $L = 12\mu m$, Young's modulus $E = 169\,GPa$, thickness $t = 220\,nm$ $w = 440\,nm$). **b**, Plot of the relative shift of the spring constant for $1K$ temperature shift in function of the slenderness ratio $s = \frac{L}{t}$, showing a non-negligible shift.

This effective spring constant falls apart in three parts. The first contribution can be interpreted as the geometrical stiffness k_{geom} originating from the bending strain that is induced in the beam when it is deflected. The numerical prefactor $4\pi^4 \approx 389.6$ deviates approximately 1.5% to the prefactor 384 we found for the effective spring constant in equation 2.16, suggesting that our trial solution $\hat{a}(x)$ represents a good approximation to the solution $a(x)$ (equation 2.14). The second contribution represents an additional stiffness k_{stress} due to residual stress in the beam. The magnitude of k_{stress} equals the geometric stiffness for a critical stress value given by:

$$|\sigma_{crit}| = \frac{\pi^2}{3}(\frac{t}{L})^2 E \tag{2.29}$$

In case of compressive stress the geometrical stiffness is canceled out for this critical stress value and buckling occurs. In Fig. 2.8a the total normalized linear stiffness ($k_{geom} + k_{stress}$, normalized to k_{geom}) is shown as function of stress. The red curve is derived from the exact solution to the Euler beam differential equation with stress (equation 2.18). The blue curve is the approximative solution obtained through the variational method (2.28). The excellent match again shows the power of this method.

From equation 2.29 we also conclude that the critical stress scales inverse quadratically with $(\frac{L}{t}) = s$ thus slender beams are more sensitive to stress induced stiffness. s is called the slenderness ratio. To illustrate the influence of temperature variations on slender beams we have also plotted the relative shift of the stiffness vs. the slenderness ratio s (Fig. 2.8b). In this plot we have set the stress parameter to the compressive stress that arises in a fixed-fixed silicon beam when the temperature is raised over $1K$, assuming a linear thermal expansion coefficient of $2.59\,10^{-6}K^{-1}$ at $25°C$ [5]. We conclude that in sufficiently slender beams temperature variations as small as $1K$ are able to decrease the stiffness with a fraction of a percent.

Finally we also mention that the stretching induced strain also induces a non-linear stiffness that scales with c^2 (see the last term in equation 2.28). We will discuss this non-linearity in further detail in section 2.7.

2.4 Dynamic beam equation

The equation 2.9 can be used directly to obtain the dynamic equation for free (unloaded) vibration of the beam. In accordance with the principle of D'Alembert we just need to imagine the vibrating bar to be loaded by an inertia force $p = -\rho S \frac{\mathrm{d}^2 a}{\mathrm{d}t^2}$ rather than an external load [3]. With ρ the mass density, S the cross-section of the beam and t the time coordinate we obtain the dynamic beam equation for $a(x,t)$:

$$E\,I\,\frac{\partial^4 a}{\partial x^4} + \rho S \frac{\partial^2 a}{\partial t^2} = 0 \tag{2.30}$$

Using the technique of separation of variables we assume $a(x,t)$ can be expressed as $X(x)f(t)$ with $X(x)$ being independent of t and $f(t)$ being independent of x. Then equation 2.30 can be rearranged:

$$\frac{E\,I}{\rho A X(x)}\frac{\mathrm{d}^4 X(x)}{\mathrm{d}x^4} = -\frac{1}{f(t)}\frac{\mathrm{d}^2 f(t)}{\mathrm{d}t^2} = \omega_n^2 \tag{2.31}$$

We see that the left side of the equation is function of x only while the right side is dependent of t only. Hence both sides must equal a constant which we will call ω_n^2 and which leads us to the solution for $f(t) = A_n\,\sin(\omega_n t) + B_n\,\cos(\omega_n t)$. The amplitude of vibration in a point x will vary harmonically in time (A_n and B_n are two constants determined by the initial conditions). The general solution for $X(x)$ is given by:

$$\begin{aligned} X(x) =& C_1\,[\cos(k_n x) + \cosh(k_n x)] + C_2\,[\cos(k_n x) - \cosh(k_n x)] + \\ & C_3\,[\sin(k_n x) + \sinh(k_n x)] + C_4\,[\sin(k_n x) - \sinh(k_n x)] \end{aligned} \tag{2.32}$$

In this equation we have introduced the constant k_n:

$$k_n^4 = \frac{\omega_n^2 \rho S}{EI} \tag{2.33}$$

Applying fixed clamping conditions in $x = 0$ leads to $C_1 = C_3 = 0$. Fixed clamping conditions in $x = L$ lead to a set of two equations:

$$0 = C_2 \left[\cos(k_n L) - \cosh(k_n L)\right] + C_4 \left[\sin(k_n L) - \sinh(k_n L)\right] \tag{2.34}$$

$$0 = C_2\, k_n \left[-\sin(k_n L) - \sinh(k_n L)\right] + C_4\, k_n \left[\cos(k_n L) - \cosh(k_n L)\right] \tag{2.35}$$

Arguing that this system of equations has non-zero solutions only if its determinant is zero we find the so called *frequency equation*:

$$\cos(k_n L)\, \cosh(k_n L) = 1 \tag{2.36}$$

This equation needs to be solved numerically, the first three roots are shown in table 2.1. Consequently we can also determine the ratio $\frac{C_2}{C_4}$ for each solution. The calculated ratios can be found in table 2.2. Although they are close to -1 and converge quickly to this value for higher order modes, the values in the table must be taken when calculating the mode shapes for the final result is very sensitive to small variations in $\frac{C_2}{C_4}$. A similar analysis for hinged-hinged beams leads to $C_1 = C_2 = 0$ and a much simpler frequency equation (the solutions are the multiples of π and $\frac{C_3}{C_4} = 1$):

$$\sin(k_n L)\, \sinh(k_n L) = 0 \tag{2.37}$$

Perhaps somewhat surprisingly it is also possible to calculate the mode shapes of a free-free beam, a beam that is clamped nowhere. It turns out that the free-free beam is having a frequency equation equal to the fixed-fixed case (2.36), but $C_2 = C_4 = 0$ now. We will continue our discussion of free-free beams when analyzing clamping losses in mechanical resonators (see subsection 2.6.2).

Using the definition of k_n (2.33) we find the mechanical resonance frequencies of the beam ($p_i = k_i L$ is a constant from table 2.1).:

$$\omega_i = \frac{p_i^2}{L^2} \sqrt{\frac{EI}{\rho S}} \tag{2.38}$$

By consequence fixed-fixed beams result in higher resonance frequencies compared to hinged-hinged ones. We can rewrite the general formula (equa-

	$frequency\ equation$	k_1L	k_2L	k_3L
fixed/fixed	$\cosh(x)\cos(x) = 1$	4.730	7.853	10.996
hinged/hinged	$\sinh(x)\sin(x) = 0$	π	2π	3π
free/free	$\cosh(x)\cos(x) = 1$	4.730	7.853	10.996
free/fixed	$\cosh(x)\cos(x) = -1$	1.875	4.694	7.855
free/hinged	$\tanh(x) = \tan(x)$	3.927	7.069	10.210
fixed/hinged	$\tanh(x) = \tan(x)$	3.927	7.069	10.210

Table 2.1: Consecutive solutions of the frequency equation for fixed,hinged and free boundary conditions

	mode 1	mode 2	mode 3
fixed/fixed ($\frac{C_2}{C_4}$)	-1.01781	-0.99922	-1.00003
hinged/hinged ($\frac{C_3}{C_4}$)	1	1	1
free/free ($\frac{C_1}{C_3}$)	-1.01781	-0.99922	-1.00003

Table 2.2: Ratio $\frac{C_2}{C_4}$, $\frac{C_1}{C_2}$ and $\frac{C_1}{C_3}$ for the fixed-fixed, hinged-hinged and free-free vibration modes of table 2.1.

tion 2.32) for the dynamic mode profile $X(x)$:

$$X(x) = C_1[\cos(p_i\frac{x}{L}) + \cosh(p_i\frac{x}{L})] + C_2[\cos(p_i\frac{x}{L}) - \cosh(p_i\frac{x}{L})] + \tag{2.39}$$

$$C_3[\sin(p_i\frac{x}{L}) + \sinh(p_i\frac{x}{L})] + C_4[\sin(p_i\frac{x}{L}) - \sinh(p_i\frac{x}{L})] \tag{2.40}$$

We see that the mode shape is only dependent on the p_i parameter (which is only determined by the type of boundary conditions) and a generalized position coordinate $\frac{x}{L} = x'$. With the constants in tables 2.1 and 2.2 we can finally construct the different vibrational mode shapes. Since we could only determine the ratio of the two remaining constants we have no amplitude and we only know the mode shapes up to a proportionality constant. This is not surprising since in equation 2.30 no real load is present and we only considered unforced vibration. We choose the proportionality constant in such a way that the maximum value of $X(x) = 1$. With this choice the beam vibration $a(x,t)$ can in fact be expressed as $X_{max}X(x)f(t)$ with X_{max} the amplitude of vibration. The ground vibrational mode is shown

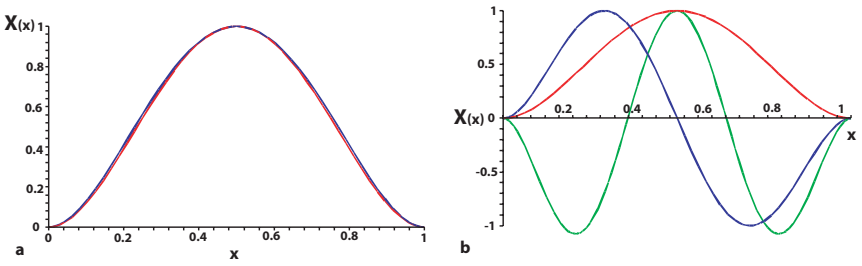

Figure 2.9: **Static and dynamic mode profiles for a beam with unit length. a**, Dynamic ground mode (red curve) vs. static deflection profile (blue curve). A great similarity between both curves is observed. **b**, First (red curve), second (blue curve) and third order (green curve) normalized dynamic mode shapes.

together with the static deflection profile in Fig. 2.9a. The first three normalized fixed-fixed mode shapes $X(x)$ are shown in Fig. 2.9b.

It is striking that the dynamic behavior of a spatially distributed beam is controlled by a set of scalar values ω_n. We already know from subsection 2.2.6 that also the beam stiffness can be described by a scalar value k (equations 2.16 and 2.17), suggesting the possibility of a lumped parameter model for the mechanical beam properties.

2.5 Lumped parameter model

2.5.1 Harmonic oscillator

A lumped parameter model is in fact a simplified mathematical description of a physical system. Spatially distributed variables of the system are represented as single scalars instead, hence reducing drastically the complexity of the system analysis. A famous example can be found in electronics where lumped elements (resistors, capacitors, inductances, etc.) are widely used to facilitate the analysis of electrical circuits. In this section we review a lumped parameter model that describes beam vibrations.

We will start our analysis by looking at a point-mass m on a perfect spring with spring constant k and a position coordinate $A(t)$ (Fig. 2.10a). The equation of motion is in this case $kA + m\ddot{A} = 0$. We employ the classical point notation that denotes a derivative for time. The point mass in this case exhibits a harmonic oscillation $A(t) = A_0 \sin(\omega t + \phi)$ with A_0 and ϕ constants to be determined by the initial conditions (position and

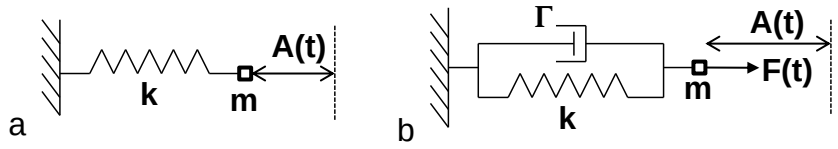

Figure 2.10: **Mass on a spring. a**, Without damping. **b**, With a damper and a harmonic excitation force F(t).

velocity of the point mass). The natural frequency of the oscillations is given by:

$$\omega = \sqrt{\frac{k}{m}} \tag{2.41}$$

Both the beam's effective spring constant and the resonance frequencies of the vibrational modes of the beam have already been introduced. In order to map the Euler beam equation to the simple harmonic oscillator model we only need to introduce an effective mass m_{eff} consistent with the chosen definition of k_{eff} in the previous subsection.

2.5.2 Effective modal mass

When we defined the effective spring constant for the static deflection (subsection 2.2.6) we chose to take the position coordinate exactly in the middle of the beam profile at the point of maximum deflection and accepted the behavior of the beam in this point ($x = \frac{L}{2}$) as a sufficient description for the behavior of the total beam. Also for the dynamic beam profiles $X_{max}X(x)$ (equation 2.32) it makes sense to take the point of maximum deflection (exactly in the middle for the uneven modes of double fixed and hinged beams) to describe the behavior of the total beam. Also the beam's mass is not confined to this point but distributed over the length of the beam. By consequence the total mass will not be displaced over a distance X_{max}, but on average the mass will displace less than X_{max}. Similar to the definition of the effective spring constant it is useful to define an effective point mass representing the distributed beam mass [6]. For a mass-on-a-spring system conservation of energy requires the maximum potential energy to be equal to the maximum kinetic energy:

$$\frac{kA_0^2}{2} = \frac{m(\frac{\mathrm{d}A(t)}{\mathrm{d}t}|_{max})^2}{2} = \frac{mA_0^2\omega^2}{2} \tag{2.42}$$

Arguing that conservation of energy should also hold in the distributed system we can write down the same balance for a beam with profile $a(x,t) =$

$f(t)X_{max}X(x)$:

$$\frac{kX_{max}^2}{2} = \frac{\rho S \int_0^L \dot{a}(x/L)^2|_{max}\mathrm{d}x}{2} = \frac{\rho S L X_{max}^2 \omega_n^2 \int_0^1 X(x')^2\mathrm{d}x'}{2} = \frac{m_{eff}X_{max}^2\omega^2}{2} \tag{2.43}$$

Noting that $\rho SL = m$ is the total mass of the beam we see a great similarity between equations 2.42 and 2.43. The beam mass m however is scaled with a factor, so we can define the effective (modal) mass:

$$m_{eff} = m\int_0^1 X(x')^2\mathrm{d}x' \tag{2.44}$$

This scaling factor is in principle only determined by the boundary conditions and can be found in table 2.3 for the double fixed and double hinged case:

	$\frac{m_{eff,1}}{m}$	$\frac{m_{eff,2}}{m}$	$\frac{m_{eff,3}}{m}$
fixed/fixed	0.397	0.439	0.506
hinged/hinged	0.5	0.5	0.5

Table 2.3: Scaling factors for the effective modal masses of the first three modes (double fixed and double hinged beams)

2.5.3 Damped harmonic oscillator

In practice the pure harmonic oscillator model is not a realistic mathematical model for beam oscillations because several loss factors will damp the motion. In the context of this work we are mainly interested in lossy mechanical oscillators driven by a harmonically varying force so we add a damping term $\Gamma\dot{A}(t)$ (the frictional damping term with damping factor Γ is proportional to the velocity) and a force term $F\sin(\omega t)$ to the harmonic oscillator equation: $kA(t) + \Gamma\dot{A}(t) + m\ddot{A}(t) = F\ \sin(\omega t)$ (Fig. 2.10b). The solution of this differential equation will result in the sum of an exponentially decaying (with time) transient solution and a harmonically varying steady-state solution. Since we are only interested in the harmonic steady-state solution (our experimental work in chapter 5 employs harmonic force

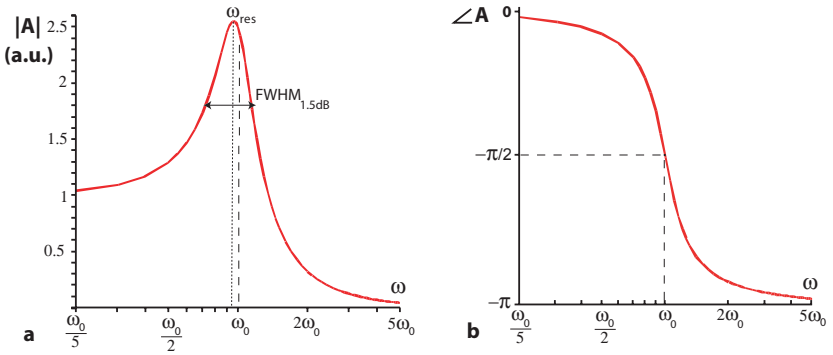

Figure 2.11: **Complex response around ω_0 of a damped harmonic oscillator with $\frac{F}{k} = 1$ and $\zeta = 0.2$ so $Q_{mech} = 2.5$. a**, Amplitude response diagram $|A|$. **b**, Phase response diagram $\angle A$

excitation) we can rewrite the differential equation with F and A being complex quantities (phasor notation for sine waves).

$$kA + \Gamma j\omega A + m(j\omega)^2 A = F \tag{2.45}$$

Substituting the natural frequency $\omega_0 = \sqrt{\frac{k}{m}}$ and introducing the damping constant $\zeta = \frac{\Gamma}{2m\omega_0}$ we can easily solve for A [7]:

$$A = \frac{F}{m[(\omega_0^2 - \omega^2) + 2\zeta j\omega\omega_0]} \tag{2.46}$$

The absolute value of this amplitude can also be written as:

$$|A| = \frac{F}{k}\sqrt{\frac{1}{(1-\frac{\omega^2}{\omega_0^2})^2 + \frac{\omega^2}{\omega_0^2 Q^2}}} = \frac{F}{k}\chi_{MECH}(\omega) \tag{2.47}$$

$\chi_{MECH}(\omega)$ is the frequency dependent mechanical susceptibility with $\chi_{MECH}(\omega_0)$=Q, $\chi_{MECH}(0)$=1 and $\chi_{MECH}(\infty)$=0

Since the vibrational response A is a complex quantity we can plot its phase and amplitude in Fig. 2.11. We note that in the low frequency

limit the amplitude converges to a constant value: ($\frac{F}{m\omega_0^2} = \frac{F}{k}$) i.e. the static response predicted by Hooke's law. In this low frequency limit the vibration is also in phase with its driving force. Around the natural frequency ω_0 the amplitude shows a lorentzian peak and lags behind over $\frac{\pi}{2}$ compared to the driving force. The maximum amplitude however is found at a slightly lower driving frequency $\omega_{res} = \omega_0\sqrt{1-2\zeta^2}$. In Fig. 2.11 we have chosen $\zeta = 0.2$ to have a clear distinction between ω_{res} and ω_0. However most of the structures discussed in this work are strongly underdamped ($\zeta \ll 1$) and $\omega_{res} \approx \omega_0$. In the high frequency limit the amplitude decays quickly and the beam moves in counter phase with its driving force. The quality factor of a resonator is an important parameter to assess (optical, electrical, mechanical) oscillators. It is defined as:

$$Q = 2\pi \frac{\text{energy stored}}{\text{energy dissipated per cycle}} \tag{2.48}$$

The energy stored in the mass-spring-damper system equals $\frac{kA_{max}^2}{2}$ while the energy dissipated through the drag force $F_{drag} = \Gamma\dot{A}(t)$ in a period T equals $\int_0^T F_{drag}(t)\dot{A}(t)\mathrm{d}t = \Pi A_{max}^2\omega_0\Gamma$. Substitution in equation 2.48 yields a simple expression for Q_{mech}:

$$Q_{mech} = \frac{1}{2\zeta} \tag{2.49}$$

Again for small ζ we can see with equation 2.47 that Q_{mech} is approximately equal to $\frac{\omega_{res}}{\Delta\omega_{1.5dB}}$. We define $\Delta\omega_{1.5dB} = \omega_{1.5dB,high} - \omega_{1.5dB,low}$ where $\omega_{1.5dB,low}$ and $\omega_{1.5dB,high}$ are the frequencies where the amplitude has dropped over $1.5\,dB$ compared to the maximum peak amplitude. Also following relation holds: $\omega_{1.5dB,low} < \omega_{res} < \omega_{1.5dB,high}$. Unless explicitly mentioned otherwise we use optical dB ($x_{dB} = 10 \times^{10} \log(x)$) in this work so $|A(\omega_{1.5dB,high})| = |A(\omega_{1.5dB,low})| = \frac{|A(\omega_{res})|}{\sqrt{2}}$. Q_{mech} can thus be quickly estimated from a frequency response measurement.

2.6 Damping mechanisms

In order to complete our lumped parameter model in the previous section we have introduced a damping factor Γ without specifying the physical mechanisms that induce losses. In mechanical resonators several energy dissipation mechanisms can be discerned, among which gas damping, clamping losses and intrinsic losses are the most important ones [8]. To

each of this mechanisms a separate damping constant ζ (and hence a separate Q-factor) can be attributed. The overall Q_{mech} is a result of the addition of several loss mechanisms:

$$Q_{mech}^{-1} = Q_{gas}^{-1} + Q_{clamp}^{-1} + Q_{int}^{-1} + ... \tag{2.50}$$

The largest damping factor (smallest Q) will dominate the overall Q_{mech}. In general it is increasingly difficult to achieve high Q's for higher mechanical resonance frequencies.

2.6.1 Gas damping

At low pressures the resonator dissipates energy through collisions with individual gas molecules [9]. A quality factor due to gas dissipation can be determined as [10] $Q_{gas} \approx \frac{m_{eff}\omega_0\sqrt{k_B\,T/m}}{pS}$ (m the individual molecule mass, T temperature and $k_B = 1.38{\times}10^{-23}JK^{-1}$ the Boltzmann constant, S the surface area of the resonator) so the damping scales linearly with the pressure p. At higher pressures a viscous dissipation regime is encountered and $Q_{gas} \sim p^{\frac{-1}{2}}$.

The gas damping mechanism can in principle be canceled easily by placing the mechanical resonator in a vacuum environment. On the drawback side certain applications like gas- and biosensors typically require contact of the resonator with a gas or fluid. High frequency oscillators however are in general less sensitive to gas damping and maintain a considerable Q_{mech} even at ambient conditions [11, 13]. The reduced sensitivity of high frequency oscillators to gas damping can be explained with high frequency nanofluidics theory [12]. In fact gas damping shows cut off behavior when the mechanical oscillation frequency exceeds a certain cut off frequency:

$$\omega_{mech} > 1/\tau_{relax} \tag{2.51}$$

τ_{relax} is the fluid relaxation time. Within the context of this model reducing the pressure can in fact be understood as increasing the relaxation time of the fluid. Perfect vacuum conditions correspond to an infinite fluid relaxation time and under these circumstances any resonator frequency will satisfy equation 2.51. Also in the limit of an infinite oscillator frequency no gas damping is present. For air at atmospheric pressure and doubly fixed nanomechanical resonators $\tau_{relax} \approx 2.3\,ns$ was found experimentally [12], so indeed in the GHz region one can expect reduced air damping.

However for mechanical oscillators operating in the MHz region a very significant air damping is expected. In Fig. 2.12 the response of a free-standing fixed-fixed beam is shown for three different air pressures. As

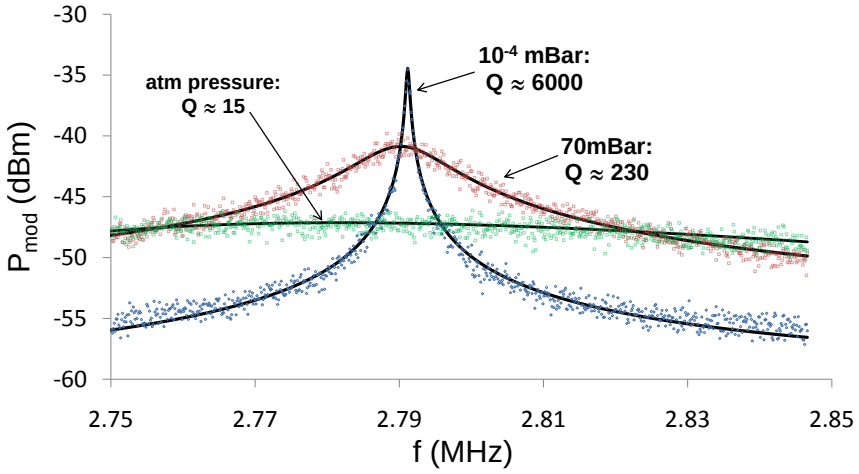

Figure 2.12: **Mechanical quality factor measurement for different ambient pressures** The Lorentzian-like response of a freestanding beam is shown for three different gas pressures. The black solid lines are fits to equation 2.47. This freestanding beam acts as a damped harmonic oscillator with $f_{res} \approx 2.79\,MHz$ At $10^{-4}mBar$ we find $Q \approx 6000$, at $70\,mBar$ $Q \approx 230$ and at atmospheric pressure ($\approx 1013\,mBar$) we obtain $Q \approx 15$.

expected for a damped harmonic oscillator we find Lorentzian-like peaks with $f_{res} \approx 2.79\,MHz$. The black solid lines are fits to equation 2.47 and allow to extract the mechanical Q of the resonator: at $10^{-4}mBar$ we find $Q \approx 6000$. Air damping is completely negligible at this low pressure and the mechanical Q is entirely determined by clamping losses (see next subsection). In fact for pressures lower than $\pm 1\,mBar$ the mechanical Q does not increase much anymore when further reducing pressure. At $70\,mBar$ the overall damping is already mainly determined by gas damping ($Q \approx 230$). At atmospheric pressure ($\approx 1013\,mBar$) the damping is very large and we obtain $Q \approx 15$. Also the shifting of the frequency yielding the largest amplitude ($\omega_{res} = \omega_0\sqrt{1-\frac{1}{2Q^2}}$, see also subsection 2.5.3) to lower frequencies with lower Q can be observed. In chapter 4 section we will discuss in great detail how we have measured the curves in Fig.2.12 and explain why the displacement is expressed in units of dBm. We will also elaborate on the 'brownian' force (in section 4.2) which drives the damped harmonic oscillator in this experiment.

2.6.2 Clamping losses

Another important mechanism is found in clamping losses or acoustic anchor losses [14]. Every resonator needs to be attached to the environment (substrate) at some point and in reality these anchors are never perfectly rigid. Hence a path is created for acoustic energy to radiate away from the resonator at these clamping points into the substrate. This type of losses is difficult to avoid in ordinary doubly fixed/hinged beams. Hence this type of losses will limit our experimental attainable Q's. However clamping losses can be reduced considerably by switching to cleverly designed geometries. Although some analytical models are available [15], in general numerical simulations and experiments [16] are needed to estimate clamping losses adequately. Design of a structure with considerably reduced clamping losses was not possible within the the time frame of this Ph.D thesis. Nevertheless we will briefly explain a possible mechanism for clamping loss reduction in order to give the reader a better understanding for clamping losses and also set the trail for future designs and experiments.

If a beam would have no clamping points it would not be able to leak energy to its environment. At this point we pick up the analysis of the free-free beam in section 2.4 again. Solving the dynamic Euler beam equation with both ends free yields a vibrational ground mode with two nodes where the displacement is zero. The mode profile is drawn in Fig. 2.13a. The zero displacement at these nodes is not enforced by some (imperfect) clamping mechanism but it is rather a natural consequence of the (perfectly) free

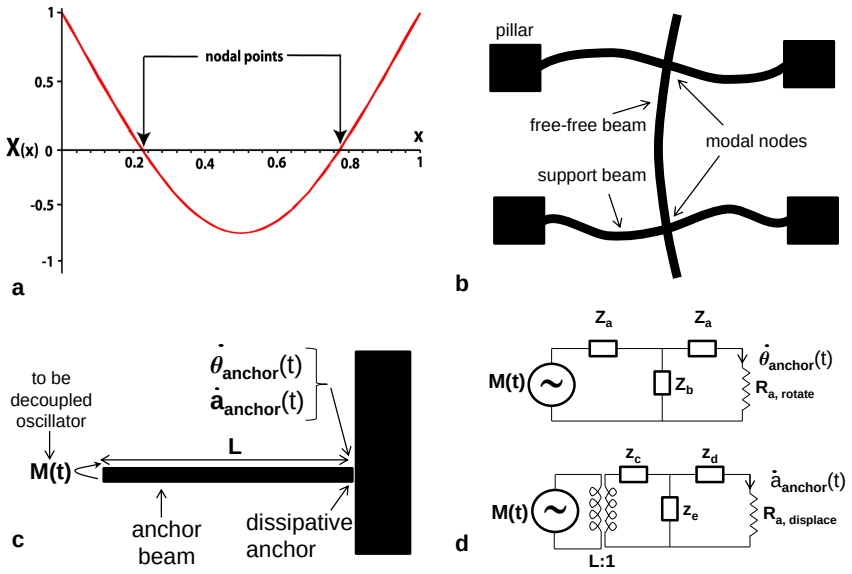

Figure 2.13: **Modeling clamping losses. a**, Ground mode profile of a free-free beam with indication of the two displacement nodes. **b**, Free-free beam suspended using a second order mode of the anchor beam. **c**, Beam with length L, an imperfect anchor and the bending moment $M(t)$ exerted on the tip of the beam by an external mechanical oscillator. **d**, Equivalent mechanical impedance circuits. The upper (lower) circuit describes the rotational (translational) dissipation caused by the bending moment M(t), the dissipative character of the anchor is modeled through the resistances $R_{a,rotate}$ and $R_{a,displace}$.

boundary conditions, so it seems straightforward to use these nodes to attach the beam to the substrate. The decoupling can be further improved by choosing appropriate dimensions for the support beams. The support structure can be designed such that the resonance frequency of the free-free beam matches a resonance frequency of the supported structure. For example the support beams can be designed such that the nodes of the free-free beam correspond to a node of the second order mode of a fixed-fixed beam (see Fig. 2.13b), hence reducing the coupling to the anchors [17, 18].

It is not so straightforward to understand why matching the to be decoupled frequency to a vibrational mode of the supporting structure is beneficial. To explain this let us think of a mechanical oscillator exhibiting a mechanical mode with a zero displacement node, so mechanical energy can only leak away through rotation if we attach the support beam at the node. However the support beam (or anchor beam) of length L needs to be connected to the substrate at some point (=the non-perfect anchor). This situation is schematically drawn in Fig. 2.13c. In this figure we have made abstraction of the to be decoupled oscillator, it is only represented by a bending moment $M(t)$ exerted at the tip of the anchor beam. The bending moment will result in dissipation through rotation or displacement of the anchor. The anchor beam and its not perfect anchor can be modeled through the impedance networks [19] shown in Fig. 2.13d. We have drawn two circuits: the upper (lower) circuit modeling dissipation through rotation (displacement) at the anchor. Compared to the classical electrical circuitry modeling 'bending moment' $M(t)$ plays the role of 'voltage' while 'angular rotation speed' $\dot{\theta}(t)$ or velocity $\dot{a}(t)$ equals 'current' and the products $M(t)\dot{\theta}(t)$ and $\frac{M(t)}{L}\dot{a}(t)$ have the dimension of power (Watt). The dissipative character of the imperfect anchor is modeled through the resistive impedances $R_{a,rotate}$ and $R_{a,displace}$. They define ohmic relations between the bending moment (or force) applied at the anchor and the rotation (or displacement) of the anchor ($M_{anchor}(t) = R_{a,rotate}\dot{\theta}_{anchor}(t)$ and $F_{anchor}(t) = R_{a,displace}\dot{a}_{anchor}(t)$ respectively).

The elements Z_a, Z_b, z_c, z_d and z_e are assumed to have a perfectly imaginary impedance thus energy can only be stored but not dissipated in these elements. They can be expressed as a function of a parameter α which is defined as:

$$\alpha^4 = \frac{\rho A \omega_0^2 L^4}{EI} \tag{2.52}$$

The exact formulas for $Z_a(\alpha)$, $Z_b(\alpha)$, $z_c(\alpha)$, $z_d(\alpha)$ and $z_e(\alpha)$ can be found in reference [19]. The imaginary impedances will depend on ω_0, the frequency of the AC bending moment that is applied to the tip of the anchor beam. In fact proper design allows the impedance $Z_a + Z_b$ to be zero for a

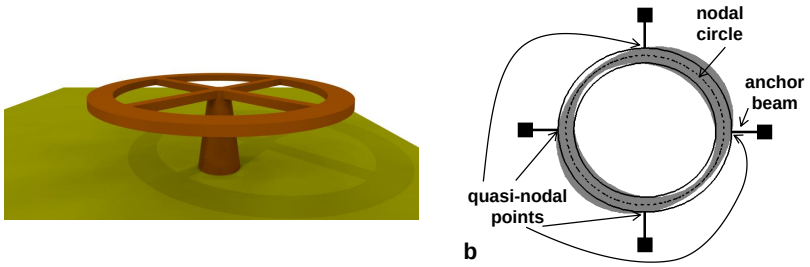

Figure 2.14: **Ring shaped mechanical oscillators. a**, Ring resonator decoupled from the center pillar using spokes. **b**, Fourth-order extensional wine-glass mode [13] in a ring topology. The quarter wavelength beams are attached to quasi-nodal displacement points and decouple rotation. The mechanical mode expands and contracts around the nodal circle.

certain vibration frequency ω_0. For this particular frequency the dissipative resistor is short-circuited and decoupled from the rest of the circuit. No current flows through the resistor and hence no power is dissipated through rotation of the anchor.

If we require $Z_a + Z_b$ to be zero, we find that α should satisfy:

$$\tanh(\alpha) = \tan(\alpha) \tag{2.53}$$

Requiring $z_c + z_e = 0$ (no dissipation through displacement), we find exactly the same equation for α. Equation 2.52 allows us to design the anchor beam. If we insert for α a value that satisfies $\tanh(\alpha) = \tan(\alpha)$, we just need to substitute the (to be decoupled) oscillator frequency in 2.52. Then the desired geometrical beam properties L,I (moment of inertia) and S (beam cross-section) can easily be determined for given material parameters (E, ρ).

In fact equation 2.53 corresponds to the frequency equation of a hinged-fixed beam (see table 2.1). In other words the frequency of the to be decoupled mechanical oscillator matches exactly the frequency for which the anchor beam would be in resonance if it were a hinged-fixed beam. Indeed a hinged-fixed beam allows rotation at one end and shows no displacement or rotation at its other end so we can understand intuitively that the rotation of the external oscillator exerted on the 'hinged' end of the anchor beam is of no influence at all any more. In other words a beam with one hinged end shows 'intrinsic' displacement/rotation nodes at a given frequency after a certain distance L.

The above described technique is commonly referred to as the 'quarter wavelength' technique. The name is referring to the quarter wave-

length impedance transformation also found in classical transmission line theory. One can also think of the decoupling anchor beam as a transmission line with zero input impedance, hence all power is reflected back into the resonator. Summarized the quarter wavelength technique can be exploited to achieve mechanical oscillators with high Q in free-free beams [20], but in fact its application potential is much wider. A variant of the technique has recently been applied successfully in ring shaped mechanical resonators where spokes have been applied to decouple a mechanical mode from the support, resulting in a Q of 50000 for a resonance frequency of $24.386\,MHz$ [16].

The mechanical modes we have discussed so far are bending modes or flexural modes. The beam's local center of mass is displaced when moving. It was found that so called bulk acoustic modes that do not change their local center of mass seem to be less sensitive to clamping losses. Promising topologies to achieve high Q high frequency oscillators are the hollow disk resonator [21] and extensional wine-glass mode ring resonator [13]. For these mechanical modes the center of mass does not change during vibration but remains in a nodal circle and the material rather contracts and expands around this nodal circle. Such a mode is shown schematically in Fig. 2.14. Decoupling this mode from its anchor using quarter wavelength beams allowed a Q of 2800 for a resonance frequency as high as $1.52\,GHz$ and $Q = 4650$ for $651\,MHz$ [13]. The latter Q was showing only a small reduction when measured in air ($Q = 4550$), indicating that the contribution of gas damping to the global Q is indeed diminishing for higher frequency oscillators.

2.6.3 Intrinsic losses

When looking at intrinsic losses we should discriminate between losses in a perfect crystal lattice or losses in a real lattice with bulk and surface defects. The losses in a perfect crystal are fundamental and limit the ultimately achievable quality factors. Some known fundamental loss mechanisms include thermo-elastic damping and losses due to phonon-electron and phonon-phonon interactions [22]. The dissipation due to crystal imperfections are not fundamental and might be further reduced by proper engineering. When looking into the relative influence of bulk and surface defects unavoidably the size of the mechanical structures comes into play. In literature evidence can be found that surface defects contribute more dominantly to losses in mechanical resonators with shrinking size [23, 24]. In fact even a rough empirical linear decrease in maximum achievable Q with volume-to-surface ratio is found [25]. Surface treatment and passi-

vation experiments are paving the way to the highest possible quality factors [26–28].

Considering the influence of scaling on the damping we can also ask ourselves the question to which extent continuum mechanics theory can be pushed into the (sub)nanoscale region. Simulations and experiments show that the continuum theory (sections 2.4 and 2.2) should hold for structures down to at least a few tens of lattice constants in cross-section [25, 29].

2.7 Non-linear mechanics

2.7.1 Mathematical description

When a beam is undergoing large amplitude vibrations the beam might respond in a non-linear way. We will briefly discuss non-linear oscillators governed by equations having the form:

$$m\ddot{A} + \Gamma\dot{A} + k_0(1 + k_1A + k_2A^2)A = F\,\cos(\omega t) \tag{2.54}$$

In this equation the spring constant k is replaced by a polynomial term $k_0\,(1 + k_1A + k_2A^2)$ hence introducing a quadratic and cubic term in the equation of motion. If we set $k_1 = 0$ only the cubic non-linearity remains and we obtain the classical Duffing oscillator equation. It can be shown that in such case the steady-state vibration amplitude around primary resonance can be found by solving the following equation [30]:

$$\frac{9}{16}(\frac{k_2}{k_0})^2A^6 - \frac{3}{2}\sigma\frac{k_2}{k_0}QA^4 + (\sigma^2 + 1)A^2 - \frac{F^2Q^2}{k_0^2} \tag{2.55}$$

Instead of using the excitation frequency ω we have introduced the detuning parameter σ which quantitatively describes the nearness of ω to ω_0 such that $\omega = \omega_0(1 + \sigma\frac{1}{2Q})$. Equation 2.55 is cubic in A^2 and thus its three roots can be calculated analytically. Depending on the numeric values of the parameters however either one root is real (with the two others complex conjugate valued) or all three roots are real.

In Fig. 2.15 a the solution is shown for $\frac{FQ}{k_0} = 1$,$k_0 = 0.001\,Nm^{-1}$,$Q = 1000$ and $k_2 = -10^{-18}m^{-2}$. We find a curve very similar to Fig. 2.11a for the ordinary damped harmonic oscillator indicating that the effect of k_2 is negligible for this small value. The different colors indicate that the solutions originate mathematically from different roots. Also the phase relation in Fig. 2.16a is identical to Fig. 2.11b. It can be found by solving the

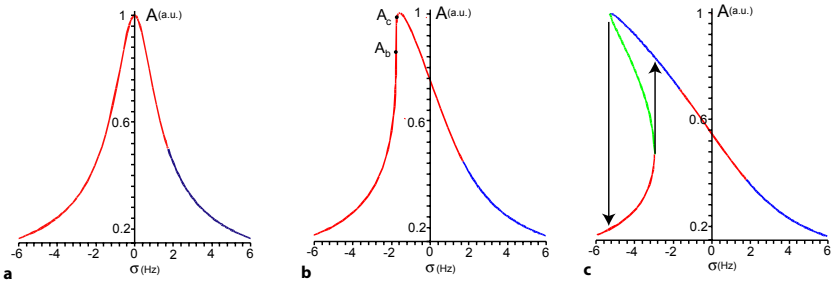

Figure 2.15: **Non-linear amplitude response. Different colored curves origin from mathematically different roots.** **a**, Quasi-linear amplitude response for $k_2 = -10^{-18}m^{-2}$. **b**, Amplitude response for $k_2 = -2.07 \times 10^{-15}m^{-2}$ with onset of bifurcation. A_b is the bifurcation amplitude and A_c the critical amplitude. **c**, Bistable amplitude response for $k_2 = -7.0 \times 10^{-15}m^{-2}$. The arrows mark the jump points.

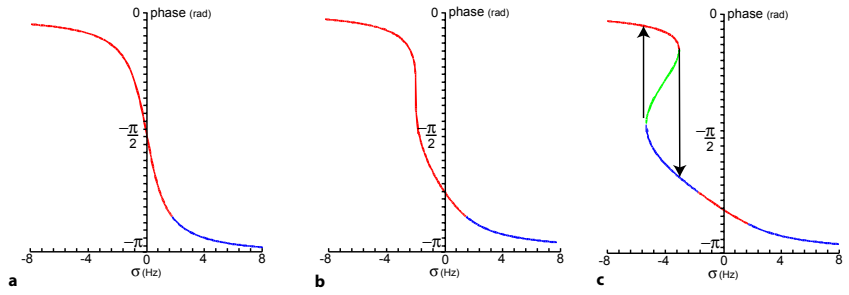

Figure 2.16: **Non-linear phase response. Different colored curves origin from mathematically different roots.** **a**, Quasi-linear phase response for $k_2 = -10^{-18}m^{-2}$. **b**, Phase response for $k_2 = -2.07 \times 10^{-15}m^{-2}$ with onset of bifurcation. **c**, Bistable phase response for $k_2 = -7.0 \times 10^{-15}m^{-2}$. The arrows mark the edges of the bistability region.

following set of equations for ϕ [30]:

$$A = \frac{FQ}{k_0}\sin(\phi) \tag{2.56}$$

$$A\sigma - \frac{3k_2Q}{4k_0} = -\frac{FQ}{k_0}\cos(\phi) \tag{2.57}$$

The picture changes drastically for $k_2 = -2.07 \times 10^{-15}m^{-2}$. Due to this negative value the resonance peak is shifting to lower frequencies (spring softening) and the lower frequency edge steepens marking the onset of bifurcation when the critical amplitude $A_c = \frac{2}{\sqrt{3Q\frac{3}{8}k_2\sqrt{3}}}$ is reached (Fig. 2.15b). A similar pattern can be seen in the phase relation (Fig. 2.16b). The amplitude at the point of bifurcation is slightly lower $A_b = A_c\frac{\sqrt{3}}{2}$. A positive third order non-linearity would result in curves that bends towards higher frequencies (curves shown in Fig. 2.15b and 2.16b mirrored around the $\sigma = 0$ axis). For $k_2 = -7.0 \times 10^{-15}m^{-2}$ a region is found where three possible amplitudes correspond with one driving frequency. However the solution plotted in green is not stable and a bistable region is created (Fig. 2.15c and 2.16c). Which of the two possible amplitudes is obtained when performing a frequency sweep depends on whether we approach the bistability region from the high or low frequency side. When entering again an area with only one solution the vibration amplitude will undergo a sudden stepwise change (see arrows in Fig. 2.15c and 2.16c). In the bistability region the actual vibration amplitude is dependent on the past hence the system possesses a memory function and is said to show hysteresis.

It can be shown that for driving frequencies around ω_0 the above analysis for cubic non-linearities can be easily extended towards quadratic non-linearities [30]. The effect of the quadratic non-linearity can be modeled as a cubic non-linearity with effective $k_2 = -\frac{10}{9}k_1^2$. Hence the quadratic non-linearity always has a spring softening influence irrespective of its sign.

2.7.2 Physical causes of non-linearity

When the beam is undergoing large vibrations the material will be stretched resulting in strain and an accompanying stress, which increases the stiffness of the beam. Using the variational model we developed in subsection 2.3.2 we can establish a simple model for mechanical spring hardening in a fixed-fixed beam. Following equation 2.28 we find a cubic non-linearity with $\frac{k_{stress}}{k_{geom}} = k_2 = \frac{3}{4}t^{-2}$ where t is thickness of the beam. We see that this type of non-linearity becomes important when the vibration amplitude reaches values, which are significant compared to the thickness of the beam.

Other non-linear mechanisms, which are related to the beam mechanics include material non-linearities [31]. However non-linearity is also encountered when the exerted force is dependent on the position coordinate of the beam: $F(A) = F(0) + \frac{\mathrm{d}F}{\mathrm{d}A}|_{A=0}A + \frac{\mathrm{d}^2F}{\mathrm{d}F^2}|_{A=0}\frac{A^2}{2} + \frac{\mathrm{d}^3F}{\mathrm{d}A^3}|_{A=0}\frac{A^3}{6}$ Substituting this expression in 2.54 we can see that the first, second and third order derivatives actually correspond to an effective spring constant, quadratic and cubic non-linearity respectively. In the case of a parallel plate capacitor for example in accordance with Coulomb's law the exerted actuation force on the plates typically varies with the inverse square of the distance between the plates ($\sim \frac{1}{(g-A)^2} \approx \frac{1}{g^2}(1 + 2\frac{A}{g} + 3\frac{A}{g}^2 + 4\frac{A}{g}^3)$) resulting in multiple higher order non-linearities (electrical spring softening). We will later see (see chapter 5) that the gradient optical force varies typically exponentially with the distance between two objects, thus also resulting in non-linear behavior. Finally non-linearity can also be generated in the motion transduction [32], which will be further discussed in chapter 4.

For a lot of applications non-linearities are undesired and the practical maximum operation amplitude is therefore limited and should be sufficiently smaller than A_b, limiting the maximum stored energy in the device to ($E_{max} < \frac{kA_b^2}{2}$) [33]. The power handling capacity however is an important spec for reference oscillators in wireless applications. In sensors non-linearities might limit the dynamic range of the sensor [34]. Therefore cancelation schemes were investigated with non-linearities of the softening and hardening type annihilating each other [35]. It was also found that the power handling capacity of the longitudinal (bulk acoustic) vibrational modes of a beam is orders of magnitudes superior to its flexural modes [33]. However non-linearity might also be usefully applied for the construction of chaotic nanomechanical systems [36].

2.7.3 Summary

Summarizing this chapter we have learnt —starting from the static and dynamic Euler beam equation— that the nanomechanical oscillators we will fabricate and characterize in this work can be described by a powerful lumped parameter model: the damped harmonic oscillator. In addition we have identified the main mechanisms (air damping, clamping losses) that will control the damping of our structures. Finally non-linearity has been added to the lumped parameter model which will allow us to fully describe, analyze and understand the mechanical behavior of our optomechanical devices.

Bibliography

[1] Stephen D. Senturia. *Microsystem design*, chapter 5. Kluwer Academic Publishers, Norwell, MA, USA, 2001.

[2] Stephen D. Senturia. *Microsystem design*, chapter 9. Kluwer Academic Publishers, Norwell, MA, USA, 2001.

[3] S. Timoshenko. *Vibration problems in engineering*, chapter 5. D. Van Nostrand Company, Inc, New York, NY, USA, 1937.

[4] Stephen D. Senturia. *Microsystem design*, chapter 10. Kluwer Academic Publishers, Norwell, MA, USA, 2001.

[5] Y. Okada and Y. Tokumaru. Precise determination of lattice-parameter and thermal-expansion coeffcient of silicon between 300-K and 1500-K . *Journal of Applied Physics*, 56(2):314–320, 1984.

[6] W.T. Thomson. *Theory of Vibration with Applications*, chapter 2. Prentice Hall, Englewood Cliffs, NJ, USA, 1981.

[7] John A. Pelesko and David H. Bernstein. *Modeling MEMS and NEMS*, chapter 3. Chapman and Hall/CRC, Boca Raton, FL, USA, 2003.

[8] Mohammad I. Younis. *Modeling and Simulation of Microelectromechanical Systems in Multi-Physics Fields*. PhD thesis, Virginia Polytechnic Institute and State University, Blacksburg, Virginia, 2004.

[9] Gabriel M. Rebeiz. *RF MEMS: Theory, Design, and Technology*, chapter 3.

[10] F.R. Blom, S. Bouwstra, M. Elwenspoek, and J.H.J. Fluitman. Dependence of the quality factor of micromachined silicon beam resonators on pressure and geometry. *Journal of Vacuum Science & Technology B*, 10(1):19–26, 1992.

[11] Mo Li, H. X. Tang, and M. L. Roukes. Ultra-sensitive NEMS-based cantilevers for sensing, scanned probe and very high-frequency applications. *Nature Nanotechnology*, 2(2):114–120, 2007.

[12] D. M. Karabacak, V. Yakhot, and K. L. Ekinci. High-frequency nanofluidics: An experimental study using nanomechanical resonators. *Physical Review Letters*, 98(25), 2007.

[13] Y. Xie, S. Li, Y. Lin, Z. Ren, and C.T.C. Nguyen. 1.52-GHz micromechanical extensional wine-glass-mode ring resonators. *IEEE Transactions on Ultrasonics Ferroelectrics and Frequency Control*, 55(4):890–907, 2008.

[14] D.M. Photiadis and J.A. Judge. Attachment losses of high Q oscillators. *Applied Physics Letters*, 85(3):482–484, 2004.

[15] Z.L. Hao, A. Erbil, and F. Ayazi. An analytical model for support loss in micromachined beam resonators with in-plane flexural vibrations. *Sensors and Actuators A-Physical*, 109(1-2):156–164, 2003.

[16] G. Anetsberger, R. Riviere, A. Schliesser, O. Arcizet, and T. J. Kippenberg. Ultralow-dissipation optomechanical resonators on a chip. *Nature Photonics*, 2(10):627–633, 2008.

[17] W.T. Hsu, J.R. Clark, and C.T.C. Nguyen. Q-Optimized lateral free-free beam micromechanical resonators. In Obermeier, E, editor, *Transducers '01: Eurosensors XV, Digest of technical papers, Vols 1 and 2*, pages 1110–1113, 2001. 11th International Conference on Solid-State Sensors and Actuators, Munich, Germany, Juin 10-14, 2001.

[18] M. Palaniapan and Lynn Khine. Nonlinear behavior of SOI free-free micromechanical beam resonator. *Sensors and Actuators A-Physical*, 142(1):203–210, 2008. 20th Eurosensors Conference, Goteborg, Sweden, SEP 17-20, 2006.

[19] M. Konno and H. Nakamura. Equivalent electrical network for transversely vibrating uniform bar. *Journal of the Acoustical Society of America*, 38(4):295–304, 1965.

[20] K. Wang, A.C. Wong, and C.T.C. Nguyen. VHF free-free beam high-Q micromechanical resonators. *Journal of Microelectromechanical Systems*, 9(3):347–360, 2000.

[21] S.S. Li, Y.W. Lin, Y. Xie, Z.Y. Ren, and C.T.C. Nguyen. Micromechanical hollow-disk ring resonators. In *MEMS 2004: 17TH IEEE International Conference on Micro-electro-mechanical systems, Technical Digest*, Proceedings: IEEE Micro-electro mechanical systems Workshop, pages 821–824, 2004. 17th IEEE International Conference on Micro Electro Mechanical Systems, Maastricht, Netherlands, Jan 25-29, 2004.

[22] R. Lifshitz and M.L. Roukes. Thermoelastic damping in micro- and nanomechanical systems. *Physical Review B*, 61(8):5600–5609, 2000.

[23] J.L. Yang, T. Ono, and M. Esashi. Energy dissipation in submicrometer thick single-crystal silicon cantilevers. *Journal of Microelectromechanical Systems*, 11(6):775–783, 2002.

[24] J.L. Yang, T. Ono, and M. Esashi. Surface effects and high quality factors in ultrathin single-crystal silicon cantilevers. *Applied Physics Letters*, 77(23):3860–3862, 2000.

[25] K.L. Ekinci and M.L. Roukes. Nanoelectromechanical systems. *Review of Scientific Instruments*, 76(6), 2005.

[26] Y. Wang, J.A. Henry, A.T. Zehnder, and M.A. Hines. Surface chemical control of mechanical energy losses in micromachined silicon structures. *Journal of Physical Chemistry B*, 107(51):14270–14277, 2003.

[27] Y. Wang, J.A. Henry, D. Sengupta, and M.A. Hines. Methyl monolayers suppress mechanical energy dissipation in micromechanical silicon resonators. *Applied Physics Letters*, 85(23):5736–5738, 2004.

[28] J.A. Henry, Y. Wang, and M.A. Hines. Controlling energy dissipation and stability of micromechanical silicon resonators with self-assembled monolayers. *Applied Physics Letters*, 84(10):1765–1767, 2004.

[29] John A. Pelesko and David H. Bernstein. *Modeling MEMS and NEMS*, chapter 2. Chapman and Hall/CRC, Boca Raton, FL, USA, 2003.

[30] Ali H. Nayfeh and Dean T. Mook. *Nonlinear oscillations*, chapter 4. John Wiley & Sons, Inc., New York, NY, USA, 1979.

[31] V. Kaajakari, T. Mattila, A. Lipsanen, and A. Oja. Nonlinear mechanical effects in silicon longitudinal mode beam resonators. *Sensors and Actuators A-Physical*, 120(1):64–70, 2005.

[32] I. Kozinsky, H. W. Ch. Postma, I. Bargatin, and M. L. Roukes. Tuning nonlinearity, dynamic range, and frequency of nanomechanical resonators. *Applied physics letters*, 88(25), 2006.

[33] V Kaajakari, T Mattila, A Oja, and H Seppa. Nonlinear limits for single-crystal silicon microresonators. *Journal of Microelectromechanical Systems*, 13(5):715–724, 2004.

[34] H.W.C. Postma, I. Kozinsky, A. Husain, and M.L. Roukes. Dynamic range of nanotube- and nanowire-based electromechanical systems. *Applied physics letters*, 86(22), 2005.

[35] L. C. Shao, M. Palaniapan, and W. W. Tan. The nonlinearity cancellation phenomenon in micromechanical resonators. *Journal of Micromechanics and Microengineering*, 18(6), 2008. 18th European Workshop on Micromechanics (MME 07), Guimaraes, Portugal, SEP 16-18, 2007.

[36] R.H. Blick, A. Erbe, L. Pescini, A. Kraus, D.V. Scheible, F.W. Beil, E. Hoehberger, A. Hoerner, J. Kirschbaum, H. Lorenz, and J. P. Kotthaus. Nanostructured silicon for studying fundamental aspects of nanomechanics. *Journal of Physics-condensed matter*, 14(34):R905–R945, 2002.

3

Fabrication of nanomechanical devices

What I cannot create, I do not understand.
Richard P. Feynman

3.1 Silicon for mechanics

AS we have already mentioned in the first chapter, silicon is the favored semiconductor of CMOS semiconductor industries. Because of its high refractive index it can also be used to create very compact nanophotonic circuits. In addition it shows almost negligible absorption around telecom wavelengths ($\lambda = 1300 - 1620nm$) making it an excellent material for nanophotonics. In the first chapter we already discussed our intention to merge nanophotonics with mechanics to create Nano-OptoMechanical Systems (NOMS), so we need to assess the suitability of silicon for mechanical purposes. We will limit our assessment to single-crystal (=monocrystalline) silicon (c-Si) which is from mechanical point of view superior to polycrystalline and amorphous silicon variants and also the material we will use in reality for our fabrication. When discussing silicon in the coming paragraphs and chapters c-Si is meant unless mentioned explicitly otherwise.

3.1.1 Anisotropy of the silicon crystal

When designing mechanical structures in silicon an important aspect we have to deal with is the anisotropy of the crystal. Silicon has a diamond cubic crystal structure [1], other group IV elements including germanium, tin and of course diamond also adopt this structure. In Fig. 3.1a the unit cell of the crystal structure is shown. Copying the unit cell in three dimensions allows reconstruction of the full crystal. We see that eight atoms are placed at the corners and six at the faces of the cubic unit cell (such a structure is called 'face centered cubic' in crystallography). In addition four tetrahedrally bound atoms are located in the bulk of the unit cell so in total we have eight atoms per unit cell ($8\frac{1}{8} + 6\frac{1}{2} + 4 = 8$).

We also defined crystal directions relative to the unit cell and used the conventional square bracket notation for crystal directions (Miller indices [2]). Planes orthogonal to a crystal direction $[i, j, k]$ are referred to as (i, j, k). For example in Fig. 3.1a the $(0, 0, 1)$ plane is marked. Due to crystal symmetry planes with a different index might behave identical. The set of planes that is equivalent to plane (i, j, k) is denoted as $\{i, j, k\}$. In a similar way the set of crystal directions that is equivalent to direction $[i, j, k]$ is denoted as $< i, j, k >$. For example both crystal directions $[1, 1, 0]$ and $[1, \bar{1}, 0]$ (by convention negative indices are written with a bar so $\bar{1}$ instead of -1) are part of the $< 1, 1, 0 >$ class. In fact due to the symmetry the mechanical behavior of silicon can be fully described in three dimensions by a six by six tensor with only three independent non-zero constants. The *compliance* matrix connects the normal and shear stresses with the strains. Oriented to the $\{1, 0, 0\}$ crystal axes (for a compact notation labeled as x,y and z, see Fig.3.1a) the relationship between stresses and strains reads as:

$$\begin{bmatrix} \epsilon_{xx} \\ \epsilon_{yy} \\ \epsilon_{zz} \\ \epsilon_{yz} \\ \epsilon_{zx} \\ \epsilon_{xy} \end{bmatrix} = \begin{bmatrix} S_{11} & S_{12} & S_{12} & 0 & 0 & 0 \\ S_{12} & S_{11} & S_{12} & 0 & 0 & 0 \\ S_{12} & S_{12} & S_{11} & 0 & 0 & 0 \\ 0 & 0 & 0 & S_{44} & 0 & 0 \\ 0 & 0 & 0 & 0 & S_{44} & 0 \\ 0 & 0 & 0 & 0 & 0 & S_{44} \end{bmatrix} \begin{bmatrix} \sigma_{xx} \\ \sigma_{yy} \\ \sigma_{zz} \\ \tau_{yz} \\ \tau_{zx} \\ \tau_{xy} \end{bmatrix} \tag{3.1}$$

The compliance elements take the following values for silicon: $S_{11} = 7.68\,10^{-12}\,Pa^{-1}$, $S_{12} = -2.14\,10^{-12}\,\text{Pa}^{-1}$ and $S_{44} = 12.6\,10^{-12}\,\text{Pa}^{-1}$. Any direction in the crystal can be identified by its 'direction cosines'. Let l,m,n be the cosines of the angles that a particular direction makes with the $[1, 0, 0]$, $[0, 1, 0]$, $[0, 0, 1]$, crystal axes respectively. Young's modulus E_{lmn}

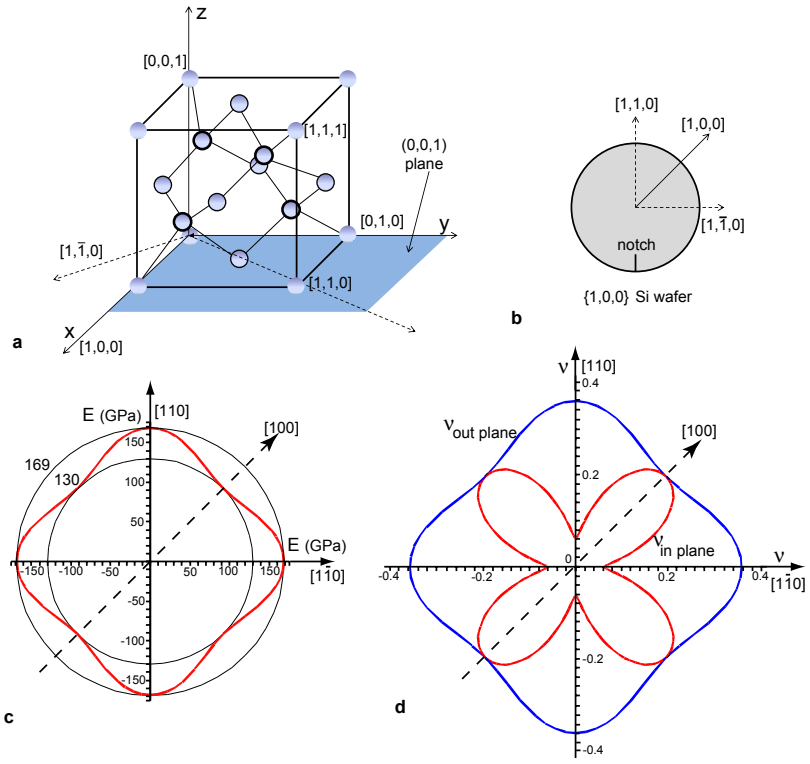

Figure 3.1: **The anisotropic mechanical properties of single-crystal silicon.** **a**, Unit cell of monocrystalline silicon (diamond cubic crystal) with crystal directions and planes indicated. The four tetrahedrally bound atoms in the bulk of the unit cell are drawn with a thicker boundary. **b**, $\{1,0,0\}$ wafer with notch and crystal directions indicated. **c**, Young's modulus in the $\{1,0,0\}$ plane. The circles indicate the extremal values of 130 GPa ($E_{<100>}$) and 169 GPa($E_{<110>}$). **d**, In plane and out of plane Poisson's ratio in the $\{1,0,0\}$ plane.

in a direction defined by the direction cosines l,m,n is then given by [3]:

$$\frac{1}{E_{lmn}} = S_{11}(l^4 + m^4 + n^4) + (S_{44} + 2S_{12})(l^2m^2 + l^2n^2 + m^2n^2) \quad (3.2)$$

Along the $< 1, 0, 0 >$ crystal axes the above formula reduces to $\frac{1}{E_{<100>}} = S_{11}$ and we find $E_{<100>} = 130\,\text{GPa}$. Using formula 3.2 we calculated Young's modulus in the $\{1, 0, 0\}$ plane. This crystal plane in particular is important because the Si wafers we use for our fabrication are $\{1, 0, 0\}$ wafers which means that our structures will lie in the $\{1, 0, 0\}$ plane. The so called 'notch' defines the $< 1, 1, 0 >$ direction in this plane (see Fig. 3.1b). In Fig. 3.1c we see that Young's modulus varies from 169 GPa along the $< 1, 1, 0 >$ axes to 130 GPa along the $< 1, 0, 0 >$ axes, a variation of approximately 23%. The anisotropy is even more distinct when considering Poisson's ratio (see Fig. 3.1d). Poisson's ratio is the ratio of the transverse strain (perpendicular to the applied axial stress) to the axial strain ($\nu = -\frac{\epsilon_{trans}}{\epsilon_{axial}}$). In Fig. 3.1d Poisson's ratio is plotted for in plane and out of plane transverse strain showing large variations. Expressions for Poisson's ratio in terms of direction cosines can be found elsewhere [3]. It is interesting to note that anisotropy is not present in $\{1, 1, 1\}$ wafers since every direction is a $< 1, 1, 0 >$ direction in $\{1, 1, 1\}$ crystal planes. Nevertheless standard $\{1, 0, 0\}$ wafers were used for this work. This is no real issue since our mechanical structures are mainly relatively slender beams oriented parallel or perpendicular to the notch along a $< 1, 1, 0 >$ direction, so we can safely accept Young's modulus to be 169 GPa in the context of this work. However anisotropy should be taken into account when designing for example mechanical resonators with ring topology in $\{1, 0, 0\}$ wafers.

3.1.2 Advantageous mechanical properties

In single crystal form, silicon is an almost perfectly elastic material [4], meaning that when it is flexed there is virtually no plastic deformation or hysteresis. Hence energy dissipation inside the material is very low. In subsection 2.6.3 we have already discussed the importance of intrinsic material losses in the pursuit of ultrahigh Q mechanical resonators so silicon seems one of the best possible materials for this goal. Another aspect which has not been discussed yet is reliability. Its elasticity makes silicon very reliable as it suffers very little from fatigue [5, 6] and can have service lifetimes in the range of billions to trillions of cycles without breaking. Since silicon suffers little from aging also very stable oscillator frequencies can be maintained over years (a frequency shift of $\approx$1 ppm per year has been

. The elastic constants and density for the semiconductors can be found in [8], the numerical values for the metals were taken from [9].

Material	$E\,(GPa)$	$\rho\,(kg\,m^{-3})$	$\sqrt{\frac{E}{\rho}}\,(m\,s^{-1})$
Cu	128	8940	3784
InP	93	4810	4398
GaAs	122	5317	4786
Al	69	2700	5055
Ge	137	5323	5079
Si	169	2329	8518
SiC	450	3210	11861
Diamond	1165	3515	18207

Table 3.1: Young's modulus E, density ρ and ratio $\sqrt{\frac{E}{\rho}}$ of some —for semiconductor industries common— semiconductors and metals. For the semiconductors the modulus for the $< 1, 1, 0 >$ crystal direction was taken. The materials are listed according increasing $\sqrt{\frac{E}{\rho}}$

demonstrated [7] while typically maximum ≈5 ppm is allowed for timing and clock applications). Finally a high Young's modulus and more in particular the high $\sqrt{\frac{E}{\rho}} = 8518\,ms^{-1}$ ratio include another asset. In chapter 2 we have seen that mechanical oscillator resonance frequencies scale with this ratio. In other words compared to materials with a lower ratio, silicon allows higher frequency components for the same geometrical dimensions of the component, hence relaxing fabrication tolerances for commercially interesting GHz components. Some materials that are popular in semiconductor industries are shown for comparison with silicon in table 3.1 [8, 9]:

We see that silicon is only surpassed by silicon carbide (SiC) and diamond. The latter is indeed a superb mechanical material. First of all diamond components can be almost twice as large for the same oscillator frequency, relaxing fabrication tolerances for high frequency components. Moreover although silicon components are known for their excellent long term reliability, the wear life of diamond oscillators is estimated to be 10000 times larger than silicon components [10]. In addition trouble with surface oxides causing surface dissipation and reducing the maximum achievable mechanical quality factors might be avoided. However for this PhD diamond was not an option yet for the fabrication of simple nanophotonic

circuits in diamond is still in its infancy [11].

3.2 Fabrication of passive structures in Silicon-on-Insulator

3.2.1 Deep Ultraviolet Lithography

Most nanophotonic structures today are defined using e-beam lithography, a technique which can handle the resolutions required, but lacks the possibility for large scale fabrication due to long writing times. Other techniques used for the large-scale fabrication of current photonic integrated circuits cannot print the fine details required for nanophotonic structures.

Deep Ultraviolet (DUV) lithography allows both large-scale fabrication and acceptable resolution. On top of these advantages, a large experience with DUV lithography based fabrication is already available in the Photonics Research Group Ghent, the research group which hosted this PhD. Consequently DUV lithography is our preferred fabrication technology to define patterns in the top layer of a silicon-on-insulator (SOI) wafer.
DUV lithography is based on excimer lasers and uses state-of-the-art CMOS-facilities provided by imec. The fabrication of nanophotonic structures in silicon-on-insulator wafers (SOI) using a 248 nm illumination wavelength was first explored in the doctoral work of Wim Bogaerts [12] and Pieter Dumon [13]. A more advanced process using a shorter wavelength (193nm) can resolve single line structures of 100 nm and was developed and fine-tuned in the PhD work of Shankar Kumar Selvaraja [14]. We mainly used this more advanced process to create patterns in a SOI wafer having a top layer of silicon with a thickness of 220 nm and a buried oxide (BOx) layer with a thickness of 2 μm. However some of the earliest structures described in this work were fabricated using the 248 nm wavelength in SOI wafers with a 220 nm top layer and a BOx layer of only 1μm. An extensive discussion of DUV lithography and the subsequent Reactive Ion Etching (RIE) are beyond the scope of this thesis. More details on the 248 nm [15] en 193 nm process [16] can be found elsewhere. From now on we make abstraction of this process and start our process flow with a patterned SOI wafer.

3.2.2 Coupling light into the chip

Before we discuss the fabrication of freestanding structures in an SOI wafer we will briefly discuss an important feature of our passive nanophotonic circuits. If we want to use relatively weak optical gradient forces to actuate nanophotonic waveguides, then at least we need to couple sufficient light

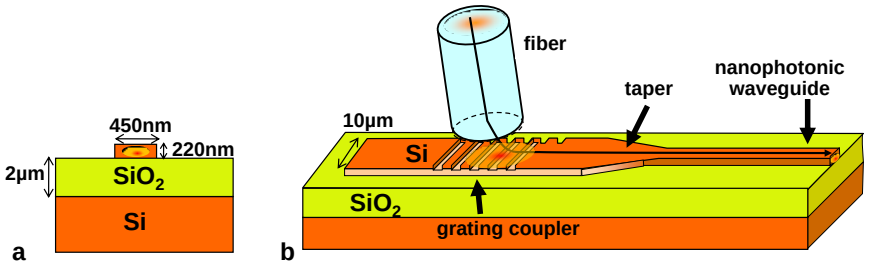

Figure 3.2: **Coupling light into a nanophotonic waveguide. a**, Typical nanophotonic single-mode waveguide cross-section. For some structures in this work a 1 μm (instead of 2 μm) thick buried oxide layer was used. **b**, The grating coupler diffracts light into a 10 μm wide waveguide which tapers through an adiabatic taper to a nanophotonic single-mode waveguide with a typical width of approximately 450 nm.

into the nanophotonic waveguides. Fig. 3.2a is showing a typical single-mode nanophotonic waveguide. Its dimensions (220 nm by 450 nm) are in sharp contrast with the fiber core diameter of a single mode fiber (circle with diameter 9 μm). To keep the losses that arise from this size mismatch at an acceptable level the grating couplers are used [17].

In Fig. 3.2b we see that the light from a tilted fiber (typically 10° tilt) is incident on a diffraction grating. Proper design of the coupler causes the light to be diffracted into the 10 μm wide waveguide with a loss that can be as small as 5dB. An adiabatic taper reduces the width of this waveguide to the typical photonic wire dimensions. The grating coupler allows nanophotonic components to be 'fully integrated', meaning that the access waveguides are also integrated on the chip. In spite of its practical importance for our experiments a detailed analysis of the grating coupler is also beyond the scope of this work. More details can be found in the PhD thesis of Dirk Taillaert [18].

3.3 Fabrication of freestanding structures in SOI

3.3.1 Fabrication process in a nutshell

The fabrication process is shown in a nutshell in Fig. 3.3. In Fig. 3.3a we see the 'naked' nanophotonic wire, which is covered with a resist mask (Fig. 3.3b). The resist mask is then patterned using standard lithography in order to create an underetch window (Fig. 3.3c). Afterwards wet buffered hydrofluoric acid (BHF) is used to remove the underlying SiO_2 selectively

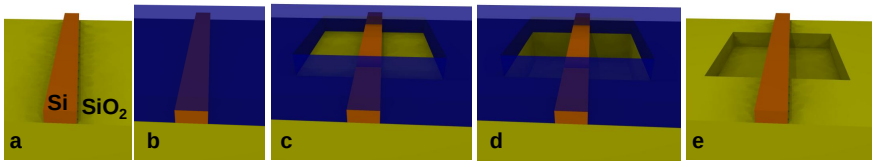

Figure 3.3: **Overview of the underetch process. a**, Single-mode nanophotonic wire. **b**, Spinning on the resist mask. **c**, Lithographically patterned resist mask which defines the underetch window. **d**, Wet buffered hydrofluoric acid (BHF) etch removes the underlying SiO_2 selectively, creating a bridge like structure. **e**, Final result after resist removal and (optional) critical point drying: an underetched single-mode nanophotonic wire.

hence creating a freestanding beam in the top silicon (Fig. 3.3d). The layer which is removed in order to create the freestanding structure is commonly referred to as the sacrificial layer. After the resist is removed we obtain a waveguide with a freestanding underetched part. The final result is shown in Fig. 3.3e. Each of the steps in the process requires some specific issues to be resolved. These will be discussed in more detail in the following subsections.

3.3.2 Choice of the masking material and etchant

The etchant required for the underetching process needs to etch SiO_2 with great selectivity towards silicon, leaving it unharmed. To the best of our knowledge only hydrofluoric acid (HF) satisfies this condition. First water forms silanol groups with the SiO_2 molecules, so water is needed to initiate the reaction:

$$2H_2O + SiO_2 \longrightarrow Si(OH)_4 \tag{3.3}$$

These groups can subsequently be attacked by HF.

$$Si(OH)_4 + 4HF \longrightarrow SiF_4 + 4H_2O \tag{3.4}$$

However the HF etch rate of $SiO_2$is high, unstable and hence it is difficult to control the process. For this reason often buffered hydrofluoric acid (BHF) is used [19]. A common buffered oxide etch solution comprises a 6:1 volume ratio of 40% NH_4F in water to 49% HF in water. The role of NH_4F in the BHF mixture is to act as buffering agent. It stabilizes the pH of the solution and the etch rate. Around room temperature such a solution etches SiO_2 at a rate of 70 to 120 nm min^{-1}. The exact etching speed depends among others on the oxide type, its quality and the ambient conditions.

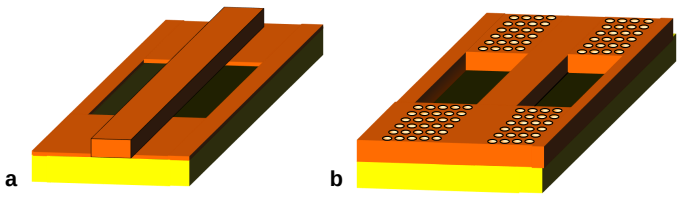

Figure 3.4: **Silicon acting as underetch mask. a**, Shallow etched waveguide terminating the freestanding part. **b**, Photonic crystal waveguide terminating the freestanding part.

Of course also the masking material needs to be resistant to a BHF etch. However this is not the only condition to be fulfilled. BHF also tends to attack the interface between the masking material and the sample. In other words the masking material is left relatively unharmed by HF but it tends to peel off at the edges of the underetch window. Hence the underetched region tends to be larger than defined by the window in the masking material. One of the masking materials which is known not to peel off from silicon or silica when exposed to HF is high quality Low Pressure Chemical Vapor Deposition (LPCVD) silicon nitride [20]. Unfortunately we did not have easy access to this material. Tests with silicon nitride of the lower quality Plasma Enhanced Chemical Vapor Deposition (PECVD) type turned out to be unsuccessful, so finally we decided to focus on reducing the peeling off for a standard resist mask.

One obvious possibility is to apply a spin-on adhesion promoter which enhances the adhesion of resist to the sample, however, water molecules attached to the SiO_2 impede the adhesion of the adhesion promoter to the silica. By consequence we had the best results when applying the adhesion promoter Hexa-Methyl-Disilizane (HMDS) in a vacuum oven. The vacuum and the high temperature first removes the water allowing HMDS (which is brought in the chamber in vapor phase) to attach to the SiO_2 much more effectively. This treatment reduced the peeling off and enabled structures with an underetched portion which exceeds the window length with only a few μm which is perfectly acceptable for this work.

However when aiming for a more precise control of the mechanical properties probably LPCVD nitride would be required for the mask. Alternatively one can think of nanophotonic devices in which the silicon itself acts as the masking material. The part of the photonic wire which has to be underetched can for example be terminated by a shallow etched waveguide (see Fig. 3.4) or a photonic crystal waveguide [21] (see Fig. 3.4). In

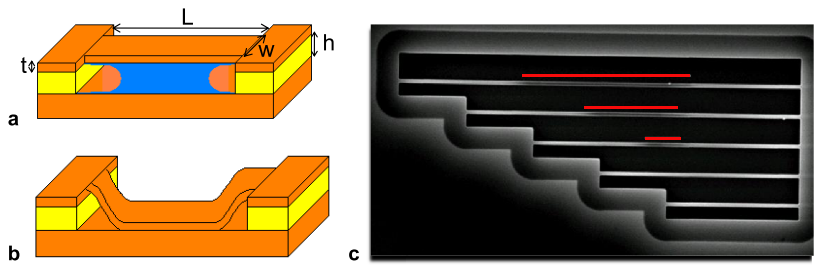

Figure 3.5: **Stiction.** **a**, A liquid drop is formed between the freestanding beam and the substrate. **b**, During the drying cycle the freestanding beam might collapse and remain stuck to the substrate. **c**, SEM picture of a stiction test. The three upper beams are sticking to the substrate, as can be seen from the slight gray decoloring in their centers (and the added red bars, which run in parallel with the sticking zone). The two lower (shorter) beams are truly freestanding.

both cases one has to engineer carefully reflections and losses at the start and end of the freestanding part since the waveguide mode profile might change abruptly there.

3.3.3 Stiction

Stiction is a contraction (or a portmanteau) of 'static friction'. In the context of MEMS it usually refers to the well known phenomenon of adhesion failure. While in the macro-world the main force freestanding structures (such as bridges) have to withstand is gravity, this picture drastically changes at the nanoscale. At this scale gravity is negligible and capillary forces become the main cause of failure. When a wet etchant is used to remove the sacrificial layer unavoidably a drop of liquid forms between the freestanding structure and the substrate (3.5a). Strong attractive capillary forces can develop during the drying cycle causing the freestanding part to collapse and subsequently to stick to the substrate as shown in (3.5b). In fact two conditions need to be fulfilled to end up in the situation of (3.5b). First the freestanding beam needs to be brought in contact with the substrate during the drying cycle. Secondly the adhesive force needs to be sufficiently strong to overcome the repelling spring force of the deflected beam. The latter condition can be modeled by calculating the peel number N_p of the structure. An in depth analysis of this model is beyond the scope of this

thesis. However the peel number can be understood intuitively as the ratio of the increase in the system's potential energy (spring energy $\frac{k_{eff}h^2}{2}$) to the reduction of potential energy (by lowering its surface energy) when the beam is making contact to the substrate. Since systems in general strive to reach the state of lowest potential energy a peeling number $N_p < 1$ means that the beam stays in its pinned state. An approximate expression for the peeling number reads as [22]:

$$N_p = k_{eff}\frac{3h^2}{256wL\gamma_s} \tag{3.5}$$

In this equation k_{eff} is the effective spring constant of the beam, w en L are the width and length of the beam respectively (see also 3.5a). Assuming that these geometric properties are determined by other constraints and are not available as free design parameters we only have the distance h to the substrate and the surface energy γ_s to alter the peeling number. However we will later see that in practice the effects we wish to observe and study in this work require closely spaced freestanding objects (so preferably with as small h as possible). At this point we also mark that stiction is not solely related to the substrate but might as well occur between two in plane objects such as two neighboring freestanding beams. In this case h would denote the gap spacing between the two parallel beams.

Taking the above restrictions into account the only accessible parameter left is γ_s, the surface energy of the material. Also here our freedom seems limited since our preferred material (silicon) has already been determined by various other factors (optical, mechanical and technological). The γ_s for silicon in the $\{1, 0, 0\}$ plane is around $1.36\, Jm^{-2}$ [23]. However in the literature methods to alter the surface chemistry of silicon by application of anti-adhesive coatings can be found [24].
In this work we followed another strategy and tried to avoid the beam ever comes into contact with a neighboring surface. As we have stated previously, the beam might reach the substrate during the drying cycle of the rinsing liquid. This effect can be modeled through the elastocapillary number [22], which reads approximately as:

$$N_e = k_{eff}\frac{4h^2}{15wL\gamma_L\cos(\theta_c)(1+\frac{t}{w})}(1+\frac{108}{245}\frac{h^2}{t^2}) \tag{3.6}$$

Besides the geometrical properties of the beam and the materials used now also the properties of the rinsing liquid come into play since θ_c and γ_L are the contact angle and the surface tension of the liquid. This provides us with an additional degree of freedom. The elastocapillary number also origins from potential energy considerations and $N_e < 1$ means that the beam

will reach the neighboring surface. Simply replacing rinsing water with isopropanol (IPA) increases the elastocapillary number with more than a factor of three since $\gamma_{L,IPA} = 21.7\,mJm^{-2}$ and $\gamma_{L,water} = 75.6\,mJm^{-2}$. In Fig. 3.5c the result of a stiction test we have performed is shown. The structure was dried in water after it was underetched in buffered HF and the full sacrificial layer (1 μm SiO_2) was removed. The beams have a width of 1 μm and a lenght of 20,30,40,50 and 60 μm respectively. Using equation 3.6 we can calculate the elastocapillary numbers for the five beams. A formula for k_{eff} has already been derived (equation 2.17). The biggest problem is θ_c, the contact angle water makes with the silicon surface. According to the literature [25] it can vary from 5° (native oxide, hydrophylic) to 60° (silicon with native oxide removed, hydrophobe). If we set θ_c to 60° and calculate N_e for the five beams that are shown in the picture we find $N_{e,60\mu m}$=0.27, $N_{e,50\mu m}$=0.56, $N_{e,40\mu m}$=1.37, $N_{e,30\mu m}$=4.32 and finally $N_{e,20\mu m}$= 21.9. According to this calculation also the 40μm long beam should not stick to the substrate. As can be seen in Fig. 3.5c this is not the case. It is clear that the elastocapillary number cannot be used as an accurate prediction for cases where it is close to unity. As already mentioned we do not know the exact contact angle and also a severe undercut can be seen in Fig. 3.5c, which might make the beam less stiff. Finally in our experience turbulence in the rinsing water might also negatively influence the chance for the beam not to get stuck to the substrate.
In the next subsection we will discuss a strategy to bring the surface tension to an extremely low value and by consequence to eliminate stiction.

3.3.4 Critical-point-drying

The vapor-liquid critical point of a material denotes the critical pressure p_c and temperature T_c above which distinct liquid and gas phases do not exist anymore. When both the temperature and the pressure are above their critical values (T_c and p_c respectively), then the material is said to be in a *supercritical* state.
Critical-point-drying (CPD) can be understood as traveling around the critical point in the pressure-temperature phase diagram shown in Fig. 3.6. Increasing the pressure and temperature of a material in its liquid phase (point A) results in a supercritical solution (point B). Gradually reducing the pressure at elevated temperature results in a gaseous phase (point C). In fact the liquid has dried without crossing the liquid-gas boundary in the diagram, hence avoiding the detrimental capillary effects described in the previous subsection.

Not all substances have practically achievable critical points. Espe-

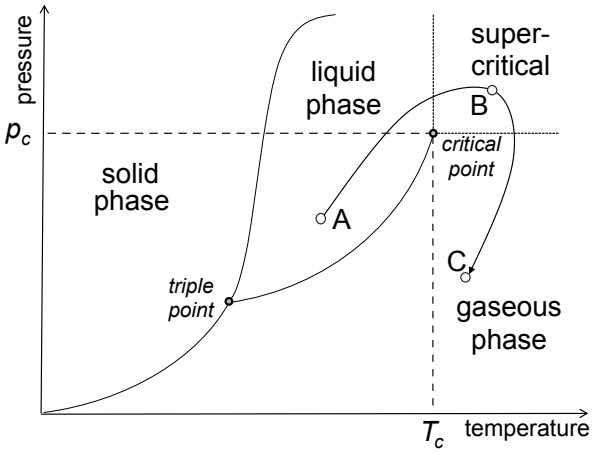

Figure 3.6: Critical-point-drying can be understood as traveling around the critical point (T_c, p_c) in the temperature-pressure phase diagram. The rinsing fluid is brought from its liquid phase (point A) to its supercritical state (point B) by increasing the pressure and temperature sufficiently. Gradually reducing the pressure in point B bring us at point C in the gaseous phase without having crossed the liquid-gas phase boundary.

cially reaching high pressures is not a sinecure. In table 3.2 some potentially interesting substances are given with their critical temperature T_c and pressure p_c [26, 27], listed according to increasing critical pressure. Freon-13 (CFC) at first sight seems the best choice ($T_{c,CFC} = 28.08°C$ and $p_{c,CFC} = 38.1\,atm$), however, it is banned in many countries because of its ozone depletion potential. The most popular substance to perform CPD is CO_2 because its critical pressure ($p_{c,CO_2} = 72.8\,atm$) and temperature ($T_{c,CO_2} = 31.04°C$) are still relatively easy to achieve. It is also less scarce and expensive than xenon ($T_{c,Xe} = 16.6°C$ and $p_{c,Xe} = 57.6\,atm$). Nitrous oxide (N_2O) has similar critical point characteristics to CO_2 but is a strong oxidizer in its supercritical state. Water is clearly out of question: it reaches its critical point at $p_{c,H_2O} = 217.7\,atm$ and ($T_{c,H_20} = 373.946°C$). Moreover it behaves as a powerful oxidizer under these harsh conditions.

In practice Critical-Point-Drying is performed using a specialized tool in which a chamber filled with solvent (typically isopropanol or acetone) is gradually refilled with liquid CO_2 after which the critical point drying cycle can be performed. We have used the Tousimis [28] Critical Point Dryer which was available in imec. With this technique we were able to dry par-

substance	T_c (°C)	p_c (atm)
freon-13 (CFC)	28.8	38.1
xenon	16.6	57.6
CO_2	31.04	72.8
N_2O	36.4	71.5
water	373.946	217.7

Table 3.2: Critical temperature T_c and pressure p_c for some substances with critical points which are practically achievable. The substances are listed according increasing critical pressure. The values were taken from references [26, 27]

allel freestanding beams up to 30 μm with gap spacings of approximately 150 nm without stiction. Such beams would normally have an elastocapillary number of approximately 0.04 and cannot survive an ordinary drying cycle.
We also mention the possibility of using a gaseous etchant. It is indeed possible to use HF in a vaporized state, hence removing directly all stiction related troubles. Given the extremely toxic, corrosive and harmful nature of HF vapors [29] we considered this option to be too risky to implement ourselves. Besides the safety issue also some additional technological problems are encountered with this approach [30]. Critical-point-drying is also a lot more flexible than HF-vapor for it can be used in combination with any possible wet etchant.

Bibliography

[1] J.J. Wortman and R.A. Evans. Young's modulus, shear modulus and Poisson's ratio in silicon and germanium. *Journal of Applied Physics*, 36(1):153–156, 1965.

[2] W.H. Miller. *A Treatise on Crystallography*. Pitt Press, London, 1839.

[3] A. Ballato. Poisson's ratio for tetragonal, hexagonal, and cubic crystals. *IEEE Transactions on ultrasonics ferroelectrics and frequency control*, 43(1):56–62, 1996.

[4] K.E. Petersen. Silicon as a mechanical material. *Proceedings of the IEEE*, 70(5):420–457, 1982.

[5] D. H. Alsem, O. N. Pierron, E. A. Stach, C. L. Muhlstein, and R. O. Ritchie. Mechanisms for fatigue of micron-scale silicon structural films. *Advance engineering materials*, 9(1-2):15–30, 2007.

[6] H. Kahn, R. Ballarini, and A.H. Heuer. Dynamic fatigue of silicon. *Current opinion in solid state & materials science*, 8(1):71–76, 2004.

[7] W.T. Hsu. Reliability of silicon resonator oscillators. In *Proceedings of the 2006 IEEE International Frequency Control Symposium and Exposition, Vols 1 and 2*, pages 389–392, 2006. IEEE International Frequency Control Symposium and Exposition, Miami, FL, JUN 04-07, 2006.

[8] M.E. Levinshtein, S.L Rumyantsev, and M. Shur. *Handbook Series on Semiconductor Parameters: Si, Ge, C (Diamond), GaAs, GaP, GaSb, InAs, InP, InSb*. World Scientific, New York, NY, USA, 1996.

[9] Gabriel M. Rebeiz. *RF MEMS: Theory, Design, and Technology*, chapter Appendix B.

[10] O. Auciello, S. Pacheco, A.V. Sumant, C. Gudeman, S. Sampath, A. Datta, R.W. Carpick, V. P. Adiga, P. Zurcher, Z. Ma, H.-C. Yuan, J.A. Carlisle, B. Kabius, J. Hiller, and S. Srinivasan. Are diamonds a MEMS' best friend? *IEEE Microwave Magazine*, 8(6):61–75, 2007.

[11] Verbist M. and Van Thourhout. D. Focused ion beam etching of thin diamond layers. In *Proceedings of the 2009 Annual Symposium IEEE Photonics Benelux Chapter*, pages 113–116, 2009.

[12] W. Bogaerts. *Nanophotonic Waveguides and Photonic Crystals in Silicon-on-Insulator*. PhD thesis, Ghent University, Ghent, Belgium, 2004.

[13] P. Dumon. *Ultracompact Integrated Optical Filters in Silicon-on-Insulator by Means of Wafer-Scale Technology*. PhD thesis, Ghent University, Ghent, Belgium, 2004.

[14] S.K. Selvaraja. *Wafer scale fabrication technology for silicon photonic integrated circuits*. PhD thesis, Ghent University, Ghent, Belgium, 2010.

[15] W. Bogaerts, R. Baets, P. Dumon, V. Wiaux, S. Beckx, D. Taillaert, B. Luyssaert, J. Van Campenhout, P. Bienstman, and D. Van Thourhout. Nanophotonic waveguides in silicon-on-insulator

fabricated with CMOS technology. *Journal of Lightwave Technology*, 23(1):401–412, 2005.

[16] S.K. Selvaraja, P. Jaenen, W. Bogaerts, D. Van Thourhout, P. Dumon, and R. Baets. Fabrication of Photonic Wire and Crystal Circuits in Silicon-on-Insulator Using 193-nm Optical Lithography. *Journal of Lightwave Technology*, 27(18):4076–4083, 2009.

[17] D. Taillaert, P. Bienstman, and R. Baets. Compact efficient broadband grating coupler for silicon-on-insulator waveguides. *Optics Letters*, 29(23):2749–2751, 2004.

[18] D. Taillaert. *Grating couplers as Interface between Optical Fibres and Nanophotonic Waveguides*. PhD thesis, Ghent University, Ghent, Belgium, 2004.

[19] K.R. Williams, K. Gupta, and M. Wasilik. Etch rates for micromachining processing - Part II. *Journal of Microelectromechanical Systems*, 12(6):761–778, 2003.

[20] C. Iliescu, B.T. Chen, F.E.H. Tay, G.L. Xu, and J.M. Miao. Characterization of deep wet etching of glass - art. no. 60370A. In Chiao, JC and Dzurak, AS and Jagadish, C and Thiel, DV, editor, *Device and Process Technologies for Microelectronics, MEMS, and Photonics IV*, volume 6037 of *Proceedings of the society of photo-optical instrumentation engineers (SPIE)*, page A370, 2006. Conference on Device and Process Technologies for Microelectronics, MEMS and Photonics IV, Brisbane, Australia, 2005.

[21] Mo Li, W. H. P. Pernice, C. Xiong, T. Baehr-Jones, M. Hochberg, and H. X. Tang. Harnessing optical forces in integrated photonic circuits. *Nature*, 456(7221):480–486, 2008.

[22] C.H. Mastrangelo. Suppression of stiction in MEMS. In DeBoer, M.P. and Heuer, A.H. and Jacobs, S.J. and Peeters, E., editor, *Materials science of microelectromechanical sustems (MEMS) devices II*, volume 605 of *Materials Research Society Symposium Proceedings*, pages 105–116, 2000. Symposium MM on Materials Science of Microelectromechanical Systems (MEMS) Devices II held at the 1999 MRS Fall Meeting, BOSTON, MA, 1999.

[23] D.J. Eaglesham, A.E. White, L.C. Feldman, N. Moriya, and D.C. Jacobson. Equilibrium shape of Si. *Physical Review Letters*, 70(11):1643–1646, 1993.

[24] W.R. Ashurst, C. Yau, C. Carraro, C. Lee, G.J. Kluth, R.T. Howe, and R. Maboudian. Alkene based monolayer films as anti-stiction coatings for polysilicon MEMS. *Sensors and actuators A-Physical*, 91(3):239–248, JUL 15 2001. Solid-State Sensors and Actuators Workshop, Hilton Head Isl, South Carolina, 2000.

[25] R. Hull. *Properties of Crystalline silicon*, chapter 5.

[26] Y. Cengel and M. Boles. *Thermodynamics: an engineering approach*, chapter pp. 824.

[27] J. Emsley. *The Elements*. Oxford University Press, 1991.

[28] http://tousimis.com.

[29] http://www.chem.purdue.edu/chemsafety/Equip/hfmsds.pdf.

[30] A. Witvrouw, B. Du Bois, P. De Moor, A. Verbist, C. Van Hoof, H. Bender, and K. Baert. A comparison between wet HF etching and vapor HF etching for sacrificial oxide removal. In Karam, J.M. and Yasaitis, J., editor, *Micromachining and microfabrication process technology VI*, volume 4174 of *Proceedings of the Society of the SPIE)*, pages 130–141, 2000. Conference on Micromachining and Microfabrication Process Technology VI, Santa Clara, CA, 2000.

4

Small displacement sensing

The least movement is of importance to all Nature. The entire ocean is affected by a pebble.
Blaise Pascal

4.1 Introduction to the chapter

IN chapter 1 we already discussed briefly the tendency towards integration and miniaturization of mechanical resonators to the nanoscale (from MEMS to NEMS). In chapter 2 however, we learned that high frequency, low mass nanomechanical resonators come at the price of high stiffness and by consequence smaller displacements for the same applied actuation force. Not surprisingly the need for powerful motion transduction techniques has attracted a lot of attention in the scientific community. Also in the context of this work the detection of small vibrations was of crucial importance. In this chapter we give an overview of the transduction methods in the literature and subsequently we explain the approach developed for nanophotonic structures.

Tiny thermal 'brownian' vibrations will be used to calibrate optically induced forces (see Chapter 5). In the current chapter we will explain the origin of this thermal mechanical motion that is encountered in mechanical oscillators. Then we review shortly the broad spectrum of displacement sensing techniques described in literature, their variety reflecting the diffi-

culty and importance of this field. Following we discuss the general principle behind small displacement detection with nanophotonic waveguides, a novel technique developed and improved during this Ph.D. Finally we show our experimental results concerning small displacement sensing and explain the practical experimental limitations.

4.2 Thermal mechanical noise

4.2.1 The fluctuation-dissipation theorem

The thermal motion of electrically charged particles inside materials gives rise to a fluctuating electromagnetic field. Because fluctuations of charge in materials lead to dissipation via radiation, no object at finite temperature can be in perfect thermal equilibrium in a realistic situation. However in most cases the object can be considered to be close to equilibrium and the non-equilibrium behavior can be described by linear response theory. This is the essence of the *fluctuation-dissipation* theorem [1]: the rate of energy dissipation in a non-equilibrium system can be related to fluctuations that occur spontaneously in an equilibrium system. One of the earliest and best known manifestations of the fluctuation dissipation theorem is the Einstein relation that relates the diffusion constant D (of colloidal particles) to the solvent viscosity η: $D = \frac{k_B T}{6\pi R\eta}$ ($k_B = 1.38 \times 10^{-23} JK^{-1}$ the Boltzmann constant, T the absolute temperature, R the radius of the spherical particle).

When applying the fluctuation-dissipation theorem to the mechanical spring-mass-damper system that we have introduced in chapter 2 we can state that the damping in fact provides a two way path. On one hand it allows energy to leave the system, on the other hand if thermal energy from the environment increases the temperature, then the mechanical oscillator's motion increases intrinsically. We can think of the latter as an additional thermal 'brownian' force which is acting on the oscillator.

4.2.2 Brownian force

Callen and Welton were the first to derive the fluctuation-dissipation theorem in its very general form [2]. Such a rigorous derivation is far beyond the scope of this work. We restrict ourselves to the analysis of a mass-spring-damper system in the high temperature limit ($k_B T \gg hf$, $h = 6.626 \times 10^{-34} Js$ Planck's constant and f the mechanical oscillation frequency) for which the classical equipartition theorem is valid. According to the equipartition theorem the different energy storage modes of a system in thermal equilibrium should contain an average energy of $\frac{k_B T}{2}$.

For the mass-spring-damper system we have two possible energy storage modes, kinetic energy (mass m) and the potential energy (spring constant k) [3].

$$\frac{1}{2}k_BT = \int_0^\infty \frac{1}{2}k < |x| >^2 \mathrm{d}f = \int_0^\infty \frac{1}{2}m < |\dot{x}| >^2 \mathrm{d}f \tag{4.1}$$

The energy integral is taken over the total spectrum. In order to make the dimensions match $x(t)$ and $\dot{x}(t)$ should be interpreted as a displacement and velocity per square root Hertz respectively. In this work we will sometimes use rtHz units ($rtHz = \sqrt{Hz}$). The brackets in equation 4.1 denote a time average.

Starting from the equation for a damped harmonic oscillator (damping factor Γ) in the frequency domain, we can tie the displacement noise ($m\sqrt{Hz^{-1}}$) to a noise force F_b ($N\sqrt{Hz^{-1}}$) (see equations 2.45 and 2.47 in subsection 2.5.3).

$$< x >= \frac{< F_b >}{(k - m\omega^2) + j\omega\Gamma} \tag{4.2}$$

Hence we can calculate the spring potential energy:

$$\frac{k}{2} < |x| >^2 = \frac{k}{2}\frac{< F_b >^2}{(k - m\omega^2)^2 + \omega^2\Gamma^2} \tag{4.3}$$

Substituting the mechanical resonance frequency $\omega_0 = \sqrt{\frac{k}{m}}$ and quality factor $Q = \frac{\omega_0 m}{\Gamma}$ and taking the integral over the entire spectrum we can write:

$$\frac{1}{2}k_BT = \int_0^\infty \frac{1}{2}k < x >^2 \mathrm{d}f = \frac{< F_b >^2}{4\pi\Gamma}\int_0^\infty \frac{Q}{Q^2(1 - \frac{f}{f_0}^2)^2 + \frac{f}{f_0}^2}\mathrm{d}\frac{f}{f_0} \tag{4.4}$$

We have also taken $< F_b >^2$ out of the integral, hence assuming that the noise force does not depend on the frequency (so called *white* noise). If the quality factor is sufficiently high the displacement will indeed take place in a narrow band around the resonance frequency where the noise can be assumed to be white [4]. Evaluation of the integral returns $\frac{\pi}{2}$, so finally equation 4.4 reduces to:

$$< F_b >^2 = 4\Gamma k_BT \tag{4.5}$$

At this time we wish to point out the striking similarity between equation 4.5 and the —to electrical engineers well known— Johnson-Nyquist noise

in resistors. Indeed a resistor with resistance R at an absolute temperature T will exhibit a noise voltage $< V_b > (V\sqrt{Hz^{-1}})$ given by [5]:

$$< V_b >^2 = 4Rk_BT \tag{4.6}$$

We have previously pointed out the mathematical analogy between RLC circuits in electronics and mass-spring-damper systems in mechanics. The analogy we encounter here is stronger than a mere mathematical one since both phenomena (voltage and force noise) origin from vibrating particles in the material lattice. In fact the Johnson-Nyquist voltage noise can be understood as scattering from electrons due to lattice vibrations and by consequence it is also intrinsically mechanical in nature [4].

4.2.3 Calibration procedure

In the context of this work the thermal mechanical noise is important for calibration of tiny forces. First we rewrite equation 4.5 by introducing the Q-factor again:

$$< F_b >= \sqrt{4\frac{\omega_0 m}{Q}k_BT} \tag{4.7}$$

In a measurement band width BW this noise force F_b (unit $N\sqrt{Hz^{-1}}$) results in an effective force F_{eff} (unit N):

$$F_{eff} = \sqrt{4\frac{\omega_0 m}{Q}k_BT}\sqrt{BW} \tag{4.8}$$

Looking at this equation we note that the parameters k_B and BW in this equation are known a priori. k_B is the (well known) Boltzmann constant and the measurement bandwidth we can set ourselves during the experiment. The resonance frequency ω_0 and the quality factor Q of the mechanical oscillator can be obtained directly through measurement. However it is very hard to measure the oscillator mass m and the exact oscillator temperature T directly in an experiment. These parameters cause the largest uncertainties in our calibration procedure for they must be estimated. For the temperature we assume that the optical power levels in the experiments are not sufficient to heat up the oscillator and its direct environment to very high temperatures and we take $T \approx 300\,K$. The oscillator mass can be approximated by estimating the dimensions of the oscillator through SEM and using the well known mass density of silicon ($2329\,kg\,m^{-3}$).

However as we have already discussed in subsection 2.5.2 this mass should be weighted with an additional factor (see table 2.3) that typically varies between 0.397 (ground mode fixed-fixed beam) and 0.5 (ground

mode hinged-hinged beam). Once we have estimated m_{eff} and T we can easily calculate the effective 'brownian' force (using equation 4.8) and use it for calibration. The application of mechanical brownian noise for calibration purposes of mechanical oscillators has been described and assessed earlier in literature in the context of atomic force microscopy (AFM) experiments [6].

We also mention that different units can be used to display the recorded vibration signals. The electrical spectrum analyzer (ESA) in combination with an optical detector in fact always measures the optical power (units dBm) in a certain bandwidth so for a brownian signal we can plot the values in dBm (raw data) or $dBm\sqrt{Hz^{-1}}$ (scaled with measurement bandwidth). The latter is also referred to as the power spectral density (PSD).

The measured PSD is in fact a consequence of the oscillator's displacement spectral density, expressed in $nm\sqrt{Hz^{-1}}$ (DSD). The oscillator's DSD is given by $\frac{<F_b>}{k}\chi_{MECH}(\omega)$ ($\chi_{MECH}(\omega)$ is the mechanical susceptibility with parameters Q and ω_0, see equation 2.47). Fitting a Lorentzian to the PSD allows us to extract Q and ω_0. Through estimation of the parameters that cannot be fitted such as temperature and effective mass we can finally calculate $< F_b >$, k and $\chi_{MECH}(\omega)$ and by consequence we know all parameters needed to calibrate the experimental data. Thermal brownian forces and displacements are inherently related to measurement bandwidth and are expressed in units of $dBm\,\sqrt{Hz^{-1}}$, $N\,\sqrt{Hz^{-1}}$ and $nm\,\sqrt{Hz^{-1}}$. However if we use an external harmonic force excitation (for example from a signal generator) we can think of the excitation as a Dirac function in the frequency domain and signals are displayed using dBm, N or nm. The calibration procedure is summarized in Fig. 4.1.

Finally in order to get a feeling for the order of magnitude of the brownian force let us consider a numerical example with values that are typical for our work. A silicon beam of $25\mu m$ with single-mode waveguide dimensions ($220\,nm$ height $\times\,440\,nm$ width) and a Q of 2000 would exhibit an in-plane noise force of $0.87\,fN\sqrt{Hz^{-1}}$ and an effective force of $2.75\,fN$ in a bandwidth of $10\,Hz$ at a temperature of 300 K. This results in a peak noise displacement of $0.48\,pm\sqrt{Hz^{-1}}$ ($1.5\,pm$ in a $10\,Hz$ BW). To put these numbers in perspective it is useful to know that the lattice constant of silicon is approximately $0.5\,nm$. It is clear that in order to detect such small vibrations, sensitive transducer methods are required.

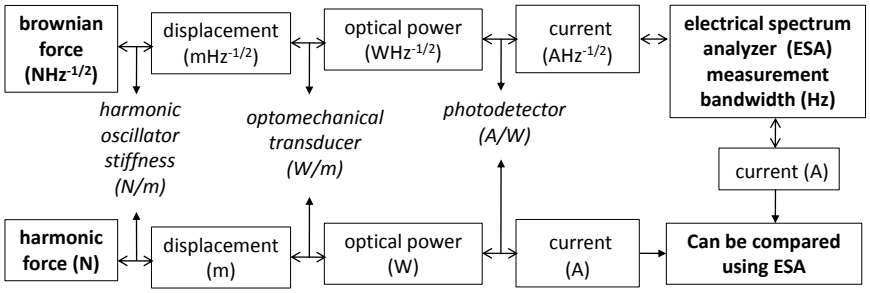

Figure 4.1: **Calibration procedure.** The (to calibrated) harmonic force is transformed into a harmonic current. Also the (easily calculated) brownian force can be linked to a current (dependent on the measurement bandwidth of the electrical spectrum analyzer). Comparing the magnitude of the generated currents hence allows comparison of the harmonic force to the (known) brownian force.

4.3 State-of-the-art motion transducers

4.3.1 Capacitive detection

In a capacitive transduction scheme [7] (Fig. 4.2a) an electrode close to the device under test is required. This way the mechanical oscillator acts as a plate of a capacitor. When a DC voltage is applied an amount of charge Q_c is trapped on the plates of the capacitor ($Q_c = C(x)V_{DC}$). The capacitance C strongly depends on the separation g between the external electrode and the oscillator (in a parallel plate capacitor model $C \propto g^{-1}$). By consequence Q_c also depends on the position coordinate x of the oscillator, so whenever the oscillator moves a current $i_{cap}(t)$ must be generated to alter Q_c:

$$i_{cap}(t) = V_{DC}\frac{\partial C}{\partial x}\frac{\partial x}{\partial t} \tag{4.9}$$

This current is intrinsically AC and can be amplified and detected. It is worthwhile noting that capacitive transduction inherently enables capacitive actuation. A voltage can be used to generate a time dependent Coulomb force:

$$\begin{aligned} F_{cap}(t) =& \frac{1}{2}\left(V_{DC} + V_{AC}\cos(\omega t)\right)^2\frac{\partial C}{\partial x} \\ =& \left(\frac{V_{DC}^2}{2} + \frac{V_{AC}^2}{4}\right)\frac{\partial C}{\partial x} + V_{AC}V_{DC}\cos(\omega t)\frac{\partial C}{\partial x} + \frac{V_{AC}^2}{4}\cos(2\omega t)\frac{\partial C}{\partial x} \end{aligned} \tag{4.10}$$

The above formula shows that the combination of an AC and DC voltage generates a force component at frequencies ω, 2ω and a DC force. Capacitive actuation has also been explored in this Ph.D. for the actuation of grating light valves [8], [9] and parallel waveguide structures [10] but it is not within the main focus of this work.

Capacitive detection is widely applied in the realm of MEMS, however, it is inherently incompatible with down scaling the device size to the nano-scale (NEMS) for the capacitance of a parallel plate capacitor scales with l_{sc}^2. We have again introduced the uniform scale factor l_{sc} that all dimensions (width, height, length) are proportional to. As can be seen in equation 4.9 a small capacitance reduces the generated current $\frac{\partial C}{\partial x} \approx \frac{-C}{g}$. Of course reducing the gap size could be considered to compensate for the reduced capacitance. However this approach might raise fabrication issues and increases the (usually unwanted) non-linear sensing response (see section 2.7 on non-linear mechanics). In addition electrical pull-in might occur for smaller gaps [7]. Pull-in also explains why simply increasing the bias voltage is not an option here. Moreover a high voltage over a small gap might also cause electrical breakdown and in addition high voltages are just not always easy to achieve on a chip. Finally we note that capacitive actuation for NEMS also suffers from the typical problems that occur with high frequency electronics (transmission line effects, reflections, RC-time constants which work as low-pass filter for high frequencies). We conclude that capacitive detection —in spite of its popularity in the MEMS community— poses too much troubles for effective miniaturization of devices.

4.3.2 Magnetomotive detection

A possible answer to the scaling limits we run into with capacitive detection is a magnetomotive detection scheme (Fig. 4.2b) [11–13]. In this scheme a large magnetic field is applied perpendicular to the plane of motion. The motion of the oscillator will generate an electromotive force (measured in volts):

$$v_{EMF}(t) = \psi LB\frac{\partial x}{\partial t} \tag{4.11}$$

ψ is a proportionality constant close to unity (depending on the mode shape) while L is the length of the beam. Similar to the capacitive case detection and actuation can be reversed and there is also a possibility to generate a magnetomotive actuation force through the well known Lorentz force. A drive current $i_{drive}(t)$ and a magnetic induction B will generate following force:

$$F_{Lorentz}(t) = \psi LBi_{drive}(t) \tag{4.12}$$

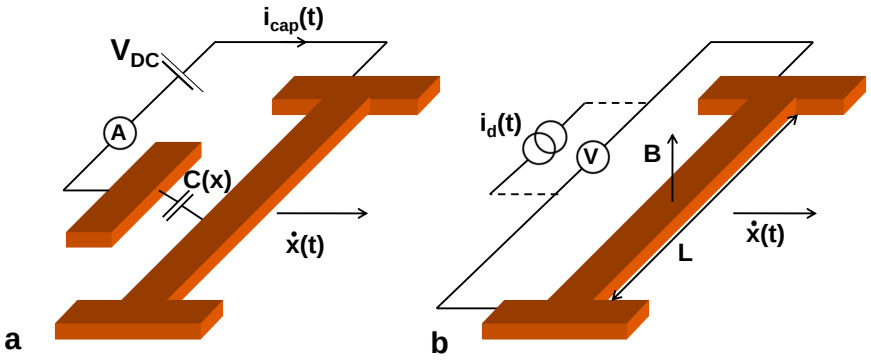

Figure 4.2: **Capacitive and magnetomotive motion transduction. a**, In a capacitive detection scheme the mechanical oscillator acts as a plate of a capacitor. A neighboring electrode provides the second plate and a DC voltage V_{DC} is applied over this capacitor. The capacitance C (and hence the charge $Q_c = C(x)V_{DC}$ stored in the capacitor) depends on the oscillator's position coordinate x. In case the oscillator is moving ($\dot{x}(t) \neq 0$) a current $i_{cap}(t)$ (which can be monitored) will be generated to alter the charge on the capacitor plates. **b**, In a magnetomotive detection scheme a DC magnetic field (with magnetic induction B) is applied perpendicular to the plane of motion. A detectable electromotive force (SI unit volt) will be generated when the oscillator moves.

The biggest issue in this scheme is the requirement for a large magnetic field (preferably on the orders of several Tesla). The technique also requires a conducting material (on top of the oscillator or the oscillator material itself should be conductive) which limits the applicable materials.

4.3.3 Other non-optical techniques

Piezo-electric motion transduction uses piezoelectric materials. In these materials an electric field is generated when strained. Again the process can be reversed and both detection and actuation can be achieved. Piezo-electric sensing is in many ways a promising path since it solves a lot of issues arising with magnetomotive and capacitive actuation and in addition great sensitivity can be achieved [14–16]. For example a recently demonstrated quantum ground state cooling experiment featured piezo-electric displacement sensing [17]. On the drawback side not all materials show a piezoelectric effect (silicon for example does not) such that often a stack of different materials might be needed, hence complicating fabrication. Also piezoelectric sensing still requires electrical paths limiting the achievable bandwidth.

Another more exotic means of sensing is electron tunneling. Very sensitive motion transduction has been reported using this effect [18, 19]. However the method is inherently very non-linear and it is difficult to achieve high bandwidths. In the following (sub)sections we will discuss optical transducer methods which lift the intrinsic bandwidth limitations of electrical signals.

4.3.4 Free space optics

Free space optics small displacement sensing is in general performed through some form of interferometry [20–22]. While in Michelson interferometry the light that interacts with the device under test interferes with a reference beam, in a Fabry-Pérot (FP) interferometer interference inside a cavity is used. Typically one of the two mirrors of the cavity is fixed while the other is allowed to move. Displacement of the movable mirror then changes the cavity's reflection (and transmission). In Fig. 4.3a a typical example is shown: the micromirror on top of the cantilever allows to track the cantilever's displacement when the mirror is placed in a cavity.

However our main focus is on integrated structures. In Fig. 4.3b a laser beam is focused on a suspended beam. The beam itself and the underlying substrate also form an FP-cavity. An experimental set-up to characterize suspended structures with this FP method was built during the Ph.D. of

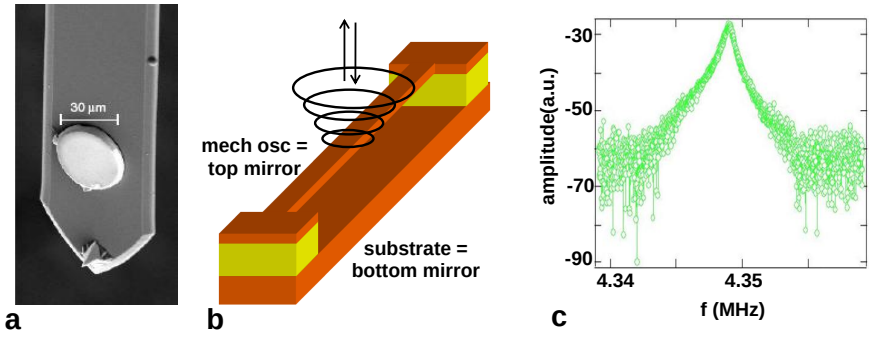

Figure 4.3: **Free space optics displacement sensing with FP cavities. a**, A micromirror which is placed at the top of a cantilever. Figure reproduced with permission from ref [23]. ©2006 NPG **b**, Suspended beam above a substrate forming an FP cavity for the incident light. **c**, Experimental response of a suspended beam, actuated through a piezoelectric shaker [24] and characterized through FP interferometry

Iwijn De Vlaminck [24]. Fig. 4.3c shows an experimental result that was obtained with this set-up. In fact we see the ground mode's resonance peak of the shortest beam of our underetch test structures (these were discussed in the previous chapter, see also Fig. 3.5 and subsection 3.3.3). Another interesting free space optics technique (although attempts towards integration are undertaken [25]) worth mentioning is laser doppler vibrometry [26]. The instantaneous velocity of the device under test is imprinted onto the optical signal as a Doppler frequency shift $\Delta f(t) = \frac{2}{\lambda}\dot{x}(t)$. Analysis of the beat signal created by interference of the Doppler shifted signal with a reference signal allows direct registration in the time domain of the beam's velocity.

Both methods in principle only allow out-of-plane vibrations to be detected and require accurate alignment. The latter issue is increasingly important when the lateral dimension of the beam shrinks to subwavelength size for the minimum achievable spot size is limited by diffraction (minimum spot radius $\propto \frac{\lambda}{NA}$ with NA the numerical aperture of the focusing lens). If the spot size exceeds the beam dimensions then light will be scattered strongly and less reflected light can be collected. The important limitations of the free space optics methods can be overcome by the integrated optical motion transduction method that we will discuss in the following sections.

We also wish to stress that the above list of techniques is by far not

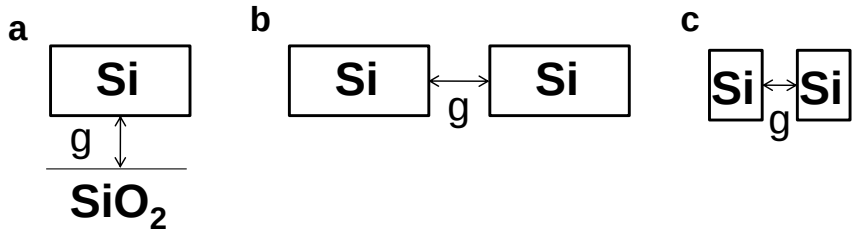

Figure 4.4: **Cross-section of several waveguide types with a gap parameter g. a**, Single-mode silicon waveguide. In this case g is the gap towards the SiO_2 substrate. **b**, Two parallel waveguides with spacing g in between. **c**, Slotted waveguide. g is the width of the slot.

complete. It rather provides a quick overview of some different techniques, much more information can be found in literature. For example the review paper by Ekinci on motion transduction in NEMS is recommended [27].

4.4 Optical transduction principle

In the most general sense an optical mechanical transducer imprints the displacement Δg of a certain object upon an optical probe signal. In case of an integrated nanophotonic waveguide transducer, the waveguide or a part of the waveguide needs to move relatively to another object in order to change the effective index $n_{eff}(g)$ (indices) of the waveguide mode(s). In principle $n_{eff}(g)$ can be a complex quantity but in the context of this work we will only consider real $n_{eff}(g)$. We will ignore the refractive index change that is caused by the elasto-optic effect since this effect is ignorable for most practical situations and more in particular the experiments carried out in this thesis.

Some configurations that were investigated in this work are shown in Fig. 4.4. The parameter g can for example refer to the gap between the waveguide and the substrate (Fig. 4.4a), the separation in between two parallel waveguides (Fig. 4.4b) or the slot width of a slotted waveguide (Fig. 4.4c).

When the effective index of a waveguide modes change over a certain length L a phase difference will be accumulated over the propagation length, so in fact the gap change Δg can be connected to a phase shift:

$$\Delta\phi = \Delta n_{eff}\frac{2\pi}{\lambda}L = \Delta g\frac{\mathrm{d}n_{eff}}{\mathrm{d}g}\frac{2\pi}{\lambda}L \tag{4.13}$$

We assumed here that $n_{eff}(g+\Delta g) = n_{eff} + \Delta g \frac{\mathrm{d}n_{eff}}{\mathrm{d}g}$ which is a acceptable assumption for sufficiently small Δg.

However in order to be detectable with an optical detector the displacement should be imprinted onto the optical carrier as an optical power change rather than a change in phase. An interferometer or optical resonator can be used for this purpose. Typically these components show a (phase dependent) transmission (transmission defined as the optical output power normalized for the optical input power $T_x(\phi[g]) = P_{out}/P_{in}$). Hence the derivative of the transmission for the gap g can be considered an important figure of merit to evaluate nanophotonic transducer performance. In the sense of the chain rule the *transduction coefficient* can be read as:

$$\frac{\mathrm{d}T_x}{\mathrm{d}g} = \frac{\mathrm{d}T_x}{\mathrm{d}\phi}\frac{\mathrm{d}\phi}{\mathrm{d}g} \tag{4.14}$$

The first factor on the right hand side in equation 4.14 is influenced considerably by the chosen configuration (interferometer or resonator). We will elaborate on this parameter in section 4.5 and define $\frac{\mathrm{d}T_x}{\mathrm{d}\phi}$ as the phase sensitivity. The second factor is rather determined by the chosen waveguide type (Fig. 4.4) and its exact design parameters (see section 4.6).

4.5 Phase sensitivity

In this section we discuss the phase sensitivity of a (Mach-Zehnder) interferometer, an optical resonator (Fabry-Pérot type or ring resonator) and a directional coupler. Essentially we are looking for a configuration that exhibits an as large as possible output power shift for a small phase perturbation $\Delta\phi$.

4.5.1 Mach-Zehnder interferometer

Let us consider the Mach-Zehnder interferometer (MZI) depicted in Fig. 4.5. The two Multi-Mode Interferometers (MMI) act as 3 dB coupler/combiner in this scheme. The upper arm of the interferometer is ΔL longer which allows the light propagating through the upper arm to accumulate a phase delay $\phi = \frac{2\pi n_{eff}}{\lambda}\Delta L$ resulting in the well-known expression for transmission:

$$T_{x,MZI} = T_{x,min} + (T_{x,max} - T_{x,min})\cos\left(\frac{\phi}{2}\right)^2 \tag{4.15}$$

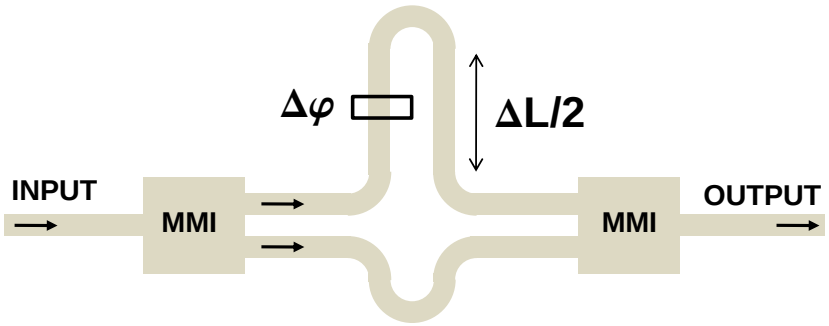

Figure 4.5: An integrated Mach-Zehnder interferometer, the first (left) multi-mode interferometer (MMI) acts as a 3dB power splitter to the INPUT power. The light propagating in the upper (longer) arm accumulates a phase delay $\phi = \frac{2\pi n_{eff}}{\lambda}\Delta L$. Sensing of an additional phase shift $\Delta\phi$ is possible since the OUTPUT power depends on the phase shift between the two arms when combining both arms in the second (right) MMI.

In case of a lossless system and perfect MMIs the mininum transmission $T_{x,min}$ will be zero. If a small phase perturbation $\Delta\phi$ occurs in one of the arms, then the phase sensitivity of the MZI reads as:

$$\frac{\mathrm{d}T_{x,MZI}}{\mathrm{d}\phi} = \frac{(T_{x,min} - T_{x,max})}{2}\sin(\phi) \tag{4.16}$$

The absolute value of 4.16 peaks for $\phi = \frac{\pi}{2} + k\pi$ (k an integer number) with a maximum value of $\frac{1-T_{x,min}}{2}$. If the second MMI receives equal optical input powers at both its inputs than the extinction will be large and $T_{x,min} \ll 1$, then $\frac{\mathrm{d}T_{x,MZI}}{\mathrm{d}\phi}|_{MAX} \approx \frac{1}{2}$.

4.5.2 Directional coupler

Fig. 4.6 shows two closely spaced parallel single-mode waveguides with S-shaped access bends. In case a light carrying single-mode waveguide is placed sufficiently close to another single-mode waveguide, light can be coupled from one waveguide to the other. Sufficiently close in this case means that the waveguide modes should experience each other's evanescent field. The presence of the second waveguide can then be considered as a perturbation of the waveguide mode in the first waveguide and the light coupling phenomenon can be described by simple perturbation theory. An in depth analysis of the perturbation theory for optical waveguide

coupling is beyond the scope of this work, we refer the reader to [28], however we restrict ourselves to an interesting conclusion that follows from this theory. In case all power is initially present in one waveguide, then the other waveguide must be identical to enable full coupling of the light to the other waveguide. So much the more the waveguides differ, the lesser is the amount of light that is coupled back-and-forth between the waveguides.
However in this work we will consider the two parallel waveguides as being one bimodal waveguide in order describe the optical properties of the parallel waveguides through a more elegant formalism. From this point of view the power coupling effect between the waveguides can be understood as the interference of the two different 'supermodes' that are supported by this bimodal waveguide.
In fact in this manner we can even think of this directional coupler as an interferometer. If the directional coupler is excited through only one of its input ports, then the supermodes (with different effective indices n^+ and n^-) are excited with equal strength. The two modes will build up a phase shift

$$\phi = \frac{2\pi(n^+ - n^-)}{\lambda} L \tag{4.17}$$

while propagating to the coupling section with length L. With this definition of ϕ the output power found in the 'bar' waveguide can also be described using equation 4.15 (and $1 - T_x(\phi)$ for the 'cross' waveguide). In the ideal case of identical, single-mode and lossless waveguides $T_{x,min}$ is zero (so all power is coupled to the other waveguide):

$$T_{x,bar} = \frac{1}{2} + \frac{\cos(\phi)}{2} \tag{4.18}$$

Since the sum of the optical power in the cross and bar waveguide must be one we also have:

$$T_{x,cross} = \frac{1}{2} - \frac{\cos(\phi)}{2} \tag{4.19}$$

For example if the length L of the directional coupler is zero, then $\phi = 0$. Consequently we find $T_{x,bar} = 1$ and $T_{x,cross} = 0$, in this case no coupling has occurred. In the special case where the coupler has length

$$L_{coupling} = \frac{\lambda}{2(n^+ - n^-)} \tag{4.20}$$

the light has fully coupled from the bar to the cross waveguide. $L_{coupling}$ is often referred to as the coupling length of the directional coupler.

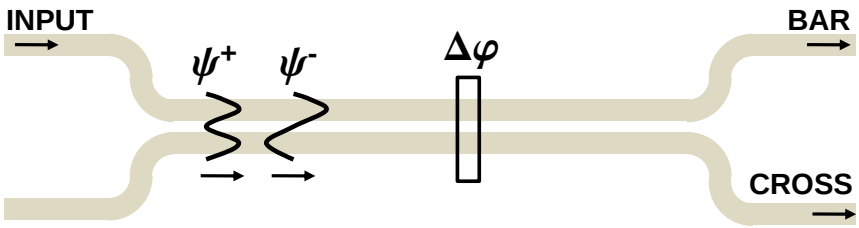

Figure 4.6: Closely spaced parallel waveguides (=coupling section) with S-shaped access bends. If this directional coupler is excited through only one of its input ports (INPUT) then a symmetric supermode ψ^+ and an anti-symmetric supermode ψ^- are excited in the coupling section. These supermodes build up a phase shift $\phi = \frac{2\pi(n^+ - n^-)}{\lambda} L$ over the length of the coupling section and the input power is divided over the BAR and CROSS port depending on this shift. An additional phase shift $\Delta\phi$ between the supermodes in the coupling section will result in a different power distribution at the outputs.

Also the phase sensitivity will be similar to the interferometer case (formula 4.16):

$$\frac{\mathrm{d}T_{x,bar}}{\mathrm{d}\phi} = -\frac{\sin(\phi)}{2} \tag{4.21}$$

From equations 4.18 and 4.21 we conclude that the directional coupler is the most sensitive when it acts as a 3 dB splitter ($T_{x,bar} = \frac{1}{2}$ for $\phi = \frac{\pi}{2} + k\pi$) and the output power is equally divided over the two output arms.

4.5.3 Ring resonators

An optical resonator uses optical feedback. A ring resonator lets a traveling wave interfere with itself. As depicted in 4.7 coupling the ring resonator to two waveguides (add-drop configuration) leads to a transmission spectrum from *input* to the *through* and *drop* port. The former with sharp Lorentzian-like dips, the latter with peaks. If only one access waveguide is present we have an all-pass configuration which shows a unity transmission for a lossless resonator. In practice the device will not be lossless and dips will appear in the *all-pass* output spectrum which can be used for displacement sensing.

Let κ be the amplitude coupling between the access waveguide and the ring resonator with $\tau = \sqrt{1-\kappa^2}$ for a lossless coupler and $n_{eff} = \Re(n_{eff}) + j\Im(n_{eff})$ the complex effective index of the traveling wave in

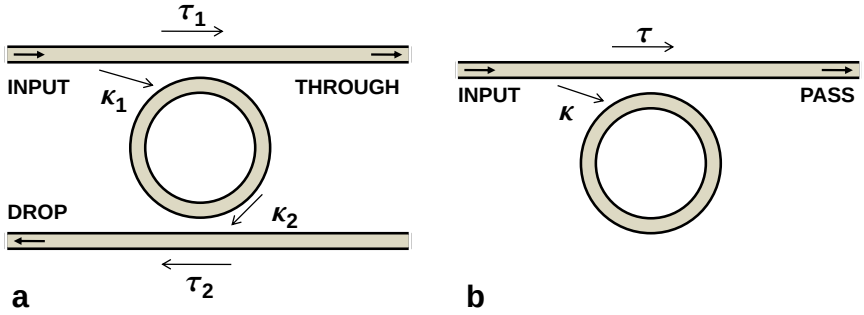

Figure 4.7: **Ring resonators. a**, Add-drop configuration with two access waveguides (coupling coefficients κ_i). **b**, All-pass configuration with only one access waveguide (coupling coefficient κ).

the ring resonator. Let then $A = \exp(-\alpha L) = \exp(-\frac{2\pi}{\lambda}\Im(n_{eff})L)$ be the intrinsic amplitude transmission (excluding coupling losses to the access waveguide) of half a round trip L around the ring with the amplitude extinction coefficient α (in m^{-1}). Let $\phi = 2\frac{2\pi}{\lambda}\Re(n_{eff})L$ be the total phase accumulated over one ring round trip. The equations for the transmission of an all-pass ring can be obtained in terms of only ϕ, A and τ [29]:

$$T_{x,ap} = \frac{T_{x,min} + F\sin\frac{\phi}{2}^2}{1 + F\sin\frac{\phi}{2}^2} \tag{4.22}$$

$$T_{x,min} = \frac{(\tau - A^2)^2}{(1-\tau A^2)^2} \tag{4.23}$$

$$F = \frac{4\tau A^2}{(1-\tau A^2)^2} \tag{4.24}$$

The F parameter can be directly linked to the finesse of the ring resonator, defined as the ratio of the free spectral range (FSR) and the full width at half maximum (FWHM) bandwidth $\delta\lambda$ of the peaks (an all-pass ring only has a transmission spectrum $T_{x,ap}$ with dips, so one should consider $1 - T_{x,ap}$) in that case):

$$\mathscr{F} = \frac{FSR}{\delta\lambda} = \frac{\pi}{2}\sqrt{F}. \tag{4.25}$$

A drawing of an all-pass spectrum with the relevant parameters indicated is shown in Fig. 4.8.

The derivative of 4.22 for ϕ returns the phase sensitivity:

$$\frac{\mathrm{d}T_{x,ap}}{\mathrm{d}\phi} = \frac{(T_{x,min}-1)\sin(\frac{\phi}{2})\cos(\frac{\phi}{2})}{(1+F\sin(\frac{\phi}{2})^2)^2} \tag{4.26}$$

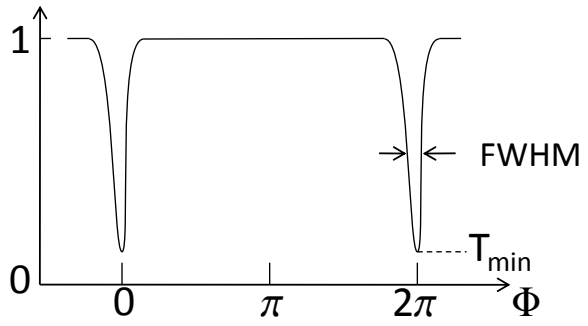

Figure 4.8: All-pass spectrum with some relevant parameters indicated in the drawing.

We are interested in both minima and maxima of equation 4.26 for these extrema both yield maximum $|\frac{\mathrm{d}T_{x,ap}}{\mathrm{d}\phi}|$. By taking the second derivative of 4.22 and looking for ϕ that make this derivative zero we find that such ϕ must satisfy $(2-F)\cos(\frac{\phi_{max,sens}}{2}^2) - 1 - F + 2F\cos(\frac{\phi_{max,sens}}{2})^4 = 0$ yielding (ignoring non-physical solutions):

$$\cos(\frac{\phi_{max,sens}}{2})^2 = \frac{-2+F+\sqrt{4+4F+9F^2}}{4F} \tag{4.27}$$

We note that for higher F $\cos(\frac{\phi_{max,sens}}{2})^2$ converges to 1 and $\phi_{max,sens}$ to 0, meaning that the optimal phase for sensing moves closer to resonance (see Fig. 4.9).

Substituting 4.27 in 4.26 we find a rather cumbersome and inaccessible formula for the maximum achievable phase sensitivity:

$$\begin{aligned}\frac{\mathrm{d}T_{x,ap}}{\mathrm{d}\phi}_{max,sens} &= (1-T_{x,min}) \\ &\frac{4\sqrt{(3F+2-\sqrt{4+4F+9F^2})(F-2+\sqrt{4+4F+9F^2})}}{(3F+6-\sqrt{4+4F+9F^2})^2}\end{aligned} \tag{4.28}$$

Much more physical insight can be achieved if we calculate the limit for high F values:

$$\begin{aligned}\frac{\mathrm{d}T_{x,ap}}{\mathrm{d}\phi}_{max,sens} &\approx \frac{3\sqrt{3}}{16}(1-T_{x,min})\sqrt{F} = \frac{3\sqrt{3}}{8\pi}(1-T_{x,min})\mathscr{F} \\ &\approx 0.207(1-T_{x,min})\mathscr{F}\end{aligned} \tag{4.29}$$

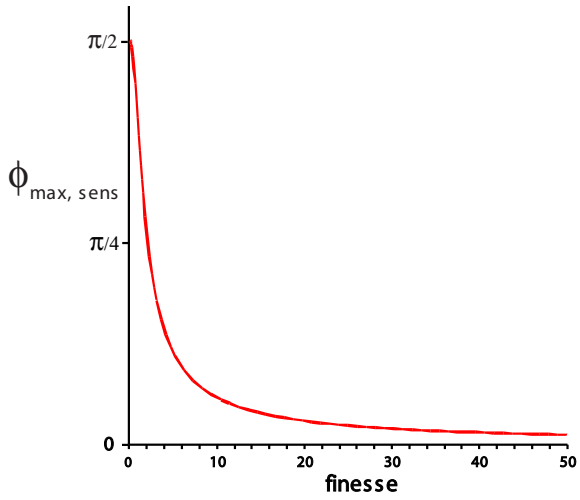

Figure 4.9: The phase $\phi_{max,sens}$ yielding the highest phase sensitivity in function of finesse $\mathscr{F}$. We see that in the high finesse limit, the optimum sensing point moves to resonance ($\phi = 0$).

and for the phase:

$$\sin(\frac{\phi_{max,sens}}{2}) \approx \pm\frac{1}{\sqrt{3F}} \tag{4.30}$$

We conclude that the phase sensitivity scales linearly with finesse. It is interesting to compare 4.29 and 4.16, we see that the feedback provided by an optical resonator becomes valuable in comparison to an interferometer for a resonator with $\mathscr{F} > 2.5$.

However $\mathscr{F}$ and $T_{x,min}$ are not directly controllable as design parameters. Looking at equations 4.23, 4.24 and 4.25 we can express 4.29 in function of A^2 and τ. The A^2 parameter is determined by the losses in the ring resonator and should be as close to one (=low losses) as possible to achieve a high finesse. Its effective value is limited by technology (bending losses, scattering losses due to sidewall roughness, etc.). In silicon also non-linear loss mechanisms like two-photon-absorption (TPA) and free-carrier absorption (FCA) come into play at higher light intensities and result in a power dependent loss [30]. The τ parameter however is determined by the coupling between the access waveguide and the ring resonator and can in principle be chosen freely by varying the distance between resonator and the waveguide. τ can also be reduced by adding a straight part in the ring resonator (racetrack configuration) that increases the interaction

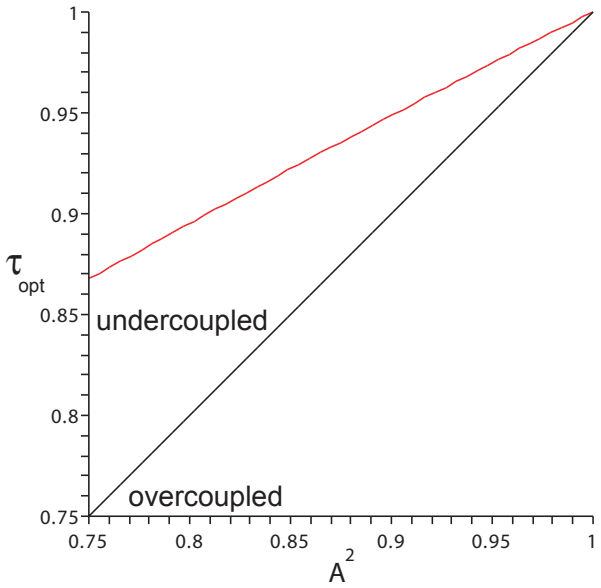

Figure 4.10: The full (red) line indicates which coupling parameter τ yields the best sensitivity for a given (half) round trip ring loss A^2. The black line indicates the critically coupled ($A^2 = \tau$) rings. Above (beneath) this line the ring resonator is undercoupled (overcoupled).

length between access waveguide and resonator and hence the coupling between both. Given the easy access to this parameter it makes sense to calculate which τ should be chosen for a given A^2 to have an optimum performance. For a lossy ring we always find the optimum performance in the undercoupled regime ($\tau > A^2$, see Fig. 4.10). This is not very surprising since the coupling in fact also is a loss factor for the resonator (loaded vs. unloaded resonator). A lower coupling (higher τ) will increase the finesse, however, if the coupling is too small the extinction of the dip disappears (factor $1 - T_{x,min}$ in 4.29) so there must be an optimum coupling value in the undercoupled regime. Substituting this optimum value in 4.28 allows us to calculate the best possible phase sensitivity for a given ring round trip loss. We can also repeat the above analysis for the add-drop configuration with two access waveguides and calculate the maximum phase sensitivity for the *through* and *drop* port.

The result is plotted (together with the result for the all-pass configuration) in 4.11. We learn that the all-pass is superior over the add-drop configuration. We also conclude from this section that losses in the resonator are detrimental for good performance. By consequence high finesse

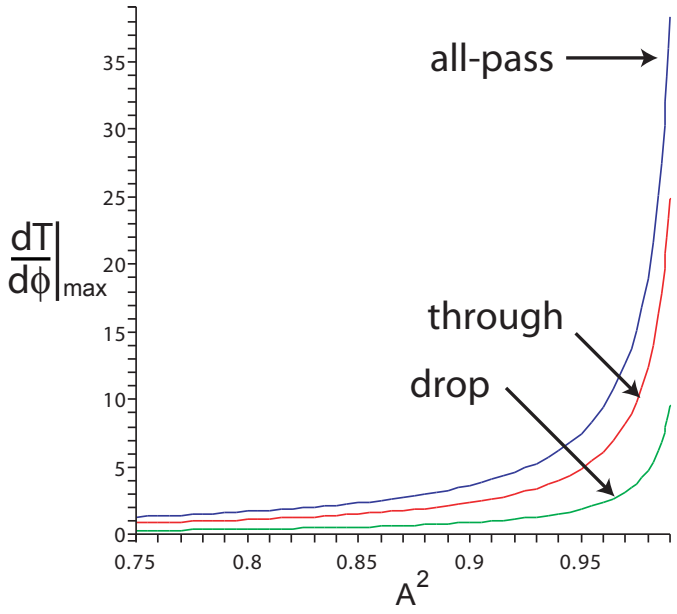

Figure 4.11: Maximum achievable phase sensitivity for different configurations: all-pass (blue), through (red), drop (green). We see that the all-pass configuration is superior.

resonators rather than high Q resonators (that might also be achieved by simply taking a long resonator length L, $Q = \frac{2n_g L}{\lambda}\mathscr{F}$) are preferred.

The above analysis is also applicable to Fabry-Pérot (FP) resonators when simply interpreting the coupling parameter τ as a mirror reflectivity. Half a ring round-trip would correspond to the FP cavity length and the *through* and *drop* spectrum could be interpreted as the reflection and transmission spectrum of the FP resonator respectively. In this case the all-pass configuration is the analogue of the Gires-Tournois etalon with one totally reflecting mirror.

4.6 Displacement to phase transduction

In the previous section we have investigated how a given phase shift $\Delta\phi$ can be detected with the highest sensitivity. In this section we discuss how a given displacement Δg can be translated into an as large as possible $\Delta\phi$. For this purpose we investigate the substrate-waveguide, parallel waveguide and slotted waveguide configurations.

4.6.1 Substrate-waveguide

Probably the simplest concept to translate displacement into a phase change is a waveguide suspended above a substrate. The effective indices n_{eff} of the propagating waveguide modes depend on the separation between the waveguide and the substrate so a displacement Δg induces a phase shift $\Delta\phi = \frac{2\pi L}{\lambda}\frac{\mathrm{d}n_{eff}}{\mathrm{d}g}(g)\Delta g$. In fact the parameter $\frac{\mathrm{d}n_{eff}}{\mathrm{d}g}$ can be used to compare the performance of different waveguide types and different waveguide modes with each other. We will refer to this parameter as index sensitivity.

To start our analysis we have calculated the index sensitivity $\frac{\mathrm{d}n_{eff}}{\mathrm{d}g}$ using the FIMMWAVE [31] mode solver. This parameter is expressed in terms of refractive index unit (RIU) per μm (waveguide displacement). In Fig. 4.12 we have plotted $\frac{\mathrm{d}n_{eff}}{\mathrm{d}g}$ for the guided ground mode of both quasi TE (transverse electric) and quasi TM (transverse magnetic) polarization as a function of the substrate-waveguide separation. By definition TE modes have their field vector parallel to the substrate while the TM modes have their field vector perpendicular to the substrate. In practice the guided modes in a silicon wire are not purely TE or TM, but they rather have a hybrid character. Nevertheless we will drop the quasi prefix when referring to the hybrid waveguide modes.

For all the simulations in this chapter we have assumed an excitation wavelength of $1.55\,\mu m$ and a silicon waveguide with a height of $220\,nm$. For the material properties we used the material models which are incorporated in FIMMWAVE ($n_{Si} \approx 3.48$ at $\lambda = 1.55\,\mu m$). For this particular calculation the waveguide width was set to $450\,nm$ and a SiO_2 ($n_{SiO_2} \approx 1.44$) substrate was taken into account.

Of course compared to the TE mode the TM mode is much less confined to the silicon core and therefore its evanescent field interacts much more with the substrate. By consequence its effective index also changes a lot more when moving the waveguide from an infinite distance into contact with the substrate: $n_{TM,g=0} - n_{TM,g=\infty} \approx 1.54 - 1.16 = 0.38\,RIU$ for TM vs. $n_{TE,g=0} - n_{TE,g=\infty} \approx 2.272 - 2.235 = 0.037\,RIU$ for TE so one might think that the index sensitivity should be much larger for TM. In practice we see that for gaps $> 100\,nm$ the index sensitivity does not differ dramatically for both polarizations (Fig. 4.12b).

The strong enhancement of the TM sensitivity takes place at the smallest gaps. As we know from general electromagnetic theory the E-field perpendicular to a material interface tends to be discontinuous at the material interface. For this reason very strong field gradients occur at these interfaces which explains the strong enhancement of $\frac{\mathrm{d}n_{eff}}{\mathrm{d}g}$. The effect we describe here is in fact very similar to the effects encountered in slotted

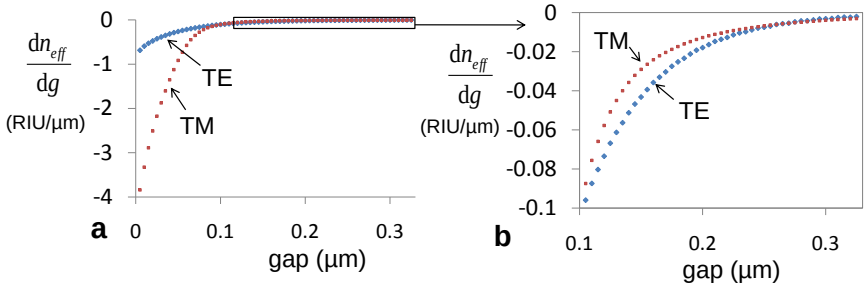

Figure 4.12: **Index sensitivity for a substrate waveguide configuration.** **a**, Index sensitivity $\frac{\mathrm{d}n_{eff}}{\mathrm{d}g}$ for TE and TM polarization in function of the distance between the single-mode waveguide (width 450 nm) and the SiO_2 substrate. **b**, Detail of Fig. 4.12a, showing that TE and TM index sensitivity does not differ much for gaps$> 100\,nm$.

waveguide theory [32, 33].

However for the experiments we restricted ourselves to the TE polarization because the TM polarization raises some technological issues (mainly higher fiber to chip coupling losses). These issues are currently addressed in the Photonics Research Group [34], however, the technology and understanding of TM was not mature enough yet to be implemented in optomechanical experiments. Anyway the use of TM polarization would only be beneficial for gaps smaller than 100 nm.

As explained in the previous section the phase shift can be detected with an MZI or in a ring/racetrack resonator. We only implemented the latter for our theoretical analysis has clearly shown the advantage of a resonator (with sufficiently high finesse) over an MZI. However both options have also been implemented by other research groups and can be found in the literature [35, 36].

A schematic of the device under test is shown in Fig. 4.13. The straight part of a racetrack resonator was underetched at the side where we have no access waveguide. We have chosen the all-pass configuration since we know from our theoretical analysis that this is the best configuration for phase sensing. The finesse $\mathscr{F}$ of this racetrack resonator is around 100 so a clear advantage over an interferometer configuration can be expected.

The recorded trace is shown in Fig. 4.14a. It originates from the out-of-plane brownian motion of the short straight part (beam length $\approx 3.5\,\mu m$) of the racetrack resonator. The power spectral density (PSD) is expressed in $dBm/rtHz = dBm\sqrt{Hz^{-1}}$. The electrical spectrum analyzer measurement bandwidth was $2.15\,kHz$. The symbols are experi-

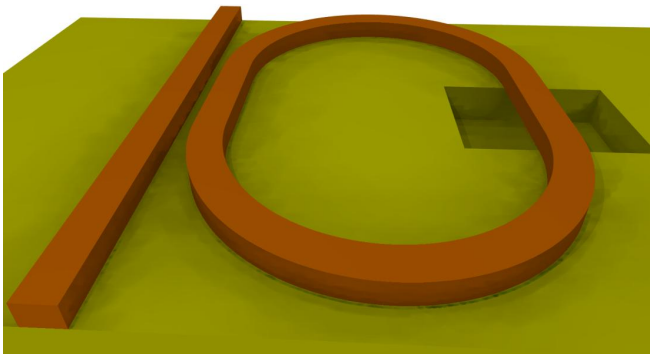

Figure 4.13: Picture of a racetrack resonator with freestanding straight part.

mental data while the solid black line is a fit to equation 2.47. From this fit we learn that the natural frequency is $65.86\,MHz$ while the Q-factor is 5373. With these extracted parameters and assuming $T \approx 300K$ we see that we only need to know the effective mass in this formula to calculate the brownian force. Taking into account the known dimensions of the beam ($220\,nm \times 450\,nm \times 3.6\,\mu m$) and the well documented mass density of silicon we can calculate the mass of the beam. Assuming a hinged-hinged beam we can take the right prefactor from table 2.1 and calculate the effective mass $m_{eff} = 415\,fg$. Since we also know the stiffness now ($k = m_{eff}\omega_0^2$) we can tie the measured signal to a displacement spectral density (DSD) $DSD = \frac{<F_b>}{k}\chi_{MECH}(\omega)$ which is plotted in Fig. 4.14b. Looking at the noise floor we can see that the displacement sensitivity is $0.4\,fm/rtHz$ for this experiment.

We note that compared to the theoretical model for the all-pass ring we have developed in subsection 4.5.3 additional effects come into play. Since the circulating power inside the ring scales with the finesse of the resonator ($\mathscr{F} \approx 100$) we easily can have several tens of mW circulating power even for modest input powers. In the small cross-section ($220\,nm \times 450\,nm$) of the waveguide this gives rise to two-photon-absorption. The absorbed optical power is transferred into heat which changes the temperature of the resonator. Through the thermo-optic effect also the refractive index of the silicon changes [30]. This thermal effect is responsible for the bistability in the optical spectrum of the resonator that is shown in Fig. 4.15a.

When sweeping the wavelength of the tunable laser source we see that the optical output power drops over $40\,\mu W$ from $145\,\mu W$ to $105\,\mu W$, indicating that increasingly more optical power is circulating in the ring. At a wavelength of $1557.5\,nm$ the output power suddenly jumps to $150\,\mu W$

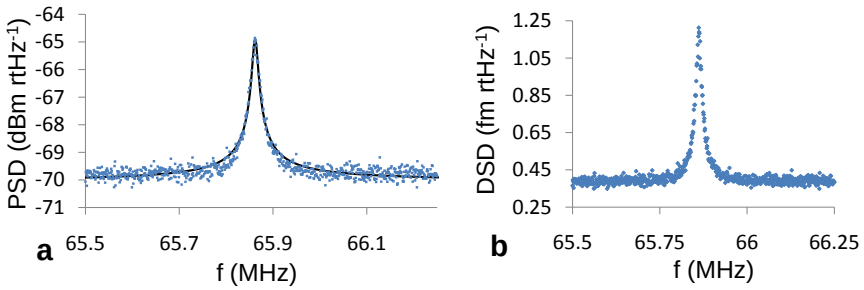

Figure 4.14: **Brownian response of a suspended waveguide in a racetrack resonator.** **a**, The measured out-of-plane vibration of the short straight part ($\approx 3.5\,\mu m$ results in a resonance frequency of $65.86\,MHz$. The power spectral density (PSD) is expressed in $dBm\sqrt{Hz^{-1}}$. The electrical spectrum analyzer measurement bandwidth was $2.15\,kHz$. The solid black line is a fit to equation 2.47. **b**, The same experimental data as in 4.14a are plotted on a linear scale after calibration. The displacement spectral density (DSD) is expressed in $fm\,rtHz^{-1}$. Looking at the noise floor we can see that the displacement sensitivity is $0.4\,fm\,rtHz^{-1}$ for this experiment.

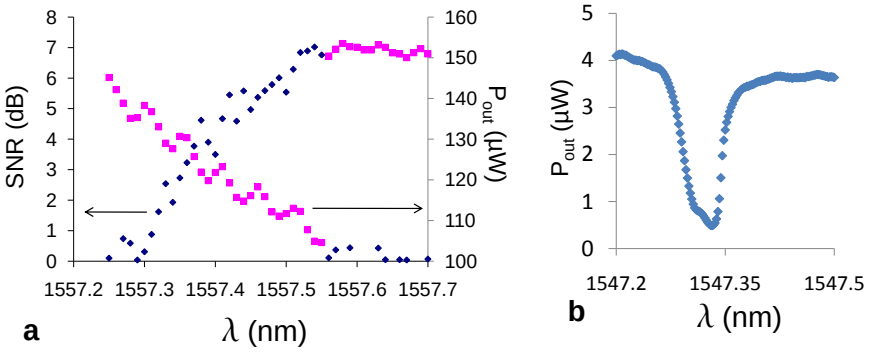

Figure 4.15: **Transmission and transduction of a suspended waveguide in a racetrack resonator.** **a**, Bistable optical transmission spectrum and accompanying measured signal-to-noise-ratio (SNR) of the brownian response. **b**, Transmission dip at very low optical power. Due to reflections in the ring resonator, the recorded dip is not perfectly Lorentzian, but suffers from peak splitting.

indicating that the light is abruptly out of resonance. In parallel we have recorded the brownian response of the beam and plotted its signal-to-noise-ratio (SNR) on the left axis of Fig. 4.15a. The SNR is defined here as the distance between the peak of the vibration signal and the noise floor. The trace in 4.14a for example was taken at $\lambda = 1557.45\,nm$ and has a SNR of $5\,dB$. We see that the SNR increases when more power is circulating through the ring. When the light is out of resonance no vibration signal is measured ($\lambda > 1557.55\,nm$ and $\lambda < 1557.25\,nm$).

In fact even for very low optical powers we do not find a perfect Lorentzian response as can be seen in Fig. 4.15b. Due to reflections in the ring coupling is established between forward and backward propagating modes which results in peak broadening or splitting [37]. The underetch region of course enhances the unwanted reflections in the ring.

In order to instigate really strong optomechanical interactions between a waveguide and a substrate we should in fact work with the TM polarization and separations well below 100 nm (Fig. 4.12). The latter condition cannot be fulfilled with the current fabrication process. Since the BHF etch is isotropic, underetching a waveguide intrinsically also corresponds to a vertical etch depth, limiting the minimum achievable gap severely. In fact $300\,nm$ gaps were reported to be practically achievable [36]. Nevertheless we think that the substrate-waveguide configuration might be very promising to achieve ultrastrong optomechanical interaction anyway.

The last statement is supported by the fact that it is essentially much easier to deposit a material layer with a few nm thickness than etching a slit of a few nm width. If the thickness of the sacrificial SiO_2 layer can be controlled and made very small, then the underlying Si might act as an etch stop layer. Eventually also the Si stop layer can be made very thin and followed by an additional thicker oxide layer to avoid leaking of the light into the substrate. The total stack could be something like: $220\,nm$ top Si, $10\,nm$ sacrificial SiO_2, $10\,nm$ Si etch stop layer, $2\,\mu m$ SiO_2, Si substrate. Given the extremely small gap and the quadratic dependence of the elastocapillary number (see equation 3.6) on the gap of course gaseous HF or at least critical-point-drying would be required. Control over the material layer stack is crucial. However the above proposed stack is perfectly achievable with the amorphous silicon technology that was developed during the Ph.D. of Shankar Kumar Selvaraja [38]. Compared to the current experiments a $10\,nm$ gap would increase the optomechanical interaction with roughly three orders of magnitude.

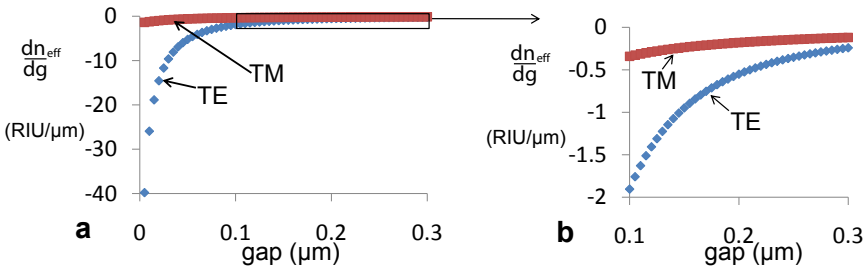

Figure 4.16: **Index sensitivity for a slotted waveguide. a**, Index sensitivity $\frac{\mathrm{d}n_{eff}}{\mathrm{d}g}$ for TE and TM polarization in function of the slot width. A strong increase of the TE index sensitivity can be observed for very small gaps. **b**, Detail of Fig. 4.16a, showing that —also for relatively large gaps— the index sensitivity is larger for TE than TM.

4.6.2 Slotted waveguide

In a slotted waveguide we have a slot (=gap) central in the waveguide cross-section. Light will typically be concentrated in this slot resulting in a strong field enhancement (see Fig. 4.18 for an example of a field mode profile). In contrast with the waveguide-substrate case we expect the TE polarization to yield the largest optomechanical effect. Knowing that the E-field perpendicular to a material interface is discontinuous at this interface, it is obvious that strong field gradients are present for TE in a narrow vertical slot. This qualitative insight is confirmed by numerical simulations. In Fig. 4.16 the index sensitivity $\frac{\mathrm{d}n_{eff}}{\mathrm{d}g}$ is plotted for both the ground mode for TE and TM in a slotted waveguide. The quantity on the horizontal axis is the slot width, the total waveguide width is $2 \times 225\, nm$ (Si beam) + slot width. We see that —as expected— the index sensitivity is larger for TE and TM, especially for very small gaps where an exponential increase can be observed.

Due to the lower index contrast, slotted waveguides exhibit higher bend losses and consequently it is more difficult to implement them in a ring resonator configuration. We have chosen to implement a straight underetched slotted waveguide in a Fabry-Pérot resonator. The reflective mirrors that are required to construct the cavity are in fact Distributed Bragg Reflectors (DBR). Our 'wing type' DBR is implemented in a waveguide with 800 nm width. The wings are 1200 nm wide. Since waveguides of 800 and 1200 nm width have different effective indices a DBR is created in the waveguide (Fig. 4.19b). We found (experimentally) that periods around 310 nm (with fill factor 50%) yield strong reflective behavior of the DBRs

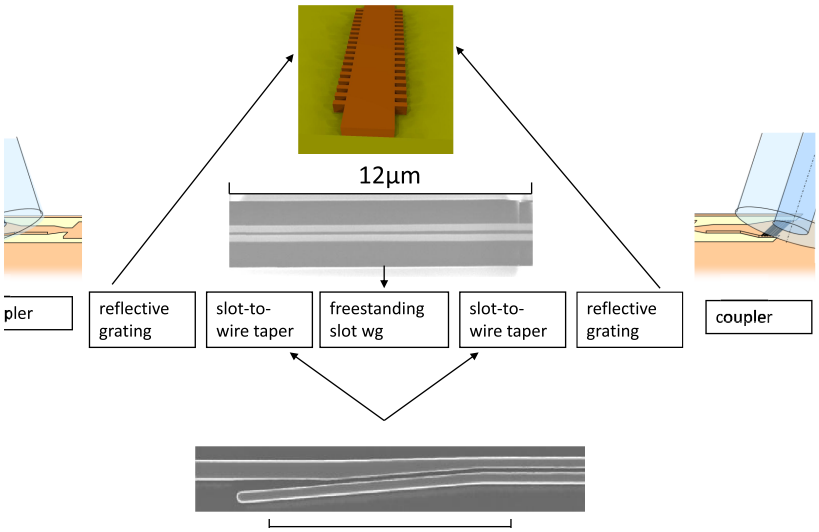

Figure 4.17: **Sketch of the slotted waveguide optomechanical device.** The light is coupled in and out of the chip through a grating coupler. The reflective gratings form the FP cavity. In the center of the cavity the free-standing slotted waveguide can be found. The slot-to-wire tapers ensure the conversion from an ordinary nanophotonic wire to a slotted waveguide and vice versa.

around $\lambda = 1.55\,\mu m$. At both sides inside the cavity tapers are required to taper the 800 nm waveguide first to a nanophotonic wire (450 nm width) and subsequently to a slotted waveguide through a compact mode-converter taper [39]. A sketch of the full device is shown in Fig. 4.17.

A transmission spectrum of an FP resonator formed by a slotted waveguide in between two of these wing type DBRs (with 100 periods) is shown in Fig. 4.19a. The free spectral range (FSR) is rather small (around $1.2\,nm$) because of the long cavity length (around a few $100\,\mu m$ and $FSR \approx \frac{\lambda^2}{2n_{eff}L}$). Given the low index contrast of the DBR the reflectivity wavelength band is not too wide (around $10\,nm$) and the power reflectivity R of the DBRs is dependent on the wavelength. The central stopband in the spectrum can be interpreted as a region where the reflectivity is very high and hence the transmission is low. In fact not enough light is transmitted to compensate for the large cavity losses. This zero transmission spectrum is equivalent to the drop spectrum of an add-drop ring filter with very high losses in the ring.

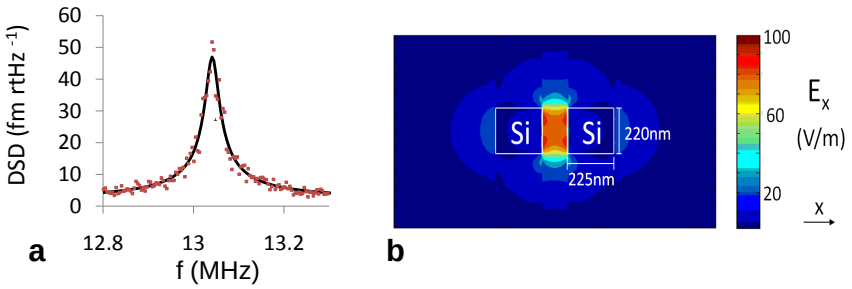

Figure 4.18: **Brownian displacement spectral density and slotted waveguide mode profile. a**, The measured DSD, generated by the in-plane vibration of one of the two beams of a suspended slotted waveguide (suspended length $\approx 11.5\,\mu m$). The electrical spectrum analyzer measurement bandwidth was $10\,Hz$. The solid black line is a fit to equation 2.47. We find a resonance frequency of $13.05\,MHz$ and $Q = 430$. **b**, Mode profile of the TE ground mode a slotted waveguide with slot width 120 nm. The typical concentration of light in the slot is clearly visible.

However because of the wavelength dependence of the reflectivity R(λ), for wavelengths at the edge of the stop band the reflectivity is less high and 3 to 4 FP transmission peaks can be observed at each side of the stop band. In spite of the high losses (tapers, slotted waveguide) inside the cavity (and a mirror reflectivity that is in fact too high for these losses) the proposed design is sufficient to detect brownian noise of a freestanding part of the slotted waveguide. If the probe wavelength is chosen at the edge of the FP transmission peaks the vibration induced phase variations in the cavity are transduced into a modulated power signal. The result of such an experiment is shown in Fig. 4.18. The measured DSD is generated by the in-plane vibration of one of the two beams of a suspended slotted waveguide (suspended length $\approx 11.5\,\mu m$). We find a resonance frequency of $13.05\,MHz$ and $Q = 430$. In fact the overall displacement sensitivity ($3\,fm\,rtHz^{-1}$) is rather disappointing compared to the previous case (out-of-plane vibration in ring resonator). The advantage of the increased index sensitivity is annihilated by the strongly reduced resonator performance.

Nevertheless we think that experiments with slotted waveguides have great potential. First of all it is very clear that the resonator performance can be improved drastically. Again also control of the material layer stack is desired to overcome resolution limits of lithographic processes. As a practical example let us consider the material stack that has recently been used to fabricate fiber a coupler with enhanced coupling efficiency [34].

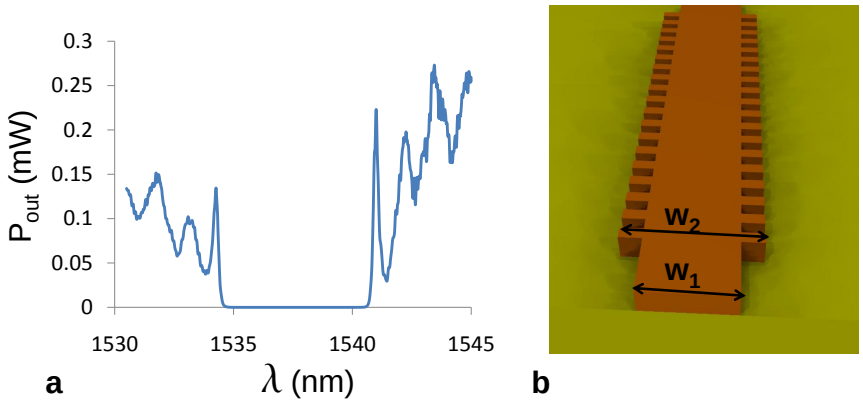

Figure 4.19: **Transmission spectrum from a DBR-wing type FP-resonator. a**, Transmission spectrum of an FP-resonator formed by a slotted waveguide in between two wing-type DBRs. The observed spectrum can be explained (see plain text) through the strong wavelength dependent reflectivity R(λ) and the losses in the cavity. The DBR reflection band and six FP transmission peaks can be clearly observed. **b**, Distributed Bragg Reflector in a 800 nm wide waveguide with 1.2 μm wide wings.

In this process the 220 nm silicon top layer of a SOI wafer can be locally thickened with an additional 160 nm amorphous (or polycrystalline) silicon layer. In between is a thin layer (typically 5 nm) of thermal oxide (see Fig. 4.20a for the material stack). Etching a 500 nm wide waveguide in this stack (up to the 2μm buried silica layer, Fig. 4.20b) and removing locally the silica layers (Fig. 4.20c) would result in an index sensitivity of approximately $-40\,RIU\,\mu m^{-1}$ for TM polarization (out-of-plane vibration). If one succeeds to plug such a waveguide into a racetrack resonator like the one shown in Fig. 4.13 (the freestanding straight part would look like the cross-section in Fig. 4.20c), an extremely powerful sensing device could arise.

A parameter that is very popular in literature to assess the interaction between an optical resonator and a mechanical degree of freedom is the g_{OM} parameter. It describes how much the optical resonance frequency of an optical resonator shifts for a given displacement of the mechanical structure and is by consequence is typically expressed in units of $GHz\,nm^{-1}$. A racetrack resonator that is fabricated using the advanced passives process and is suspended over its full length exhibits a $g_{OM} \approx 1839\,GHz\,nm^{-1}$. To calculate this number we have used $\frac{\partial f_0}{\partial g} = \frac{\partial n_{eff}}{\partial g}\frac{c}{\lambda_0 n_g}$

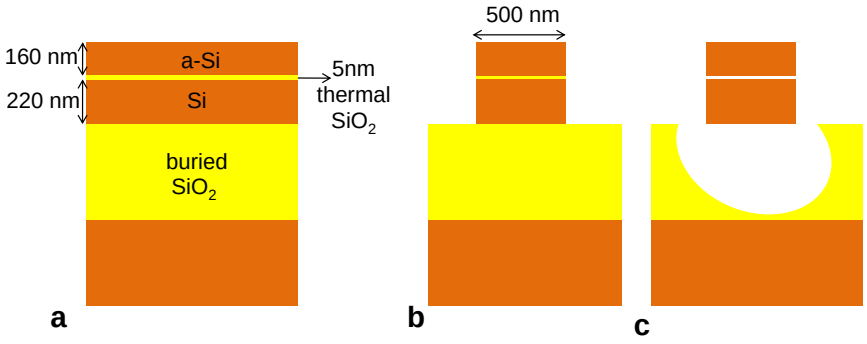

Figure 4.20: **Optomechanical device based on the advanced passives process. a**, Material stack. On top of the 220 nm monocrystalline Si layer a 160 nm layer amorphous Si is deposited. In between is a layer of 5 nm thermal oxide. **b**, A waveguide is etched in the material stack. D. **c**, Removing the SiO_2 results in two suspended beams with a narrow gap in between.

[29] where $n_g \approx 4.21$ is the group index, f_0 the optical resonance frequency and $\lambda_0 = 1.55\,\mu m$. A fully suspended resonator is of course not easy to fabricate. If we consider a racetrack resonator with a bend radius of $3\,\mu m$ that is only suspended over its straight part (and assuming $1\,\mu m$ length) then g_{OM} drops to $88.4\,GHz\,nm^{-1}$.

However if we compare this number to values in the literature it is still considerably high. For example one of the best structures that was recently demonstrated is a photonic crystal cavity structure with $g_{OM} = 123\,GHz\,nm^{-1}$ [40] and another one with $g_{OM} = 66\,GHz\,nm^{-1}$ [41]. With a double ring configuration $31\,GHz\,nm^{-1}$ [42] and $1.25\,GHz\,nm^{-1}$ [33] were achieved. Experiments with high finesse silica microtoroids and an external silicon nitride membrane acting as a mechanical oscillator achieved almost $0.02\,GHz\,nm^{-1}$ [43]. Of course g_{OM} is not the only parameter that is of importance. It is also challenging to maintain a high g_{OM} together with high mechanical Q's, high mechanical resonance frequencies and high finesse optical cavities. It is noteworthy that optical losses for the TM polarization can be potentially lower because the effects of sidewall roughness decrease and we conclude that the proposed (advance passives) structure indeed seems of great potential. We also note that the Casimir effect might come into play when designing optomechanical devices with nanogaps. The Casimir effect is a quantummechanical phenomenon and predicts that two closely spaced parallel metal plates placed in vacuum experience a force, even in the absence of an external field. Recently it has been theoretically predicted that also for silicon structures with nanogaps,

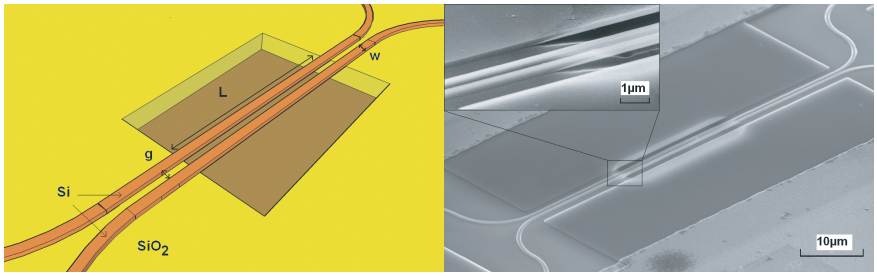

Figure 4.21: **Underetched directional coupler. a**, Schematic drawing. **b**, SEM picture: the inset shows the clamping region in greater detail.

this effect might be non-negligible [35].

4.6.3 Parallel waveguides

In Fig. 4.21 a directional coupler with a freestanding part is shown. Parallel waveguides have the intrinsic advantage that the phase changes that are induced through vibration are directly converted to a power modulated signal. This is possible because the coupling effect can be seen as the result of the interference of the two guided modes that are present in a parallel waveguide structure.

According to section 4.4 the transduction coefficient for a directional coupler (with a freestanding part of length L) reads as:

$$\frac{\mathrm{d}T_{x,bar}}{\mathrm{d}g} = -\frac{\sin(\frac{2\pi(n^+-n^-)}{\lambda}L)}{2}\frac{\mathrm{d}(n^+-n^-)}{\mathrm{d}g}\frac{2\pi}{\lambda}L \tag{4.31}$$

n^+ and n^- are the ground mode and second guided mode of the parallel waveguide structure respectively (also called the 'supermodes').

Usually λ is chosen such that $\frac{2\pi(n^+-n^-)}{\lambda}L = \frac{\pi}{2} + k\pi$. The directional coupler acts as a 3-dB splitter in that case and the transduction coefficient reduces to:

$$\frac{\mathrm{d}T_{x,bar}}{\mathrm{d}g}|_{MAX} = \frac{\mathrm{d}(n^+-n^-)}{\mathrm{d}g}\frac{\pi}{\lambda}L \tag{4.32}$$

From this last equation we can see that in this particular case we should not evaluate the index sensitivity of the individual modes. Instead we are rather interested in $\frac{\mathrm{d}(n^+-n^-)}{\mathrm{d}g}$. n^+ and n^- are plotted for both TE and TM in Fig. 4.22. We see that the indices of the supermodes converge to the

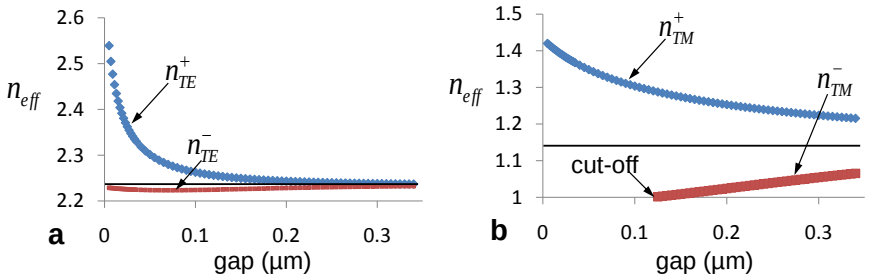

Figure 4.22: **Effective indices of the guided modes in a directional coupler (waveguide width 450 nm).** **a**, Effective index of the ground mode n_{TE}^{+} and second guided mode n_{TE}^{-} in function of the gap. In the limit of large gaps both indices converge to the effective index of a single-mode waveguide, indicated by the black solid line ≈ 2.235. **b**, Same plot for TM polarization (single-mode index ≈ 1.155). The second mode goes in cut-off for gaps smaller than 125 nm.

effective index of a single-mode waveguide (indicated by the black solid lines, $n_{TE} = 2.235$ and $n_{TM} = 1.155$) in the large gap limit. For TE polarization (Fig. 4.22a) the sharp increase in effective index for the ground mode is striking. The behavior of the second mode is non-monotone, its effective index reaches a minimum for a gap of 70 nm. For larger gaps the effective index can be seen to increase with larger gap ($\frac{\mathrm{d}n^-}{\mathrm{d}g} > 0$). We will come back to this interesting behavior in chapter 5 when discussing repulsive forces. For TM polarization (Fig. 4.22b) the second mode goes in cut-off for gaps smaller than 125 nm. Modes close to cut-off also tend to be lossy, so TM polarization is anyway not a good choice for experimental implementation.

In Fig. 4.23 $\frac{\mathrm{d}(n^+ - n^-)}{\mathrm{d}g}$ is plotted. As expected the TE polarization shows the largest index sensitivity. As can be seen in the previous graph the ground mode is responsible for the sharp increase at small gaps.

Finally experiments were performed on structures similar to the one shown in Fig. 4.21a. We have first recorded the directional coupler transmission spectrum of the BAR arm (see Fig. 4.6 for definition of BAR). The BAR spectrum is shown in Fig. 4.24a (right axis). The wavelengths with maximum and minimum (=maximum optical power in CROSS-arm) transmitted power have been labeled with arrows (P_{MAX} and P_{MIN}). The wavelengths where the directional coupler acts as 3dB-splitter are labeled P_{3dB}. In parallel with the transmission spectrum the peak of the brownian signal was also recorded to investigate how the transduction evolves with

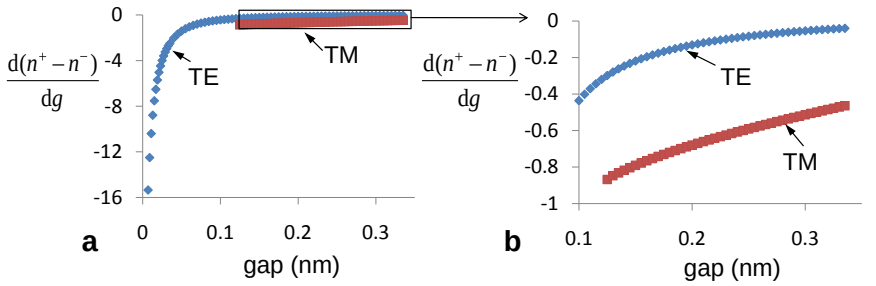

Figure 4.23: **Index sensitivity in a directional coupler. a**, $\frac{\mathrm{d}(n^+ - n^-)}{\mathrm{d}g}$ in function of the gap for both polarizations. **b**, detail of Fig. 4.23a.

wavelength (left axis). In agreement with the theory we can see that the directional coupler is most sensitive when the optical power is equally divided over its output arms while for maxima and minima in the transmission spectrum the transduction is minimal. In Fig. 4.24b a recorded brownian DSD is shown after calibration. We have two peaks with slightly different resonance frequencies because there are also two freestanding waveguides with slightly different geometrical properties.

The freestanding directional coupler can also be inserted as splitter/-combiner in an unbalanced Mach-Zehnder interferometer. 'Unbalanced' in this case means that one arm of the interferometer is much longer (ΔL) than the other such that the light in this arm exhibits a phase delay ϕ_{delay}. The freestanding coupler has a length L and supermode effective indices n^+ and n^-. A sketch of the device is shown in Fig. 4.25a. If we assume that the second coupler is an ordinary 3dB-splitter then the transmission spectrum of this structure reads as [44]:

$$T_{x,bar,MZI}(\lambda) = \frac{1}{2}[1 + \sin(\phi_{delay}) \sin\left(\frac{2\pi\,(n^+ - n^-)\,L}{\lambda}\right)] \qquad (4.33)$$

The transduction coefficient reads as:

$$\frac{\mathrm{d}T_{x,bar,MZI}}{\mathrm{d}g} = -\sin(\phi_{delay})\frac{\mathrm{d}(n^+ - n^-)}{\mathrm{d}g}\frac{\pi}{\lambda}L\cos\left(\frac{2\pi\,(n^+ - n^-)\,L}{\lambda}\right) \qquad (4.34)$$

Assuming that also the waveguide coupler is a 3dB-splitter we find a simple expression for the transduction coefficient:

$$\frac{\mathrm{d}T_{x,bar,MZI}}{\mathrm{d}g}|_{MAX} = -\sin(\phi_{delay})\frac{\mathrm{d}(n^+ - n^-)}{\mathrm{d}g}\frac{\pi}{\lambda}L \qquad (4.35)$$

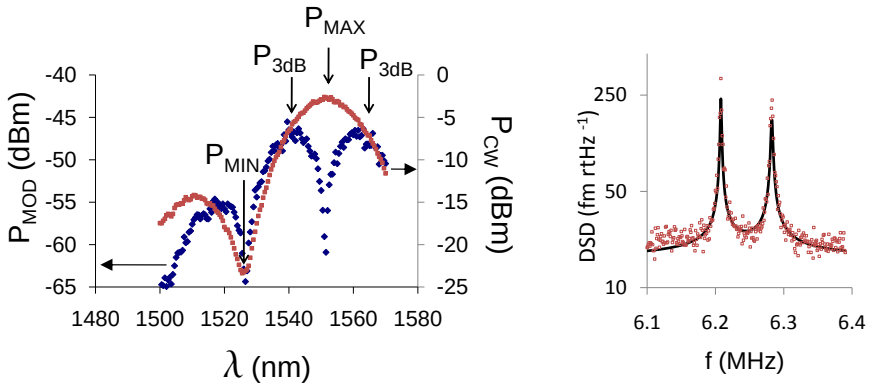

Figure 4.24: **Transmitted power, transduction and brownian noise. a**, Transmitted continuous wave power P_{cw} spectrum (right axis) of a directional coupler (BAR arm, see Fig. 4.6 for definition). When looking at the corresponding brownian noise power P_{MOD} (left axis) we see that at the maximum P_{MAX} and minimum P_{MIN} transmitted power the transduction is minimal. In agreement with the theory we also see that the transduction is maximum when the directional coupler works as a 3dB-splitter (P_{3dB}). **b**, Recorded brownian DSD. Extracted parameters are $f_{res,1} = 6.207\,MHz$, $f_{res,2} = 6.281\,MHz$, $Q_{MECH,1} = 2669$ and $Q_{MECH,2} = 2710$

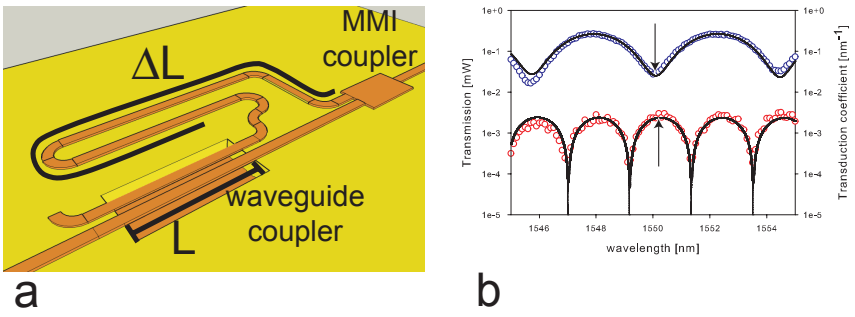

Figure 4.25: **Waveguide directional coupler in an unbalanced MZI. a**, Schematic drawing of the device. The freestanding waveguide coupler (length L) acts as one of the couplers in an MZI. The other coupler is an ordinary 3dB-splitter of the Multi-Mode interferometer type (MMI). One arm of the MZI is ΔL longer than the other. **b**, Experimentally obtained transmission and transduction coefficient of the structure. The arrows indicate a point with minimum transmission and maximum transduction. The black solid lines are fits to equations 4.33 and 4.34

When we compare this expression to equation 4.32 we see that depending on the delay $\phi_{delay} = \frac{2\pi n_{eff}\Delta L}{\lambda}$ the transduction coefficient can only be smaller or in the best case be equal to the transduction of a simple directional coupler, so for small displacement sensing the proposed structure does not offer any advantages at first sight. However in chapter 5 we will show how this structure enables control of the mode excitation in the freestanding waveguide coupler. Looking at the transmission and transduction spectrum in Fig. 4.25b we also see that —in contrast with a simple directional coupler— the wavelengths of maximum transduction correspond to minima and maxima in the transmission spectrum. In other words we can effectively measure the brownian vibration response using wavelengths that intrinsically exhibit a very low continuous wave output power. In the next section we will explain that the low output power is beneficial when used in combination with optical amplifiers and higher displacement sensitivities can be achieved.

4.7 Noise limitations

Noise limits the actual minimum vibration amplitude that can be sensed through the integrated nanophotonic waveguide transducers. First of all it is interesting to note that in our experiments environmental vibrations were of less importance than one might intuitively think. We work mainly in the frequency domain and (almost) all data are taken using an electrical spectrum analyzer. This spectrum analyzer contains an electrical band pass filter which filters out the frequency band of interest and blocks unwanted frequency components. In practice our frequencies of interest lie in the MHz range and environmental vibrations are found in a much lower frequency band (kHz). For example vibrations of the input and output fiber -a typical source of noise in many integrated optics experiments- are filtered out.

The noise factor which is —in first instance— truly the limiting factor for our experiments is receiver noise. However we will also show in this section that receiver noise can in fact be overcome in many practical cases by amplifying the optical signal prior to detection. In that case amplifier noise finally limits the transducer performance.

4.7.1 Receiver noise

Shot noise and thermal noise are two fundamental noise mechanisms responsible for current fluctuations in optical detectors even when the incident optical power is constant. The thermal noise is actually the Johnson-Nyquist noise we have discussed previously and is dominant in most practical situations (and also for our experiments). Its effect is often quantified through a quantity called noise-equivalent power (NEP). The NEP is defined as the minimum detectable optical power per unit of square root bandwidth. The receiver NEP of the Agilent 71400 Light wave signal analyzer is approximately $-73\,dBm\,\sqrt{Hz^{-1}}$. Taking into account that the smallest measurement bandwidth that can be set on this device is $10\,Hz$ we know that the smallest detectable (modulated) power signal is around $-68\,dBm$. However when assessing and calibrating transducer systems the excitation force of interest is of brownian origin and scales with (electrical) measurement bandwidth (consequently the displacement sensitivity of a transducer system is usually expressed in dimensions of $m\sqrt{Hz^{-1}}$. We understand now that reducing the measurement bandwidth any further (when it is already sufficiently smaller than the mechanical resonance linewidth) is of no use: when characterizing the thermal mechanical noise response of a mechanical oscillator the useful signal is also reduced when reducing the

electrical measurement bandwidth. Nevertheless because receiver noise is dominant we implemented another strategy to increase the SNR.

4.7.2 Preamplification prior to detection

Optical amplifiers are routinely used in optical telecom networks for improving sensitivity of optical receivers by preamplifying the optical signal before it falls on the photodetector. Preamplification of the optical signal makes it strong enough such that thermal noise becomes negligible compared with the noise that is added by the optical amplifier. Under this condition the most important issue is the distortion of the amplified signal by amplified spontaneous emission (ASE). Because of the incoherent nature of spontaneous emission, the amplified signal (SNR_{OUT}) is noisier than the input signal (SNR_{IN}), degrading the SNR. The SNR degradation is quantified through a parameter $F_n = \frac{SNR_{IN}}{SNR_{OUT}}$ called the amplifier noise figure. Even an ideal amplifier would have a F_n of $3\,dB$. Realistic amplifiers such as Semiconductor Optical Amplifiers (SOA) typically show a noise figure of $5 - 7\,dB$. For our experiments we choose Erbium-Doped Fiber Amplifiers (EDFA) which have a lower F_n ($4 - 5.5\,dB$).

Because the photodetector responds to the intensity, which is proportional to the square of the fields, the optical noise gets converted in two electrical beat noise components. Roughly speaking we get the terms corresponding to $(signal + noise)^2 = signal^2 + noise^2 + 2\,noise\,signal$. The first term is the useful signal, the second term is the spontaneous-spontaneous beat noise and the third term is called the signal-spontaneous beat noise. A more detailed analysis shows that the variance of current fluctuations $\sigma^2 = < (\Delta I)^2 >$ due to spontaneous-spontaneous and signal-spontaneous beat noise can be written as [45]:

$$\begin{aligned} \sigma^2 &= \sigma^2_{sig-sp} + \sigma^2_{sp-sp} \\ \sigma^2_{sig-sp} &= 4R^2 S_{sp} \Delta f_{elec}\; GP_s \\ \sigma^2_{sp-sp} &= 4R^2 S_{sp} \Delta f_{elec}\; S_{sp} \Delta \nu_{opt} \end{aligned} \tag{4.36}$$

In these formulas P_s is the (DC) optical signal power before amplification, G is the amplifier gain and R is the responsivity of the detector so a signal current $I = RGP_s$ is generated. The spectral density of the spontaneous emission induced noise S_{sp} can also be expressed in terms of the amplifier noise figure, the amplifier gain and the average photon energy $h\nu$: $S_{sp} \approx \frac{1}{2} G h\nu F_n$. Given the linear and quadratic dependence on F_n

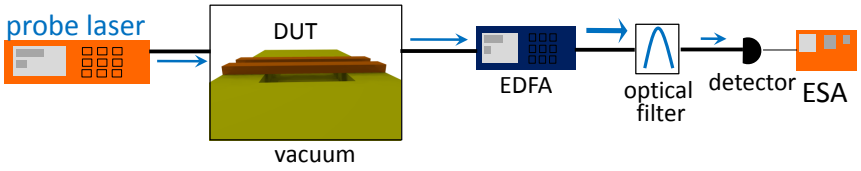

Figure 4.26: **Preamplification setup.** After transmission through the chip containing the device-under-test (DUT) the probe signal is amplified and filtered prior to falling onto the photodetector.

of σ^2_{sig-sp} and σ^2_{sp-sp} the importance of an amplifier with low noise figure is clear. Also the electrical bandwidth Δf_{elec} is of crucial importance, however, as explained in the previous subsection reducing the electrical measurement bandwidth is at some point no longer beneficial when characterizing thermal mechanical noise.

Due to its dependence on the optical bandwidth $\Delta\nu_{opt}$ the spontaneous-spontaneous beat noise (see equation 4.36) can in principle easily be reduced by placing an optical band-pass filter after the optical amplifier. Such a measurement setup is shown in Fig. 4.26. So finally we can conclude that ultimately the signal-spontaneous beat noise sets the achievable displacement sensitivity. In fact we noticed that in practice —even without optical bandpass filter— the signal-spontaneous dominates the noise when the signal power P_s is on the order of a few tens of μW or higher. However in structures where the transduction coefficient is intrinsically large for low transmissions the (DC) optical signal power P_s can be very low, hence offering a possibility to reduce the signal-spontaneous beat noise drastically.

The above noise limitation analysis is clearly illustrated through Fig. 4.27. The curves that are shown in this figure are all thermal noise responses from the same underetched waveguide (mechanical ground mode resonance frequency around $2.79\,MHz$, Q_{mech} around 6000 in vacuum) which is part of a directional coupler. The directional coupler itself acts as a 3 dB splitter in an MZI (we actually discussed this type of device previously, see Fig. 4.21). The extinction in the interferometer due to destructive interference can be high for certain wavelengths (extinction ratio $> 30\,dB$ for $\lambda = 1549.95$) and hence the intrinsic transmission of the MZI is low. For this particular device and wavelength we finally have an input power of $-37\,dBm$ at the photodetector. Using this low (DC) optical power the blue curve (labeled 'no preamp') in Fig. 4.27 was recorded. The electrical measurement bandwidth of the electrical spectrum analyzer (ESA) was set to $100\,Hz$ for all data series in the graph. We note that the brownian signal exceeds the noise floor of the ESA by only $5\,dB$ approximately. The noise

floor in this case is clearly set by thermal receiver noise.

The picture changes drastically when the optical signal is preamplified through an EDFA prior to detection ($0\,dBm$ at the detector). Looking at the red data points (labeled 'preamp, no filter') we see that the noise floor is raised over $11\,dB$, however the useful signal now peaks $16\,dB$ above the noise floor. Knowing that spontaneous-spontaneous beat noise is reduced by reducing the optical bandwidth (but signal-spontaneous noise is not, see equation 4.36) we placed an optical bandpass filter ($2.4\,nm$ optical bandwidth) after the EDFA and obtained the green curve (labeled 'preamp with filter'). We see that the use of the filter provides us with an additional $5\,dB$ of useful signal and finally we obtain a signal that exceeds the noise floor by $21\,dB$. The fact that adding the filter improved the signal quality proves that spontaneous-spontaneous beat noise was the limiting noise factor for the preamplification experiment without filter (red curve). Estimating the bandwidth of the EDFA around $40 - 50nm$, adding the $2.4\,nm$ the filter has reduced the spontaneous-spontaneous beat noise over (roughly) a factor 20. Additional experiments with smaller bandwidth optical filters ($0.6\,nm$) did not yield any significant improvement anymore, indicating that finally signal-spontaneous beat noise is the limiting noise factor for the green data series.

Compared to the not preamplified trace the overall improvement of the displacement sensitivity ($16\,dB$) is dramatic. After calibration we find that the displacement sensitivity has been improved from 80 to $2\,fm\,Hz^{-\frac{1}{2}}$ In fact the preamplification technique enabled experiments that require considerable displacement sensitivities and that would not have been possible otherwise. For example the brownian signal of the suspended beam in the ring resonator was recorded using preamplification (the optical power on the y-axis in Fig. 4.15 is in fact the power before preamplification). This mechanical mode with resonance frequency $65.86\,MHz$ (and hence relatively high stiffness $k \propto f_{res}^2$) would have stayed hidden without preamplification. Moreover the improved quality of the brownian noise signal also enabled feedback experiments. In these experiments the brownian signal is used to create optical feedback forces (see chapter 6). Although amplification of optical signals in order to improve their quality is not novel as such, the application of the technique in an optomechanical sensing context is.

4.8 Chapter summary

Summarizing this chapter we have learnt that damped mechanical oscillators are subject to a temperature driven noise force through the fluctu-

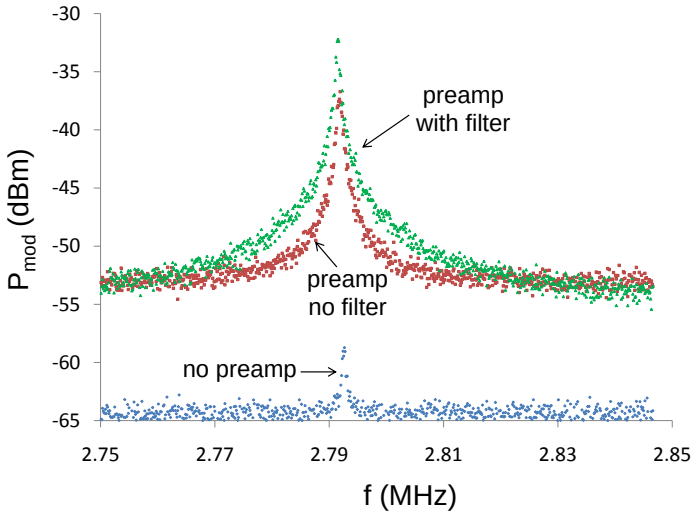

Figure 4.27: **The effect of optical preamplification prior to detection**. All three curves originate from the same underetched waveguide which is part of a directional coupler that acts as splitter/combiner in an MZI. The device has intrinsically a low transmission (MZI with extinction ratio $> 30\,dB$) for the wavelength ($\lambda = 1549.95$), only $-37\,dBm$ is available at the detector. For all curves the measurement BW of the electrical spectrum analyzer (ESA) was set to $100\,Hz$. The lower (blue, labeled 'no preamp') trace was recorded with the $-37\,dBm$ signal. We see that the signal peaks only $5\,dB$ above the ESA noise floor which is dominated by thermal receiver noise. For the red curve (labeled 'preamp, no filter') an EDFA was used for preamplification. The noise floor (now dominated by spontaneous-spontaneous beat noise) has risen over $11\,dB$. The brownian mechanical signal however peaks $16\,dB$ above the noise floor. The green curve (labeled 'preamp with filter') was obtained with an EDFA and an optical filter of $2.4\,nm$ bandwidth placed in series. The noise floor is now dominated by signal-spontaneous beat noise and we finally have $21\,dB$ of useful signal vs. noise floor.

ation dissipation theorem. This noise force can be used for calibration of other forces. However scalable powerful motion transduction schemes are required. For applications that benefit from miniaturization the motion transduction technique must also be scalable to submicrometer dimensions and preferentially be fully integrated. By consequence we have introduced novel on-chip nanophotonic motion transducers that we have extensively studied in our research work. We have elaborated on substrate-waveguide, slotted waveguide and parallel waveguide configurations for nanomechanical motion transduction. By analysis of the limiting noise factors we have shown that in some cases small displacement sensing can be enhanced dramatically through preamplification of the optical signal.

Bibliography

[1] L. Novotny and Hecht B. *Principles of Nano-Optics*, chapter 14.

[2] Herbert B. Callen and Theodore A. Welton. Irreversibility and generalized noise. *Phys. Rev.*, 83(1):34–40, Jul 1951.

[3] R. Kubo. Fluctuation-dissipation theorem. *Reports on Progress in Physics*, 29(Part 1):255–&, 1966.

[4] T.B. Gabrielson. Mechanical-thermal noise in micromachined acoustic and vibration sensors. *IEEE Transactions on electron devices*, 40(5):903–909, 1993.

[5] H. Nyquist. Thermal agitation of electric charge in conductors. *Phys. Rev.*, 32(1):110–113, 1928.

[6] J.E. Sader, I. Larson, P. Mulvaney, and L.R. White. Method for the calibration of atomic-force microscope cantilevers. *Review of Scientific Instruments*, 66(7):3789–3798, 1995.

[7] H. Baltes, O. Brand, G.K. Fedder, C. Hierold, Korvink J.G., and Tabata O. *Enabling Technology for MEMS and Nanodevices*, chapter 3. Wiley, 2004.

[8] S. Rudra, J. Roels, G. Bryce, L. Haspeslagh, A. Witvrouw, and D. Van Thourhout. SiGe based grating light valves: A leap towards monolithic integration of MOEMS. *Microelectronic Engineering*, 87(5-9):1195–1197, 2008. The 35th International Conference on Micro- and Nano-Engineering, MNE.

[9] J. Roels, W. Van der Tempel, D. Van Nieuwenhove, R. Grootjans, M. Kuijk, D. Van Thourhout, and R. Baets. Continuous Time-of-Flight Ranging using a MEMS diffractive subwavelength period grating (de)modulator. *IEEE Photonics Technology Letters*, 20(21-24):1827–1829, 2008.

[10] I. De Vlaminck, J. Roels, D. Taillaert, D. Van Thourhout, R. Baets, L. Lagae, and G. Borghs. Detection of nanomechanical motion by evanescent light wave coupling. *Applied Physics Letters*, 90(23), 2007.

[11] A.N. Cleland and M.L. Roukes. Fabrication of high frequency nanometer scale mechanical resonators from bulk Si crystals. *Applied Physics Letters*, 69(18):2653–2655, 1996.

[12] A.N. Cleland and M.L. Roukes. External control of dissipation in a nanometer-scale radiofrequency mechanical resonator. *Sensors and Actuators A-Physical*, 72(3):256–261, 1999.

[13] S.B. Shim, M. Imboden, and P. Mohanty. Synchronized oscillation in coupled nanomechanical oscillators. *Science*, 316(5821):95–99, 2007.

[14] S. Tadigadapa and K. Mateti. Piezoelectric MEMS sensors: state-of-the-art and perspectives. *Measurement Science & Technology*, 20(9), 2009.

[15] I. Bargatin, E.B. Myers, J. Arlett, B. Gudlewski, and M.L. Roukes. Sensitive detection of nanomechanical motion using piezoresistive signal downmixing. *Applied Physics Letters*, 86(13), 2005.

[16] Sotiris C. Masmanidis, Rassul B. Karabalin, I. De Vlaminck, G. Borghs, Mark R. Freeman, and Michael L. Roukes. Multifunctional nanomechanical systems via tunably coupled piezoelectric actuation. *Science*, 317(5839):780–783, 2007.

[17] A. D. O'Connell, M. Hofheinz, M. Ansmann, Radoslaw C. Bialczak, M. Lenander, E. Lucero, M. Neeley, D. Sank, H. Wang, M. Weides, J. Wenner, John M. Martinis, and A. N. Cleland. Quantum ground state and single-phonon control of a mechanical resonator. *Nature*, 464(7289):697–703, 2010.

[18] G. Nunes and M.R. Freeman. Picosecond Resolution in scanning-tunneling-microscopy. *Science*, 262(5136):1029–1032, 1993.

[19] T.W. Kenny, W.J. Kaiser, J.K. Reynolds, J.A. Podosek, H.K. Rockstad, E.C. Vote, and S.B. Waltman. Electron Tunnel Sensors. *Journal of Vacuum Science & Technology A-Vacuum Surfaces and Films*, 10(4, Part 2):2114–2118, 1992. 38th National Symposium of the American Vacuum Society, Seattle, WA, Nov 11-15, 1991.

[20] T. Kouh, D. Karabacak, D.H. Kim, and K.L. Ekinci. Diffraction effects in optical interferometric displacement detection in nanoelectromechanical systems. *Applied Physics Letters*, 86(1), 2005.

[21] D. Karabacak, T. Kouh, C.C. Huang, and K.L. Ekinci. Optical knife-edge technique for nanomechanical displacement detection. *Applied Physics Letters*, 88(19), 2006.

[22] B. Ilic, S. Krylov, K. Aubin, R. Reichenbach, and H.G. Craighead. Optical excitation of nanoelectromechanical oscillators. *Applied Physics Letters*, 86(19), 2005.

[23] D. Kleckner and D. Bouwmeester. Sub-kelvin optical cooling of a micromechanical resonator. *Nature*, 444(7115):75–78, 2006.

[24] I. De Vlaminck. *Nanoscale resonators in optics and mechanics: development of electromechanical and optoelectronic transducers*. PhD thesis, Katholieke Universiteit Leuven, Leuven, Belgium, 2008.

[25] Y. Li, S. Meersman, and R. Baets. Optical frequency shifter on SOI using thermo-optic serrodyne modulation. pages 75–78, 2010. IEEE Group IV Photonics, Bejing, China.

[26] J. De Coster, L. Haspeslagh, A. Witvrouw, and I. De Wolf. Long-term reliability measurements on MEMS using a laser-Doppler vibrometer. In Quan, C. and Asundi, A., editor, *Ninth International Symposium on laser metrology, Pts 1 and 2*, volume 7155 of *Proceedings of the society of photo-optical instrumentation engineers (SPIE)*, page G1550, 2008. 9th International Symposium on Laser Metrology, Singapore, JUN 30-JUL 02, 2008.

[27] K.L. Ekinci. Electromechanical transducers at the nanoscale: Actuation and sensing of motion in nanoelectromechanical systems (NEMS). *Small*, 1(8-9):786–797, 2005.

[28] R. März. *Integrated Optics, Design and Modeling*. Artech House Publishers, 1995.

[29] P. Dumon. *Ultracompact Integrated Optical Filters in Silicon-on-Insulator by Means of Wafer-Scale Technology*. PhD thesis, Ghent University, Ghent, Belgium, 2004.

[30] G. Priem. *Nonlinear behaviour in nanophotonic waveguides and resonators for Ultrafast Signal Processing*. PhD thesis, Ghent University, Ghent, Belgium, 2004.

[31] http://www.photond.com/products/fimmwave.htm.

[32] V.R. Almeida, Q.F. Xu, C.A. Barrios, and M. Lipson. Guiding and confining light in void nanostructure. *Optics Letters*, 29(11):1209–1211, 2004.

[33] G. S. Wiederhecker, C. M. B. Cordeiro, F. Couny, F. Benabid, S. A. Maier, J. C. Knight, C. H. B. Cruz, and H. L. Fragnito. Field enhancement within an optical fibre with a subwavelength air core. *Nature Photonics*, 1(2):115–118, 2007.

[34] D. Vermeulen, K. Van Acoleyen, S. Gosh, De Cort W.A.D. Selvaraja, S. K., A.D. Yebo, Hallynck E., K. De Vos, P.P.P. De Backere, P. Dumon, W. Bogaerts, G. Roelkens, P. Dumon, Dries Van Thourhout, and Baets R. Efficient tapering to the fundamental Quasi-TM mode in Asymmetrical Waveguides. pages 1000–1001, 2010. ECIO, Cambridge, UK, APRIL, 2010.

[35] W. H. P. Pernice, M. Li, and H. X. Tang. Optomechanical coupling in photonic crystal supported nanomechanical waveguides. *Optics Express*, 17(15):12424–12432, 2009.

[36] M. Li, W. H. P. Pernice, C. Xiong, T. Baehr-Jones, M. Hochberg, and H. X. Tang. Harnessing optical forces in integrated photonic circuits. *Nature*, 456(7221):480–486, 2008.

[37] B.E. Little, J.-P. Laine, and S.T. Chu. Surface-roughness-induced contradirectional coupling in ring and disk resonators. *Optics Letters*, 22(1):4–6.

[38] S.K. Selvaraja. *Wafer scale fabrication technology for silicon photonic integrated circuits*. PhD thesis, Ghent University, Ghent, Belgium, 2010.

[39] J. Blasco and C.B. Barrios. Compact slot-waveguide/channel-waveguide mode-converter. pages 607–607, 2005. Proc. CLEO/Eur, 2005.

[40] M. Eichenfield, Ryan M. Camacho, J. Chan, Kerry J. Vahala, and O. Painter. A picogram- and nanometre-scale photonic-crystal optomechanical cavity. *Nature*, 459(7246):550–U79, 2009.

[41] M. Eichenfield, J. Chan, Ryan M. Camacho, Kerry J. Vahala, and O. Painter. Optomechanical crystals. *Nature*, 462(7269):78–82, 2009.

[42] J. Rosenberg, Q. Lin, and O. Painter. Static and dynamic wavelength routing via the gradient optical force. *Nature Photonics*, 3(8):478–483, 2009.

[43] G. Anetsberger, O. Arcizet, Q. P. Unterreithmeier, R. Riviere, A. Schliesser, E. M. Weig, J. P. Kotthaus, and T. J. Kippenberg. Near-field cavity optomechanics with nanomechanical oscillators. *Nature Physics*, 5(12):909–914, 2009.

[44] J. Roels, I. De Vlaminck, L. Lagae, B. Maes, D. Van Thourhout, and R. Baets. Tunable optical forces between nanophotonic waveguides. *Nature Nanotechnology*, 4(8):510–513, 2009.

[45] E. Säckinger. *Broadband circuits for optical fiber communication*, chapter 3.

5 Optical forces

He beheld his own image, and it was no longer the reflection of a clumsy, dirty, gray bird, ugly and offensive. He himself was a swan!
Hans Christian Andersen

5.1 Introduction to the chapter

5.1.1 Chapter outline

IN section 4.3 of chapter 4 we discussed several state-of-the art motion transducers (capacitive, magnetomotive, piezo-electric,...). We noted that often these sensing schemes can be reversed, so that efficient motion transduction corresponds with actuation capability. In sections 4.4, 4.5 and 4.6 we discussed intensively some integrated optical waveguide transducers. Unavoidably the question rises whether also in this case the sensing scheme can be reversed and actuation through optical forces is feasible. This way integrated Nano-ElectroMechanical Systems (NEMS) in fact evolve into Nano-OptoMechanical Systems (NOMS) (see chapter 1 for a thorough discussion). In this chapter we first introduce the Maxwell stress tensor formalism, a general formalism which allows to calculate the force exerted on an object for a given electromagnetic field distribution. After this general treatment we focus on forces in waveguides which can be described in a much more elegant way when we think in terms of guided

modes of the waveguide structure. It will turn out that knowledge of the effective index n_{eff} of a guided mode in function of a displacement coordinate g is in fact sufficient to calculate the force exerted by this mode when carrying a certain amount of optical power. One of the main results of this work is the experimental demonstration of optical forces in integrated nanophotonic waveguides. The set-up that was used for this purpose is also described in this chapter. Finally we will also discuss several optical actuation experiments in various configurations.

5.1.2 A little bit of history

The idea that light can be responsible for mechanical effects is quite old. Already at the start of the 17th century Johannes Kepler noticed the deflection of the tails of comets entering our solar system and suggested that solar radiation might be responsible for it. In fact we know now that it is rather the solar wind (stream of mass carrying particles such as protons and electrons) that causes this deflection, rather than pure radiation pressure from the sun light.

Almost two-and-a-half centuries later (1873) it was Maxwell who showed with his classical electrodynamics theory [1] that radiation carries momentum with it and 'radiation pressure' is exerted on an illuminated object. A few years later Adolfo Bartoli also derived the concept of radiation pressure from thermodynamical considerations [2]. The first experimental demonstrations of radiation pressure in a lab followed around 1900 by Lebedev [3] and Nichols [4] by measuring the rotation of an illuminated torsion balance. Shortly thereafter Einstein introduced the concept of a photon and the idea that energy transfer between light and matter occurs in discrete quanta [5]. Hence also the idea of photons carrying momentum was introduced. Discrete momentum transfer between photons and particles (electrons) was experimentally demonstrated by Compton [6].

Even up to day there is actually great controversy about the momentum of a photon in a medium. According to the Minkowski interpretation the photon momentum is multiplied (compared to the non-ambiguous photon impulse in vacuum) with the refractive index of the medium. The Abraham formulation states that the photon momentum is actually divided by the refractive index of the medium. Experimental proof supporting both theories exists. Recently it was proposed that probably both theories are correct, it depends on the experiment itself which momentum is actually measured. A detailed analysis of the Abraham-Minkowski dilemma is far beyond the scope of this thesis. We redirect the interested reader to [7] and the references therein.

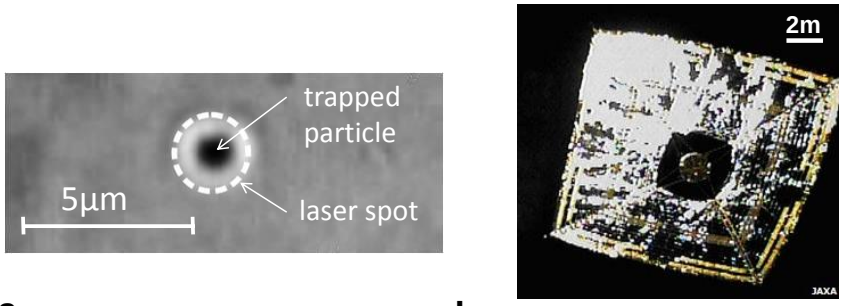

Figure 5.1: **Application examples related to optical forces. a**, Microparticle trapped in a laser beam waist. **b**, Photograph of the IKAROS spacecraft (with solar sail propulsion), illuminated by the Sun.

Also worth mentioning is the possibility to cool objects through interaction with electromagnetic fields [8]. Roughly spoken the idea is to counteract the thermal motion of atoms through radiation pressure effects. The technique has led to ultralow temperatures (order nK) and consequently observation of Bose-Einstein condensates [9]. In fact also mechanical oscillator vibrational modes can be cooled through interaction with light, we will come back to this idea in chapter 6 on feedback cooling.

It is clear from the above that light matter interactions have been (and still are) of extreme importance for a better understanding of fundamental physics. However at the application side probably the most disruptive achievement in the field op optical forces has been the development of 'optical tweezers' which started in the seventies [10, 11]. Optical laser power on the order of a few mW produces sufficiently large forces to trap a particle (including living cells, DNA, bacteria with sub-μm size to a few μm) in the center of a laser beam waist and manipulate it. In Fig. 5.1a we show a microparticle which is trapped in the center of a laser beam waist. We will later on in this chapter explain why the particle actually stays trapped in the region with largest intensity and make an important parallel with optical forces in nanophotonic waveguides.

On the other hand radiation pressure effects can also be applied at a totally different scale. The Russian space engineer Friedrich Zander already proposed around 1924 to use solar sails for spacecraft propulsion (the actual 'photonic' radiation pressure is exploited here and not the much weaker solar wind, although currently experiments are undertaken to exploit the solar wind for propulsion also). However the technical hurdles to be overcome remain challenging, even up to this day. The first successful radiation pres-

sure driven spacecraft IKAROS [12] (Interplanetary Kite-craft Accelerated by Radiation Of the Sun) was launched only very recently (May 2010) by the Japanese Aerospace eXploration Agency (JAXA). Since solar radiation pressure effects are small (around $4.57\,\mu N\,m^{-2}$ at Earth distance from the Sun, this value should be doubled when the light is totally reflected instead of absorbed) a large area ($200\,m^2$), low mass sail ($7.5\,\mu m$ thick polyimide) is required to get significant acceleration (Fig. 5.1b). Although the spacecraft and the optical tweezers are very different applications we can describe the optical force effect for both by the same classical formalism. The Maxwell stress tensor formalism will be introduced in the next section for it can also be used to calculate optical forces in integrated structures.

5.2 Maxwell Stress Tensor

The goal of this section is to derive a formula for the exerted force onto an object by a given electromagnetic field. This derivation can to a large extent be considered as a reproduction of classical electrodynamics concepts. The starting point for our analysis is the well known Lorentz force law:

$$\mathbf{F} = q[\mathbf{E} + \mathbf{v} \times \mathbf{B}] \tag{5.1}$$

In this equation **F** is a force, **E** is the electric field, **v** is the velocity (of a single charge q) and **B** is the magnetic induction. **F**, **E**, **v** and **B** are printed in bold because they denote vectorial quantities. We assume implicitly that these quantities are function of a time coordinate t and a position vector **r**, so **F** is in fact the force exerted by the electromagnetic fields at a time t on an elementary charge q at a position **r**, moving with a velocity **v**.

In the end we will have to deal with macroscopic objects rather than single charges so it is useful to rewrite the Lorentz force law equation in terms of a charge density $\rho(\mathbf{r}, t)$ ($C\,m^{-3}$) and a current density $\mathbf{J}(\mathbf{r}, t)$ ($A\,m^{-2}$):

$$\mathbf{f} = \rho[\mathbf{E} + \mathbf{J} \times \mathbf{B}] \tag{5.2}$$

f is the force per unit volume exerted by the electromagnetic fields. Our goal is to get rid of ρ and **J** in the above equation and to substitute them with expressions that only contain the electromagnetic fields. If we manage to achieve this, then we can in principle calculate the optically induced force per unit volume for any electromagnetic problem with only knowledge of the electromagnetic fields.

We can eliminate ρ and **J** using Maxwell's equations:

$$\nabla \times \mathbf{E} = -\frac{\partial \mathbf{B}}{\partial t} \tag{5.3}$$

$$\nabla \times \mathbf{B} = \frac{1}{c^2}\frac{\partial \mathbf{E}}{\partial t} + \mu_0 \mathbf{J} \tag{5.4}$$

$$\nabla \cdot \mathbf{E} = \frac{\rho}{\epsilon_0} \tag{5.5}$$

$$\nabla \cdot \mathbf{B} = 0 \tag{5.6}$$

In these equations we have introduced the vacuum permittivity ϵ_0 and vacuum permeability μ_0. We will for now use Maxwell's equations in vacuum, the theory can be easily extended by introducing a relative permittivity and permeability that take into account the material properties. Using Gauss's law (equation 5.5) we can easily remove the charge density ρ from equation 5.2. The current density **J** can be substituted using Ampère's law (equation 5.4). Using also the relation $\epsilon_0 = \frac{1}{\mu_0 c^2}$ we can rewrite equation 5.2:

$$\mathbf{f} = \epsilon_0(\nabla \cdot \mathbf{E})\mathbf{E} + (\frac{1}{\mu_0}\nabla \times \mathbf{B} - \epsilon_0\frac{\partial \mathbf{E}}{\partial t}) \times \mathbf{B} \tag{5.7}$$

We now focus on $\frac{\partial \mathbf{E}}{\partial t} \times \mathbf{B}$. Using the product rule for derivatives

$$\frac{\partial(\mathbf{E} \times \mathbf{B})}{\partial t} = \mathbf{E} \times \frac{\partial \mathbf{B}}{\partial t} + \frac{\partial \mathbf{E}}{\partial t} \times \mathbf{B} \tag{5.8}$$

and substituting $\frac{\partial \mathbf{B}}{\partial t}$ using Faraday's law (equation 5.3) we obtain:

$$\frac{\partial \mathbf{E}}{\partial t} \times \mathbf{B} = \frac{\partial(\mathbf{E} \times \mathbf{B})}{\partial t} + \mathbf{E} \times (\nabla \times \mathbf{E}) \tag{5.9}$$

Substituting this equation into 5.7 we obtain:

$$\mathbf{f} = \epsilon_0(\nabla \cdot \mathbf{E})\mathbf{E} + \frac{1}{\mu_0}(\nabla \times \mathbf{B}) \times \mathbf{B} - \epsilon_0 \mathbf{E} \times (\nabla \times \mathbf{E}) - \mu_0\epsilon_0\frac{\partial \mathbf{S}}{\partial t} \tag{5.10}$$

We have introduced the Poynting vector $\mathbf{S} = \frac{1}{\mu_0}\mathbf{E} \times \mathbf{B}$ in this equation. The Poynting vector can be thought of as representing the energy flux of the electromagnetic radiation. Due to our manipulations the time derivative only operates on this vector.
We can further simplify our expression by eliminating the curl ($\times$) vector products for both **E** and **B** through following identity:

$$(\nabla \times \mathbf{E}) \times \mathbf{E} = (\mathbf{E} \cdot \nabla)\mathbf{E} - \frac{1}{2}\nabla E^2 \tag{5.11}$$

In this formula $E^2 = E_x^2 + E_y^2 + E_z^2$ is the total electric field strength. We can rewrite equation 5.10:

$$\mathbf{f} = \epsilon_0[\mathbf{E}(\nabla \cdot \mathbf{E}) + (\mathbf{E} \cdot \nabla)\mathbf{E}] + \frac{1}{\mu_0}[\mathbf{B}(\nabla \cdot \mathbf{B}) + (\mathbf{B} \cdot \nabla)\mathbf{B}] \tag{5.12}$$

$$- \nabla(\frac{\epsilon_0}{2}E^2 + \frac{1}{2\mu_0}B^2) - \frac{1}{c^2}\frac{\partial \mathbf{S}}{\partial t} \tag{5.13}$$

In this equation we have also inserted an extra term $\frac{\mathbf{B}}{\mu_0}(\nabla \cdot \mathbf{B})$. We can do this because this term is zero anyway (equation 5.6). However we added this term to obtain a certain symmetry. By consequence we can see now that the expressions between square brackets in equation 5.13 can be rewritten in a more elegant way using the outer product notation $\otimes$:

$$\mathbf{f} = \nabla \cdot [\epsilon_0 \mathbf{E} \otimes \mathbf{E} + \frac{1}{\mu_0}\mathbf{B} \otimes \mathbf{B} + (\frac{\epsilon_0}{2}E^2 + \frac{1}{2\mu_0}B^2)\bar{\bar{\mathbf{I}}}] - \frac{1}{c^2}\frac{\partial \mathbf{S}}{\partial t} \tag{5.14}$$

We have introduced the unit tensor $\bar{\bar{\mathbf{I}}}$ in this equation. The quantity in square brackets is the Maxwell stress tensor $\bar{\bar{\mathbf{T}}}$ in vacuum. In fact the Maxwell stress tensor is just an artificially created tensor that is introduced to enable a compact notation of the complicated expression that we achieved by eliminating ρ and $\mathbf{J}$ from the right hand side of equation 5.2. In cartesian coordinates it reads as:

$$\bar{\bar{\mathbf{T}}} = \epsilon_0 \begin{bmatrix} E_x^2 - \frac{E^2}{2} + \frac{B_x^2 - \frac{B^2}{2}}{\epsilon_0\mu_0} & E_xE_y + \frac{B_xB_y}{\epsilon_0\mu_0} & E_xE_z + \frac{B_xB_z}{\epsilon_0\mu_0} \\ E_xE_y + \frac{B_xB_y}{\epsilon_0\mu_0} & E_y^2 - \frac{E^2}{2} + \frac{B_y^2 - \frac{B^2}{2}}{\epsilon_0\mu_0} & E_yE_z + \frac{B_yB_z}{\epsilon_0\mu_0} \\ E_xE_z + \frac{B_xB_z}{\epsilon_0\mu_0} & E_yE_z + \frac{B_yB_z}{\epsilon_0\mu_0} & (E_z^2 - \frac{E^2}{2}) + \frac{B_z^2 - \frac{B^2}{2}}{\epsilon_0\mu_0} \end{bmatrix} \tag{5.15}$$

Till now we have only considered the force per unit volume. We need to integrate over an arbitrary volume V in which ρ and $\mathbf{J}$ are located:

$$\mathbf{F} = \int_V \nabla \cdot \bar{\bar{\mathbf{T}}} \mathrm{d}V - \int_V \frac{1}{c^2}\frac{\partial \mathbf{S}}{\partial t}\mathrm{d}V \tag{5.16}$$

This expression is also known as the conservation law for linear momentum [13]. This is because $\mathbf{F}$ and $\int_V \frac{1}{c^2}\frac{\partial \mathbf{S}}{\partial t}\mathrm{d}V$ can be interpreted as the time derivative for the mechanical momentum and field momentum respectively. The volume integral involving the Maxwell tensor can be transformed into a surface integral using Gauss's integration law:

$$\int_V \nabla \cdot \bar{\bar{\mathbf{T}}} \mathrm{d}V = \int_{\partial V} \bar{\bar{\mathbf{T}}} \cdot \mathbf{n} \mathrm{d}A \tag{5.17}$$

n is the unit vector perpendicular to the surface and $\mathrm{d}A$ is an infinitesimal surface element. Finally we note that the fast varying field momentum is zero when averaged over one oscillation period and by consequence the term $\int_V \frac{1}{c^2}\frac{\partial \mathbf{S}}{\partial t}\mathrm{d}V$ can be omitted when considering the time averaged force so we obtain ($<>$ denotes a time average):

$$< \mathbf{F} >= \int_{\partial V} < \bar{\bar{\mathbf{T}}} > \cdot \mathbf{n} \mathrm{d}A \tag{5.18}$$

It is remarkable that the exact material properties of the body under investigation do not enter equation 5.18. We only need to know the fields on a surface ∂V that encloses the body to calculate the electromagnetic force that acts on it, so in most cases we are able to deal with the Maxwell stress tensor in vacuum. In case the surrounding surface is located in a medium that can be accurately enough described by a relative dielectric constant ϵ_r and magnetic permeability μ_r then we can still calculate the force using equation 5.18 when replacing the Maxwell stress tensor in vacuum with a more general expression:

$$\bar{\bar{\mathbf{T}}} = [\epsilon_0 \epsilon_r \mathbf{E} \otimes \mathbf{E} + \frac{1}{\mu_0 \mu_r}\mathbf{B} \otimes \mathbf{B} + (\frac{\epsilon_0 \epsilon_r}{2}E^2 + \frac{1}{2\mu_0 \mu_r}B^2)\bar{\bar{\mathbf{I}}}] \tag{5.19}$$

Strictly spoken the above is only valid for perfectly rigid bodies. Otherwise electrostrictive and magnetostrictive effects have to be taken into account [14].

Summarizing this section we have reviewed the Maxwell stress tensor formalism. With this formalism we can calculate the electromagnetic force that is exerted on a body that is lying within a volume V that is enclosed by a surface ∂V. The power of the proposed formalism is its wide applicability: knowledge of the fields on an enclosing surface in principle suffices to calculate the force of any type of illuminated body. On the drawback side the formalism is rather cumbersome and does not provide much physical insight. In the next section we will see that much more transparent semi-analytical formulas can be obtained for forces acting on waveguide structures. The Maxwell stress tensor formalism is still useful in this case to check the validity of the proposed models.

5.3 Optical forces in waveguides

In this section we introduce optical gradient forces through the example of optical tweezing and make the bridge with gradient forces in optical waveguides. Intuitive explanations for forces in optical waveguides are provided.

Finally we review the theory of optical waveguides and derive a compact force formula for waveguide modes. In constrast with the previous section the theory that is introduced in this chapter is mainly derived from very recent literature.

5.3.1 Microparticle in a gradient field

Before analyzing forces in waveguides it is instructive to take a look into the case of a microparticle in an optical trap. We skip the full derivation (it can be found elsewhere [13]) and directly proceed to the final result. The force acting on a polarizable microparticle (dimensions $\ll \lambda$) is given by:

$$< \mathbf{F}_{trap} >= \frac{\Re(\alpha)}{2} \nabla \left\langle |\mathbf{E}|^2 \right\rangle + \omega \Im(\alpha) \left\langle \mathbf{E} \times \mathbf{B} \right\rangle \tag{5.20}$$

In this equation α is the complex polarizability of the microparticle ($\alpha(\lambda)\mathbf{E} = \mathbf{p}$) which connects the electric field to the induced dipole moment $\mathbf{p}$, ω is the frequency of the illuminating (monochromatic) laser. The first term at the right hand side of the equation is the gradient force, it shows that the particle will be driven along the gradient of $\left\langle |\mathbf{E}| \right\rangle^2$ towards the region with highest intensity (in all three dimensions), explaining the trapping effect. The second term is the scattering force which acts in the light propagation direction. It can be regarded as a consequence of momentum transfer from the radiation field to the particle. The scattering force is responsible for pushing the particle out of the trap when the laser beam is not tightly focused enough. In the next section we will explain how optical trapping of microparticles is related to optical forces in waveguides.

5.3.2 Intuitive explanations for the optical gradient force

Equation 5.20 also illustrates the importance of the polarizability. Indeed the external field induces dipoles in the material. Knowing that dipoles in a non-homogeneous (=gradient) field experience a net force (see Fig. 5.2a) we have an intuitive explanation for optical forces in waveguides. A waveguide supporting a guided wave can be seen as a collection of dipolar subunits. The net force on the waveguide can then be seen as the resultant of the forces exerted on the subunits (see Fig. 5.2b).

Another way of understanding the optical force is thinking in terms of impulse. We can think of a propagating wave inside a waveguide as photons being reflected at the top and bottom of the waveguide, exerting impulse with each reflection. When there are exactly as many photons at the top and bottom at the waveguide the impulses cancel out and no net force is exerted on the waveguide. This is shown in Fig. 5.3.

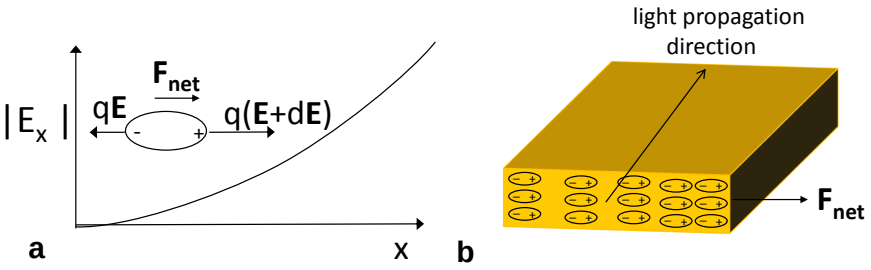

Figure 5.2: **Gradient dipole force. a**, Dipole in a non-homogeneous field. The dipole experiences a net force towards higher field intensities because the charges 'see' a different electric field. **b**, The dipole model can also be used to explain waveguide force if we consider the waveguide as a collection of dipolar subunits.

The field profile changes drastically when a SiO_2 substrate is added to the simulation at a distance of $100\,nm$ of the waveguide 5.4a. The light is much more concentrated around the bottom of the waveguide. We can interpret this as more photons bumping into the bottom edge, compared to the top edge (see Fig. 5.4b). As a consequence an impulse imbalance exists and a net force (towards the substrate) is exerted onto the waveguide. Although the 'impulse' interpretation is limited in providing accurate explanations, it provides an intuitively accessible view into optical forces.

In general a very instructive intuitive insight is to understand that the waveguide material always tends to move into regions with high field intensities (similar to a microparticle in a trap). In Fig. 5.4a we can clearly see that the highest field intensity can be found in the gap between the waveguide and the substrate, so the waveguide will indeed be pushed downward very strongly in this case.

Of course qualitative insights in the origin of the optical gradient force are useful, but we also need to quantify the force. For this purpose the Maxwell stress tensor can be used. However in the next subsection we will show that for the specific case of waveguides a semi-analytical formula can be obtained.

5.3.3 Optical force formula for waveguides

Assume we have a closed (meaning that there is no exchange of energy with the outside world) photonic system of which the eigenfrequencies depend on a spatial coordinate g. In order to focus our thoughts consider a concrete

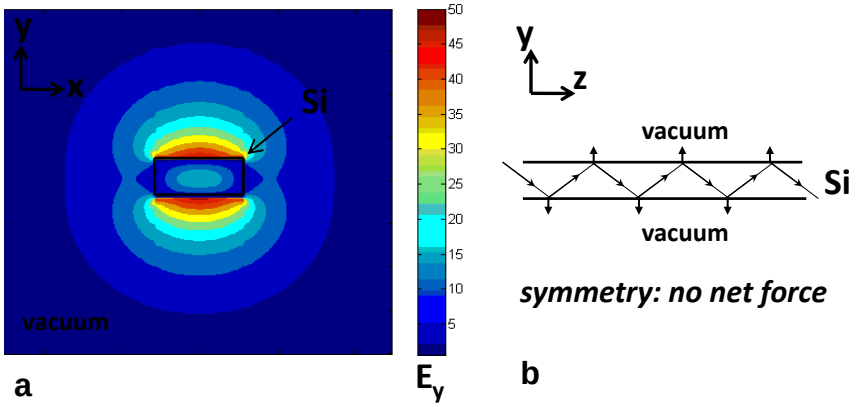

Figure 5.3: **Optical force impulse model for a waveguide in vacuum. a**, Field profile (E_y, see indicated axes) for the fundamental TM mode of a single-mode waveguide (width=450 nm, height=220 nm). **b**, Side view of the waveguide in Fig. 5.3a. We can think of a propagating wave as photons exerting impulse on the top and bottom of the waveguide. Due to the symmetry the impulse contributions cancel out and no net force is exerted on the waveguide.

example: assume we have a lossless FP-resonator with mirror reflectivity $100\,\%$ and g is the mirror separation. This structure only supports eigenfrequencies that interfere constructively after a cavity roundtrip. Assume that $\omega_0(g)$ is such an eigenfrequency of the cavity and N photons populate this eigenfrequency. The energy of the system can then be written as:

$$U = N\hbar\omega_0 \tag{5.21}$$

When changing the separation between the mirrors conservation of energy is required. The mechanical work done to displace the mirrors must be compensated by a change in the electromagnetic energy of the system. By consequence the total energy U of the system must remain the same when the mirror separation is changed over a small distance $\mathrm{d}g$:

$$\mathrm{d}U = 0 = N\hbar\mathrm{d}\omega_0 + F\mathrm{d}g \tag{5.22}$$

We have implicitly assumed that the number of photons is conserved $\mathrm{d}N = 0$ when changing the mirror separation so finally the shift in mirror separation $\mathrm{d}g$ must be compensated by a shift of the eigenfrequency $\mathrm{d}\omega_0$. Solving for F we find:

$$F = \frac{-U}{\omega_0}\frac{\mathrm{d}\omega_0}{\mathrm{d}g} \tag{5.23}$$

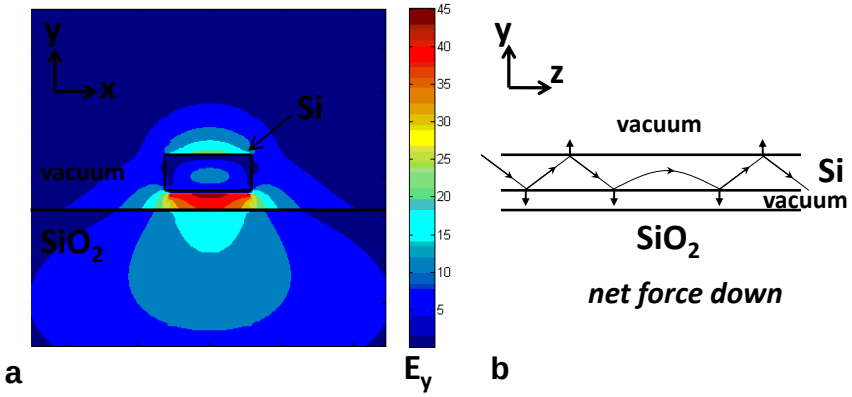

Figure 5.4: **Optical force impulse model for a waveguide with substrate. a**, Field profile (E_y, see the defined axes) for the fundamental TM mode of single-mode waveguide (width=450 nm, height=220 nm, gap to substrate=100 nm). **b**, Side view of the waveguide in Fig. 5.4a. We can think of a propagating wave as photons exerting impulse on the top and bottom of the waveguide. Due to the close presence of the the SiO_2 substrate the field distribution is not symmetric anymore. There are more photons at the bottom of the waveguide compared to the top. The imbalance leads to a net force towards the substrate.

In fact the closed system we proposed can easily be mapped onto the structure we are really interested in: a perfect resonator with periodic boundary conditions (which implies that the wavevector **k** is conserved) resembles a waveguide very much. We only need to mimic electromagnetic energy density in a waveguide through proper choice of the photon number N in our closed system. The number of photons N carried by an eigenmode with eigenfrequency ω and optical power P in a waveguide of length L is equal to [15]:

$$N = \frac{P}{\hbar\omega}\frac{Ln_g}{c} \tag{5.24}$$

In this equation we have also introduced the speed of light c (in vacuum) and the mode group index $n_g = n_{eff} - \lambda\frac{\mathrm{d}n_{eff}}{\mathrm{d}\lambda}$. Combining equations 5.23 and 5.24 we can express the optical force in terms of L, P and waveguide mode parameters:

$$F = \frac{-PLn_g}{\omega c}\frac{\mathrm{d}\omega}{\mathrm{d}g}|_k \tag{5.25}$$

We remind the reader that the derivative is evaluated at fixed k. The formula was first derived in this form [16]. From the formula it is also clear that attractive and repulsive force can be obtained depending on the sign of $\frac{\mathrm{d}\omega}{\mathrm{d}g}$. The idea of having attractive and repulsive optical forces was also proposed by other authors [17, 18].

However it is useful to express equation 5.25 in terms of the effective index of the waveguide mode because this will facilitate comparison with the results obtained in the previous chapter (on small displacement sensing). For this purpose we use the triple product rule. It states that if three variables obey $f(g, k, \omega) = 0$ (where $k = |\mathbf{k}| = \frac{2\pi}{\lambda}n_{eff}$) then the following must hold:

$$-1 = \frac{\mathrm{d}k}{\mathrm{d}g}|_\omega\frac{\mathrm{d}g}{\mathrm{d}\omega}|_k\frac{\mathrm{d}\omega}{\mathrm{d}k}|_g \tag{5.26}$$

Taking into account the definition of group velocity $\frac{c}{n_g} = \frac{\mathrm{d}\omega}{\mathrm{d}k}$ and $\frac{\omega}{c} = \frac{2\pi}{\lambda}$ we can rewrite equation 5.26:

$$\frac{\mathrm{d}\omega}{\mathrm{d}g}|_k = -\frac{\omega}{n_g}\frac{\mathrm{d}n_{eff}}{\mathrm{d}g}|_\omega \tag{5.27}$$

Substituting equation 5.27 into equation 5.25 yields [15]:

$$F = \frac{PL}{c}\frac{\mathrm{d}n_{eff}}{\mathrm{d}g}|_\omega \tag{5.28}$$

In this formula the derivative is evaluated at fixed ω. It is striking that the optical force per unit length and unit optical power is entirely determined

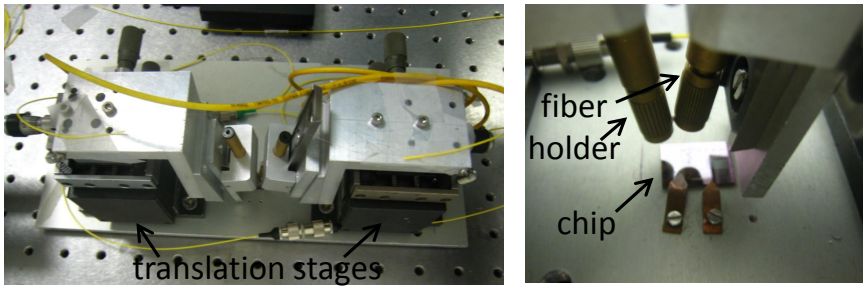

Figure 5.5: **Vertical setup.** **a**, Two fibers can be aligned above a sample using two translation stages. **b**, Silicon chip with aligned fibers. The metal tubes hold the fibers.

by the index sensitivity $\frac{\mathrm{d}n_{eff}}{\mathrm{d}g}$. We have already introduced this parameter to assess the sensitivity of a waveguide configuration in the context of displacement sensing. Similar to the capacitive, magnetomotive and piezoelectric detection and actuation schemes strong optical forces and sensitive displacement sensing are strongly intertwined.

5.4 Pump-probe set-up in vacuum

In the remainder of this chapter we will report on some experiments that demonstrate optical gradient forces in integrated waveguide structures. In fact these experiments can be considered to be the main original contributions to the state-of-the-art in the presented work. First we discuss the set-up that is used for all these experiments. As we have already explained in subsection 3.2.2 light from a fiber is coupled in and out the chip using a grating coupler. The fibers are aligned above the grating couplers using XYZ translation stages. In Fig. 5.5a a photograph is shown of the set-up we have built for this purpose. Essentially it is a miniaturized version of the standard vertical set-ups that are used within the Photonics Research Group. Fig. 5.5b shows the silicon chip with aligned fibers. The metal tubes are fiber holders, they clamp the fibers and hold them on their positions. They are very important because this miniaturized set-up will be placed in a chamber where it is subject to considerable air turbulence when removing the air from the chamber.

The vacuum environment is necessary to obtain high mechanical Q oscillators. In vacuum the major loss mechanism of gas damping is eliminated (see also subsection 2.6.1).

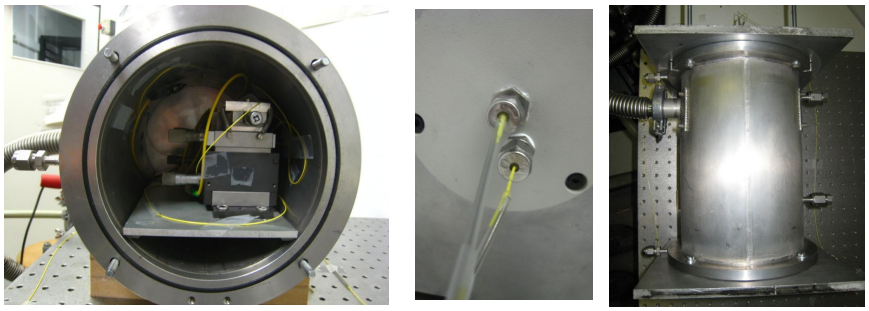

Figure 5.6: **Vacuum chamber. a**, The miniaturized set-up is placed into a vacuum chamber. **b**, Two vacuum feedthroughs for optical fibers are available to bring an optical signal in and out the vacuum chamber. **c**, Top view of the chamber after sealing. At the left the tube which is used to remove the air from the chamber is visible. It is connected to a rotation pump, turbo pump and pressure sensor (not on image).

In Fig. 5.6a we see how the miniaturized setup fits in a vacuum chamber. In order to bring an optical fiber in and out the chamber two special vacuum feedthroughs are foreseen (Fig. 5.6b). Finally in Fig. 5.6c we have a top view of the chamber after it is hermetically sealed with the metal lid. At the left we see the tube that is used to drain air from the chamber. It is connected to a pump group, consisting of a rotation pump and a turbo pump (not on image) and a sensor group (to monitor the pressure inside the chamber). With this system measurements can be done at pressures as low as $10^{-4}\,mBar$. In fact for our structures loss mechanisms other than air damping start to dominate for pressures lower than $1\,mBar$ so we can safely claim that air damping is totally eliminated with this set-up. To demonstrate optical forces typically a pump-probe scheme is applied. This is shown in Fig. 5.7. The pump signal is provided by a tunable laser source (TLS) with wavelength λ_1. The pump signal is power modulated through an electro-optical modulator (EOM). The drive signal for this EOM is typically provided by a sine wave signal generator. The modulated signal is injected into the device-under-test (DUT) which is located in the vacuum chamber. If the modulation frequency of the pump signal is close to a mechanical resonance frequency of the DUT, then the pump signal might induce a detectable vibration of the suspended waveguide structure. This vibration can be detected by means of a CW probe signal with wavelength λ_2. It is typically injected at the other side of the chip. After transmission through the chip the probe signal is separated from the counter propagat-

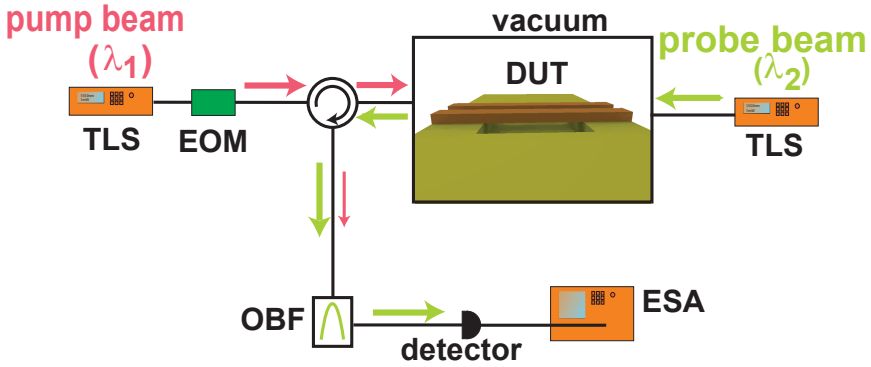

Figure 5.7: **Pump-probe set-up.** The pump signal (λ_1) from a tunable laser source (TLS) is modulated through the electro-optic modulator (EOM) before it is injected in the device-under-test (DUT). The CW probe signal (λ_2) is simultaneously injected from the other side and after transmission through the chip it is separated from the counter propagating pump signal with a circulator. The optical bandpass filter (OBF) ensures that no pump light reaches the detector. The electrical signal from the detector is analyzed with the electrical spectrum analyzer (ESA)

ing pump signal in a circulator. Before it falls onto the detector it passes through an optical bandpass filter (OBF) that ensures the removal of any reflected pump light. The electrical output signal from the detector can be analyzed with an electrical spectrum analyzer (ESA) or oscilloscope. Summarized, if the pump signal is modulated sinusoidally and exerts a force onto the mechanical structure, this structure will respond to this excitation and vibrate at exactly the drive frequency. This vibration is imprinted upon the probe signal so in the end the modulation of the pump signal is 'copied' to the probe signal. However one must make sure that no other mechanism but an optically induced vibration is responsible for this copy. In the next section we will see that other mechanisms than mechanical vibration can cause a pump-probe cross-modulation. In addition we also have to check that the recorded vibration is truly optically induced. It is in principle possible that pure temperature modulation induces vibrations, so we also have to rule out this thermally induced vibration.

5.5 Cross-modulation

In this section we discuss some issues that might jeopardize the unambiguous detection of optical forces: thermo-optical and thermomechanical effects.

5.5.1 Thermo-optical effect through (non-linear) absorption

The modulated optical power from the pump laser will also cause a temperature modulation inside the device. Due to the relatively high thermo-optic effect in silicon ($1.8 \times 10^{-4}/K$) [19] this temperature modulation will also affect the refractive index of the device. A temperature induced refractive index change seems in first instance indistinguishable from a vibration induced refractive index change. Both will be converted into a power modulation by an interferometer or resonator (see section 4.5 on phase sensitivity). However the spectral response is very different. As discussed previously an underdamped harmonic mechanical oscillator exhibits a sharp Lorentzian peak in the frequency domain. On the other hand the temperature response (of the optomechanical transducer) is very similar to a first order low pass band filter: a flat response for DC up to a certain cut-off frequency, above this cut-off frequency the response decays with a factor of 10 per decade. The typical thermal cut-off frequency for the structures considered in this work is around a few $100\,kHz$ while the resonance frequencies are in the MHz region. Hence the temperature response is in general attenuated but not strongly enough to be completely neglected.

However because of the very different spectral response the thermo-optic background can be easily fitted and subtracted from the useful signal. In fact in most cases we can model the decaying thermo-optic response as constant because the frequency spans we consider here are very narrow (due to the relatively large mechanical Q-factors). Although for most of our experiments the thermo-optic effect is order of magnitudes smaller than the mechanical vibration signal, in some circumstances it can dominate the response.

For example for high optical powers in silicon nanophotonic structures non-linear two photon absorption (TPA) and free carrier absorption (FCA) occur [20]. In contrast with the linear regime where absorption (and hence heat generation) is very low, the heat generation increases very strongly through TPA and FCA. The situation is even more dramatic for optomechanical motion transducers that realize a large transduction coefficient $\frac{\mathrm{d}T_x}{\mathrm{d}g}$ through a large phase sensitivity $\frac{\mathrm{d}T_x}{\mathrm{d}\phi}$ (rather than through a large index sensitivity $\frac{\mathrm{d}n_{eff}}{\mathrm{d}g}$, see sections 4.6 and 4.5). In such a transducer also the un-

wanted thermally induced phase shifts are equally enhanced compared to the vibration induced phase shifts. An illustrative example of a structure suffering from a large thermo-optic effect is the ring resonator with free-standing part, which we have previously discussed in subsection 4.6.1. The phase sensitivity is pretty high in this case as it is enhanced by the finesse $\approx$ 100 of the racetrack resonator (see equation 4.29). As can be seen in Fig. 4.15 the probe power that is required to detect the brownian response is already sufficiently high to have a clear thermal bistability due to TPA, so an additional pump signal will suffer from large absorption. Hence it is not possible to present pump probe data for this structure, since the useful signal was covered with thermo-optic noise in spite of the relatively high resonance frequency of $65.86\,MHz$.

Nevertheless we applied the thermo-optic effect also in a useful way, it helped us to distinguish between attractive and repulsive forces between waveguides. However before proceeding to experimental results we will first briefly discuss thermomechanical forces.

5.5.2 Thermomechanical effect

The temperature modulation also gives rises to strain modulation in the material through the thermal expansion coefficient. In fact the mismatch between the thermal expansion coefficient of silicon and silica is responsible for vibration of the beam (TO_{coef,SiO_2} = $0.5\,10^{-6}K^{-1}$ and $TO_{coef,Si}$ = $2.59\,10^{-6}K^{-1}$ at $25°C$ for silicon [21]). In contrast with the thermo-optic effect we have a physical displacement here which makes it hard to separate the thermomechanical effect from an effective optical force since both phenomena will show a Lorentzian response.

However the thermomechanical effect can be modeled through a finite element simulation. At this point we wish to acknowledge Prof. Bjorn Maes for implementing the simulation in software. According to the simulation a displacement of $1.5\,pm\,K^{-1}$ can be expected in-plane for a standard silicon nanophotonic waveguide (of approximately $24\mu m$) resting on silica supports. For out-of-plane displacement $14\,pm\,K^{-1}$ is found which is very close to the value of $11\,pm\,K^{-1}$ that has been reported by other authors for a similar structure [22]. We can conclude that unrealistic temperature shifts would be required to explain the experimentally found displacements (=on the order of nanometers). Finally we will see that also experimental proof is available that the encountered forces are truly electromagnetic in nature. For example repulsive and attractive forces can never be explained through a thermomechanical model.

5.6 Experimental results

5.6.1 Optical force in a directional coupler

We will first discuss the case of an ordinary directional coupler. In Fig. 5.8a a microscope picture of the device is shown. A schematic drawing and SEM-picture of this type of device can be found in the previous chapter (Fig. 4.21). Also in the previous chapter we have analyzed the optomechanical transduction of this device in detail (see subsection 4.6.3).

As announced previously we will restrict ourselves to TE-polarization for practical experiments. Two guided modes are available for this polarization: their mode profiles are shown in Fig. 5.9. As can be seen the ground mode is symmetric in E_x (field component parallel with substrate, see Fig. 5.9 for definition of axes), while the second mode is anti-symmetric in E_x. In fact based on these field profiles we can already make qualitative predictions about the optical force. In case of the symmetric mode (Fig. 5.9a) we observe strong fields in the gap in between the waveguides. Similar to the microparticle the waveguide will be driven towards regions with high intensities so we can expect an attractive force for this mode. The anti-symmetric mode can be seen to have higher fields at the outer boundaries of the waveguides compared to the fields in the gap. In this case the waveguides will be pushed apart and a repulsive force is to be expected. This qualitative insight is confirmed by calculations. The result can be seen in Fig. 5.8b where the normalized force ($pN\,\mu m^{-1}mW^{-1}$) is plotted in function of the gap between the waveguides. We indeed see that the symmetric mode has an exclusively attractive nature (negative force value=attractive force) while the anti-symmetric mode is repulsive for sufficiently large gaps. For very small gaps the anti-symmetric mode shows an attractive force. This behavior is due to edge effects at the top and bottom of the strip waveguides we are considering here. For slab waveguides the anti-symmetric mode conserves its repulsive character, even at very small gaps [23, 24].

The force is normalized for the waveguide length and the optical power carried by the optical mode. The circles are obtained using the 'waveguide force formula' (equation 5.28) while the solid black line is the corresponding calculation using the Maxwell stress tensor (equation 5.18). As can be seen in Fig. 5.8b the match between the two formalisms is perfect. The equivalence of equations 5.28 (semi-analytical force formula) and 5.18 (stress tensor) has also been verified by other authors [15, 16, 22, 25].

However in the case of an ordinary directional coupler such as the one shown in Fig. 5.8a both propagating modes are always excited simultaneously with equal amplitude and hence they are counteracting each other's force. Since the symmetric mode always has a larger amplitude we can

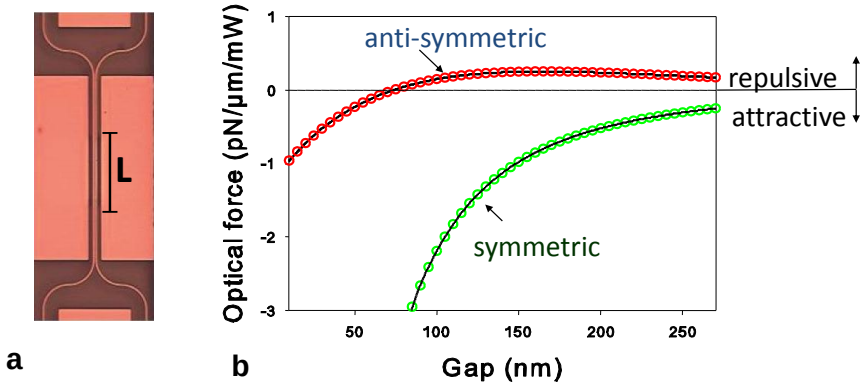

Figure 5.8: **Directional coupler optical force simulation. a**, Microscope picture of a freestanding directional coupler, the freestanding portion is of length L$\approx 24\,\mu m$ **b**, Optical force simulation for the symmetric and anti-symmetric mode (g=220 nm, w=445 nm, t=220 nm). Negative values correspond to attractive forces. Circles are obtained through the semi-analytical formula 5.28. The black solid line is the corresponding calculation with the Maxwell stress tensor formalism (equation 5.18).

only obtain a net attractive force for this structure.

The results of a pump probe experiment are shown in Fig. 5.10. The curves in Fig. 5.10 b were obtained by sweeping the frequency of the signal generator and the electrical spectrum analyzer in parallel. We see that the measured responses increase with increasing pump power as expected. Using the calibration procedure with the brownian force (see subsection 4.2.3) we can estimate the vibration amplitude for each data point and extract the optical force exerted on each of the two waveguides for different pump powers (Fig 5.10a). Forces on the order of pN and amplitudes on the order of nm are obtained.

An important issue concerning this experiment has not been addressed yet. It is not straightforward to simply add the modal contributions to obtain the total force. In practice one might expect a beating force when two propagating modes are present in the structure. In other words a force that varies in the propagation direction of the waveguide can be expected.

The force beating issue is intrinsic to a bimodal system and will be addressed in a specific subsection of this section. We will however first discuss how we can excite the symmetric and anti-symmetric mode individually and by consequence obtain a purely attractive or repulsive force.

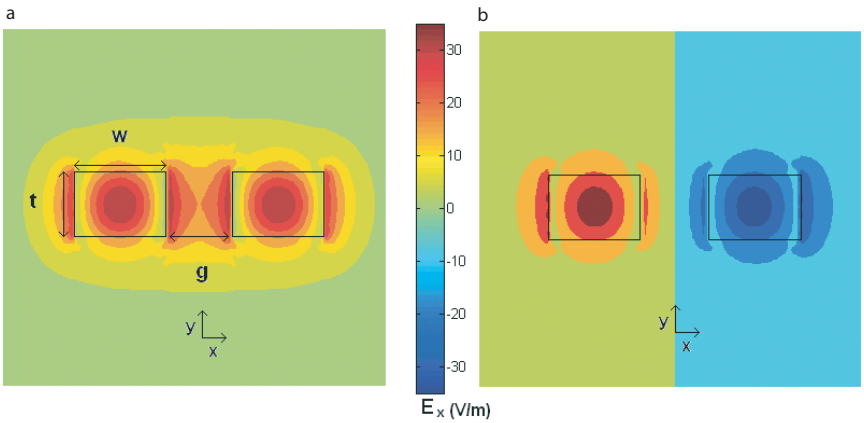

Figure 5.9: **Mode profiles symmetric and anti-symmetric TE modes (g=220 nm, w=400 nm, t=220 nm) a**, E_x mode profile of the symmetric ground mode. **b**, E_x mode profile of the anti-symmetric ground mode.

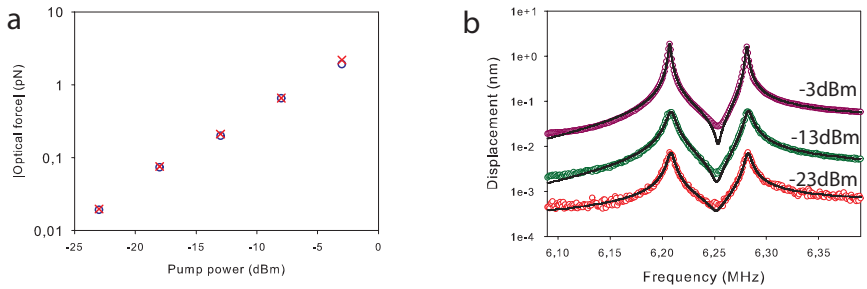

Figure 5.10: **Optical force in a directional coupler (g=220 nm, w=400 nm, t=220 nm) a**, Extracted optical force for different power levels. Blue circles: force exerted on the lower frequency oscillator. Red crosses: force exerted on the higher frequency oscillator. **b**, Measured and fitted vibration amplitudes in function of drive frequency for different pump powers. Black solid lines are fits to equation 2.47.

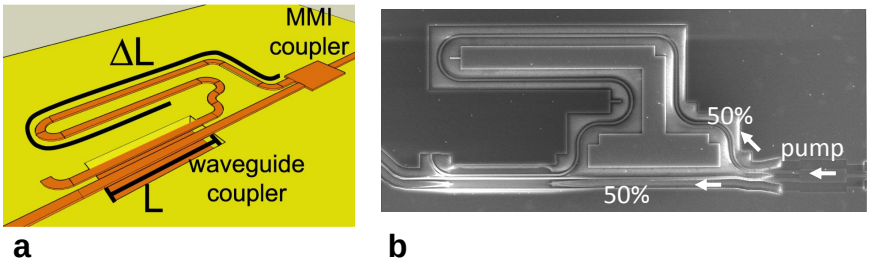

Figure 5.11: **Tunable force device. a**, Schematic drawing. Basically we have a Mach-Zehnder Interferometer (MZI) with arms of unequal length (length difference $\Delta L \approx 113\mu m$). One of the couplers is a standard Multi-Mode-Interferometer (MMI) 3dB-splitter, the other is a freestanding directional coupler. **b**, SEM-picture of the device, showing where the pump power is entering the device and how it is divided in two equal parts. Due to the delay length the phase difference between the fields that arrive at the waveguide coupler section varies with wavelength, hence different mode superpositions can be excited in the coupler section.

5.6.2 Attractive and repulsive force

In order to control the sign of the force we must control the excitation of the two modes in the directional coupler section. This can be done with the structure shown in Fig. 5.11. We have already introduced this device in subsection 4.6.3 where we discussed its motion transduction (see also Fig. 4.25). The freestanding waveguide coupler (length L) acts as one of the couplers in a Mach-Zehnder Interferometer (MZI). The other coupler is an ordinary 3dB-splitter of the Multi-Mode interferometer type (MMI) which splits the pump light into two equal parts. One arm of the MZI is ΔL longer than the other. Because of this delay length the phase difference between the fields that arrive at the waveguide coupler section varies with wavelength. When the fields arrive in phase the symmetric mode will be excited. In case the fields arrive in counter phase the anti-symmetric mode is favored. Hence simply tuning the pump wavelength allows us to sweep from an attractive to a repulsive force and vice versa.

We did a sweep of the drive frequency for a number of wavelengths. The result for two of such sweeps is shown in Fig. 5.12a. The trace with the red (blue) circles is obtained with a pump wavelength $1551.4\,nm$ ($1553.5\,nm$). From the corresponding fits (black solid lines) we can extract an optical force. If we repeat this procedure for a large number of wavelengths and plot the extracted force for each of them, then we obtain

5.12b. In this plot we have already assigned a sign to the measured forces, however in principle we cannot directly detect the force sign from simple amplitude measurements such as the curves shown in Fig. 5.12a. Nevertheless for several wavelengths we measured a zero force (twice in Fig. 5.12b), which strongly suggests that the attractive and repulsive force cancel each other out for these wavelengths. One can of course argue that the force with a magnitude that is approximately twice as large as the other must be the attractive one since this ratio is predicted by theory. The spectral distance between a wavelength that we assume to generate an attractive force and a wavelength that we assume to generate a repulsive force is approximately around $2.1\,nm$. In Fig. 5.13 we have shown the time domain traces for pump wavelengths $1547\,nm$ and $1549\,nm$ taken with an oscilloscope (both relative to the same reference = the signal generator drive signal, not shown in the graph). The fit reveals a phase shift of $169°$, showing that the displacements (in function of time) are almost in counter phase for these pump wavelengths. Phase shift measurements indeed prove that attractive and repulsive forces are obtained but strictly speaking we must still rely on the amplitude argument to determine the force sign.

One technique that allows to measure the force sign directly is to look into the interference with the thermo-optic background. The idea is that the thermo-optic effect acts similar in phase ('phase' is always defined relative to the drive signal) for wavelengths that differ only $2.1\,nm$. However as we have just discussed the displacement signals can be thought of as being in counter phase and by consequence they will interfere differently with the thermo-optic background. Therefore in our fitting model we must add a term P_{TO} which takes into account the thermo-optic background.

$$\frac{P_{mod}}{P_{cw}} = |\frac{F_{opt,AC}}{k}\frac{\mathrm{d}T_x}{\mathrm{d}g}\chi_{mech} + P_{TO}| \tag{5.29}$$

In fact an increase in temperature (=increase in optical power) increases the index contrast through the thermo-optic effect and leads to a decrease in coupling strength. A gap increase is also equivalent to a decrease in coupling strength. A gap increase that comes with an increase in optical power must be attributed to a repulsive force, by consequence the thermo-optic background and a repulsive force signal will interfere constructively. Indeed for the curves shown in Fig. 5.12a the fitted value for P_{TO} is equal in magnitude, but different in sign. For the $1553.5\,nm$ trace we find $\Re(P_{TO}) > 0$, while for the $1551.4\,nm$ trace $\Re(P_{TO}) < 0$. The former corresponds to repulsive, the latter to attractive forces.

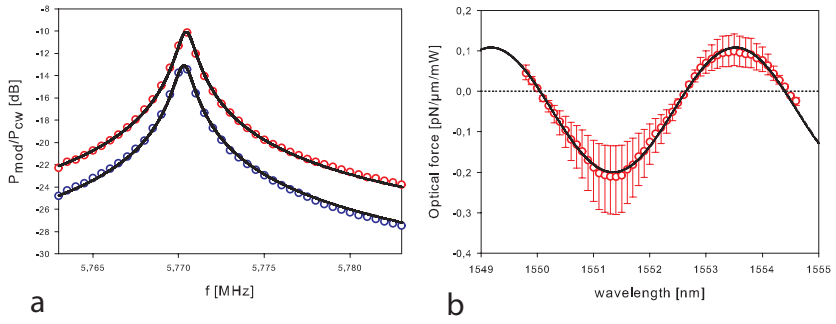

Figure 5.12: **Tunable force experimental results. a**, Measured response for a drive frequency sweep around the mechanical resonance frequency. The trace with the red (blue) circles is obtained with a pump wavelength $1551.4\,nm$ ($1553.5\,nm$). From the corresponding fits (black solid lines) we can extract an optical force magnitude. **b**, Extracted force for different wavelengths. Error bars origin from the uncertainty on the exact optical power level inside the device and its exact temperature.

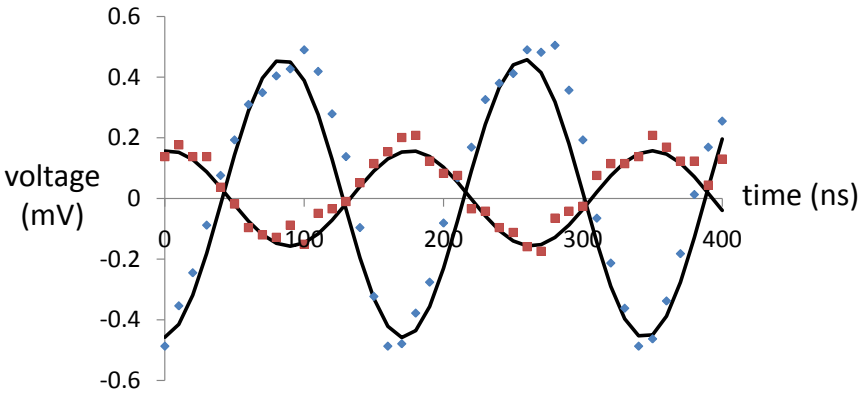

Figure 5.13: **Measured phase shift in the time domain.** Vibration response for wavelengths $1547\,nm$ and $1549\,nm$. The fits reveal a phase shift of $169°$.

5.6.3 Force beating

In a directional coupler the optical power can be thought of as coupling back-and-forth between the waveguides when propagating through the coupler. The coupling happens with a period of $L_{prop,period} = \frac{\lambda}{n^+ - n^-}$. Since the electromagnetic field distribution is also changing along the propagation length we must also investigate how the optical force is varying over this period. These calculations can be done with the Maxwell stress tensor formalism. The result of such a calculation for a parallel waveguide structure (waveguide width $w = 445\,nm$, thickness $t = 220\,nm$, gap $g = 220\,nm$) with a coupling period of approximately $120\,\mu m$ is shown in Fig. 5.14. The pink and blue curves show the force of the pure modes (repulsive and attractive mode respectively). These curves are completely flat because there can be no beating. In the most extreme case (equal excitation of the repulsive and attractive modes) the beating force amplitude is calculated to be 25% of the average optical force for our device (black curve in Fig. 5.14). The red and green curves show mixed mode superpositions with a 5% to 95% distribution of the optical power between the modes. In principle the beating is the most significant (in terms of effect on measurement) for parallel waveguides that are freestanding over a length that is much shorter than the coupling period. In any case in the analysis of our experimental data we are only able to fit the average force that is exerted onto the waveguide. However if the freestanding portion is sufficiently long, then averaging of the beating effect is obtained and the beating will be much less than the worst case 25% and it is acceptable to ignore the beating.

5.6.4 Slot waveguide

We have already introduced the slotted waveguide in subsection 4.6.2 of the previous chapter. Also for this structure we have explored optical actuation. The calculated forces are shown in Fig. 5.15. Similar to the case of the index sensitivity (see Fig. 4.16) we observe a strong enhancement of the optical force in the TE polarization for smaller gaps due to strong field gradients. In fact many of the conclusions made in subsection 4.6.2 can be repeated. Slotted waveguides with small gaps and a field vector that is orthogonal to the gap create the largest forces. In Fig. 5.16a the result for a pump-probe experiment for a slotted waveguide is shown. We obtain nm displacements for only $1\,mW$ power and obtain around $5\,pN\,mW^{-1}\,\mu m^{-1}$ [26]. Interestingly non-linear spring softening is observed. In Fig. 5.16b an experiment for a parallel waveguide pair is shown where non-linear spring hardening is observed. The (be it very rough) model for mechanical spring hardening we have introduced in section 2.7 predicts that (for typical pa-

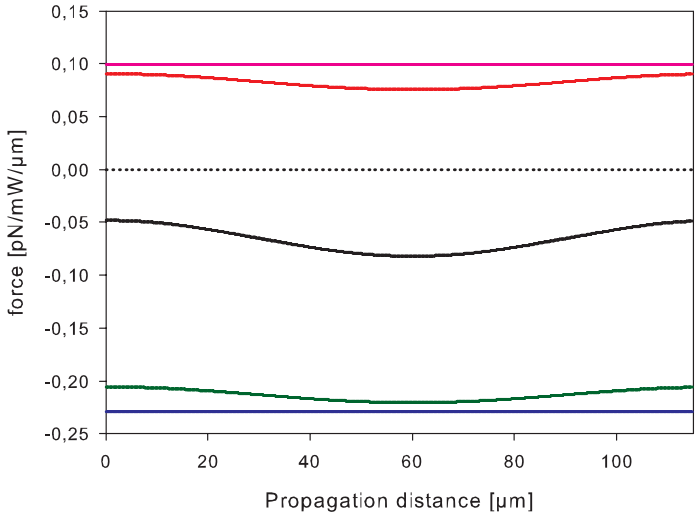

Figure 5.14: **Force beating.** Normalized calculated force ($pN\,mW^{-1}\,\mu m^{-1}$) for different relative mode excitations (anti-symmetric A, symmetric S): pink (100%A), red (95%A, 5%S), black (50%A, 50%S), green (5%A, 95%S), blue (100%S). Forces above (under) dotted line are repulsive (attractive).

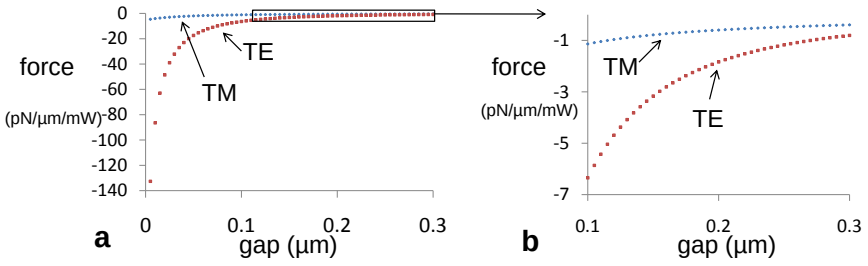

Figure 5.15: **Theoretical force in a slotted waveguide.** **a**, Normalized calculated force ($pN\,mW^{-1}\,\mu m^{-1}$) for a slotted waveguide in function of gap for TE and TM polarizations. **b**, Detail of Fig. 5.15a.

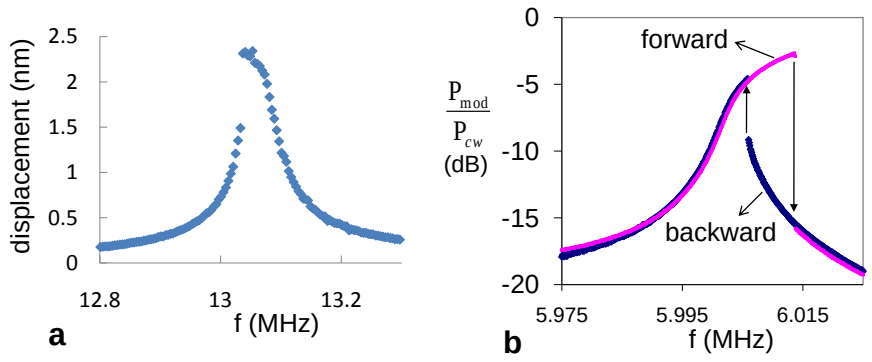

Figure 5.16: **Displacement spectra showing non-linearities. a**, Displacement spectrum in a slotted waveguide with non-linear spring softening. **b**, Forward and backward pump wavelength sweep for a parallel waveguide pair. The observed non-linear spring hardening and corresponding bistability might be caused by mechanical non-linearity.

rameters) bistability can occur for vibration amplitudes $< 10\,nm$ so probably the observed behavior can be explained by this model. The spring softening is much harder to explain. It could be explained through non-linearity in the exerted force. For an attractive force the non-linearity should indeed be of the softening type but the observed non-linearity is too high to match our theoretical calculations. We conclude that more research is required here to explain the observed behavior.

5.7 Chapter summary

We have introduced optical forces and explained the difference between radiation pressure effects (e.g. spacecraft) and gradient optical forces. We have also discussed the Maxwell stress tensor formalism which can be used to simulate various types of electromagnetic forces. For forces in integrated waveguide structures we have derived a semi-analytical formula which suggested a strong correlation between large optical forces and efficient small displacement sensing. Moreover intuitive explanations were provided to explain optical forces.

Furthermore we introduced our pump-probe setup and discussed the difficulties that perturb the transduction scheme (thermo-optic and thermo-mechanical effects). Finally we have demonstrated optical forces in parallel waveguides (attractive and repulsive) and in slotted waveguides.

Bibliography

[1] James C. Maxwell. *Treatise on Electricity and Magnetism*. Clarendon Press, 1873.

[2] A. Bartoli. Il calorico raggiante e il seconde pricipio di termodynamica. *Nuovo Cimento*, 15:196–202, 1876.

[3] Lebedev P. Untersuchungen über die druckkräfte des lichtes. *Annalen der Physik*, 311(11):433–458, 1901.

[4] E. F. Nichols and G. F. Hull. A preliminary communication on the pressure of heat and light radiation. *Phys. Rev. (Series I)*, 13(5):307–320, 1901.

[5] A. Einstein. Über einen die Erzeugung und Verwandlung des Lichtes betreffenden heuristischen Gesichtspunkt. *Annalen der Physik*, 17:132–148, 1905.

[6] Arthur H. Compton. A quantum theory of the scattering of x-rays by light elements. *Physical Review*, 21(5):483–502, 1923.

[7] Stephen M. Barnett and R. Loudon. The enigma of optical momentum in a medium. *Philosophical Transactions of the Royal Society A: Mathematical, Physical and Engineering Sciences*, 368(1914):927–939, 2010.

[8] Arthur H. Compton. Zwei bemerkungen über den unterschied von lumineszenz-und temperaturstrahlung. *Z. Phys.*, 57:739–746, 1929.

[9] M.H. Anderson, J.R. Ensher, M.R. Matthews, C.E. Wieman, and E.A. Cornell. Observation of Bose-Einstein Condensation in a dilute atomic vapor. *Science*, 269(5221):198–201, 1995.

[10] J.P. Gordon and A. Ashkin. Motion of atoms in a radiation trap. *Physical Review A*, 21(5):1606–1617, 1980.

[11] S. Chu. Laser manipulation of atoms and particles. *Science*, 253(5022):861–866, 1991.

[12] http://www.jspec.jaxa.jp/e/activity/ikaros.html.

[13] L. Novotny and Hecht B. *Principles of Nano-Optics*, chapter 14. Cambridge University Press, Cambridge, UK, 2006.

[14] Peter T. Rakich, P. Davids, and Z. Wang. Tailoring optical forces in waveguides through radiation pressure and electrostrictive forces. *Optics Express*, 18(14):14439–14453, 2010.

[15] Peter T. Rakich, Milos A. Popovic, and Z. Wang. General Treatment of Optical Forces and Potentials in Mechanically Variable Photonic Systems. *Optics Express*, 17(20):18116–18135, 2009.

[16] M.L. Povinelli, M. Loncar, M. Ibanescu, E.J. Smythe, S.G. Johnson, F. Capasso, and J.D. Joannopoulos. Evanescent-wave bonding between optical waveguides. *Optics letters*, 30(22):3042–3044, 2005.

[17] A. Mizrahi and L. Schachter. Two-slab all-optical spring. *Optics Letters*, 32(6):692–694, 2007.

[18] A. Mizrahi and L. Schachter. Mirror manipulation by attractive and repulsive forces of guided waves. *Optics Express*, 13(24):9804–9811, 2005.

[19] J. A. McCaulley, V. M. Donnelly, M. Vernon, and I. Taha. Temperature dependence of the near-infrared refractive index of silicon, gallium arsenide, and indium phosphide. *Phys. Rev. B*, 49(11):7408–7417, Mar 1994.

[20] G. Priem. *Nonlinear behaviour in nanophotonic waveguides and resonators for Ultrafast Signal Processing*. PhD thesis, Ghent University, Ghent, Belgium, 2004.

[21] Y. Okada and Y. Tokumaru. Precise determination of lattice-parameter and thermal-expansion coeffcient of silicon between 300-K and 1500-K . *Journal of Applied Physics*, 56(2):314–320, 1984.

[22] M. Li, W. H. P. Pernice, C. Xiong, T. Baehr-Jones, M. Hochberg, and H. X. Tang. Harnessing optical forces in integrated photonic circuits. *Nature*, 456(7221):480–486, 2008.

[23] Dries Van Thourhout and Joris Roels. Optomechanical device actuation through the optical gradient force. *Nature Photonics*, 4(4):211–217, 2010.

[24] F. Riboli, A. Recati, M. Antezza, and I. Carusotto. Radiation induced force between two planar waveguides. *European Physical Journal D*, 46(1):157–164, 2008.

[25] M. Li, W. H. P. Pernice, and H. X. Tang. Tunable bipolar optical interactions between guided lightwaves. *Nature Photonics*, 3(8):464–468, AUG 2009.

[26] J. Roels, B. Maes, D. van Thourhout, and R. Baets. Optical gradient force in a slot waveguide on a Silicon-on-Insulator-Chip. In *2009 IEEE LEOS Annual Meeting Conference Proceddings, Vols 1 and 2*, IEEE Lasers and Electro-Optics Society (LEOS) Annual Meeting, pages 223–224, 2009. 22nd Annual Meeting of the IEEE-Photonics-Society, Belek Antalya, Turkey, OCT 04-08, 2009.

6 Feedback

Doing a Ph.D. is like becoming all of the Seven Dwarves. In the beginning you're Dopey and Bashful. In the middle, you are usually sick of it (Sneezy), tired (Sleepy), and irritable (Grumpy). But at the end, they call you Doc, and then you're Happy.
R.T. Azuma

6.1 Introduction

AS discussed in subsection 1.3.2, optical cooling of micromechanical resonators is of great interest to the scientific community [1, 2]. In general the major incentive is the possibility to cool a micromechanical resonator to its quantummechanical ground state [3] and hence to gain additional insight in the less well understood aspects of quantum mechanics. In the case of optical cooling light is used to extract energy from the resonator and hence to dampen its motion. However it is also possible to reverse this process and amplify the resonator motion through positive optical feedback (sometimes this process is referred to as 'heating' of the mechanical resonator).

When the feedback is sufficiently large regenerative oscillations occur and the resonator acts as an oscillator. In the literature this regime is called 'parametric instability' [1]. Compared to the optical cooling regime, the 'heating' regime has received less attention in the physics community. Nev-

ertheless oscillators might be the shortest route towards a practical application for optomechanics, for example as a reference clock on chip. In the literature this concept is often referred to as 'photonic clock' [4]. When thinking of (mass) sensing applications, especially in aqeous or gaseous environments, micromechanical resonators suffer from very low quality factors (see subsection 2.6.1). This limitation might be overcome by positive feedback, as has been demonstrated with electrical feedback schemes [5, 6]. Both for the sensing and reference applications higher mechanical resonance frequencies are beneficial.

In the next section we explain the difference between active and passive feedback schemes. In the remainder of the chapter we elaborate on the experimental implementation of an optomechanical active feedback experiment. First we select the optomechanical device that fits best our experimental requirements and discuss the full experimental setup. Afterwards we show some experimental results. These results can be considered as a novel and important contribution in the context of this work and optomechanics in general. In particular we focus on the important parameters that govern access to the regime of parametric instability.

6.2 Active vs. passive feedback

Passive cooling or amplification requires the mechanical resonator to be implemented in an optical cavity with extremely high optical Q because the mechanical oscillation period needs to be smaller than the optical cavity lifetime. Expressed in terms of the cavity optical bandwidth $\Delta\omega_{cav}$ and the mechanical resonance frequency ω_{mech} we require $\Delta\omega_{cav} \ll \omega_{mech}$. Under this condition a laser beam with frequency ω_{laser} can cool or amplify the mechanical resonator motion depending on whether the laser light is blue- or red detuned compared to the cavity resonance frequency ω_{cav} (see Fig. 6.1). In fact we can explain the whole process through the Doppler effect where the mechanical oscillator generates two sidebands with frequencies $\omega_{cav} - \omega_{mech}$ (lower frequency sideband) and $\omega_{cav} + \omega_{mech}$ (higher frequency sideband) [1]. The former can be interpreted as absorption of a phonon by a laser photon, the latter as emission of a phonon by the photon. If the laser light is exactly on resonance $\omega_{cav} = \omega_{laser}$ both processes are in equilibrium and the net energy exchange between the mechanical resonator and the light is zero.

However in case the laser light is slightly red-detuned compared to the cavity resonance ($\omega_{cav} > \omega_{laser}$), then the photon frequency upconversion (or phonon absorption) process is resonantly enhanced and the mechanical resonator is cooled (Fig. 6.1a). On the other hand if the laser light

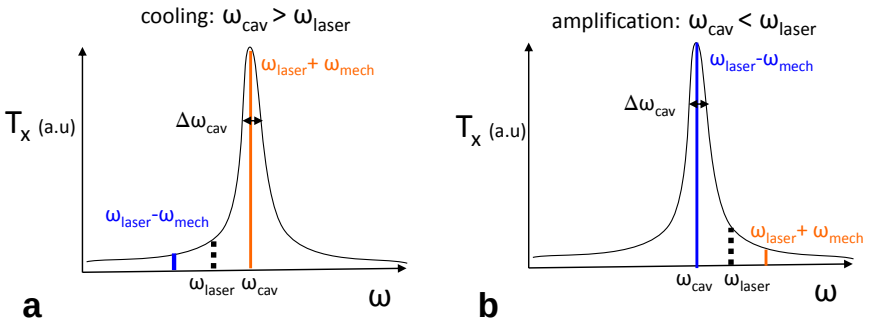

Figure 6.1: **Passive cooling and heating of a mechanical oscillator.** The optical cavity transmission (T) spectrum is shown in function of the optical frequency. Two frequency side-bands to the laser frequency ω_{laser} are created through interaction with the mechanical oscillator: $\omega_{cav} \pm \omega_{mech}$ **a**, The laser is red-detuned ($\omega_{cav} > \omega_{laser}$). The photon upconversion process is resonantly enhanced, hence the mechanical oscillator is cooled. **b**, The laser is blue-detuned ($\omega_{cav} < \omega_{laser}$)). The photon downconversion process is resonantly enhanced, hence the mechanical oscillator is heated.

is slightly blue-detuned compared to the cavity resonance ($\omega_{cav} < \omega_{laser}$) then the photon frequency downconversion (or phonon emission) process is resonantly enhanced. In this case the mechanical resonator is receiving phonons and the motion is amplified (Fig. 6.1b).

From the technological point of view such a high Q is not easy to fabricate, especially if additional boundary conditions apply. For example the resonator might be required to be fully integrated or operate in an aqueous environment. An ultra-high Q also limits the intrinsic optical bandwidth of the system and the high circulating optical powers might result in heating of the cavity material and non-linear effects. Consequently instability of the optical resonance wavelength can be expected through the thermo-optic effect, which is a considerable drawback.

In this chapter we present a system with active feedback that does not include an optical cavity, hence strongly reducing bandwidth, heating and fabrication issues. The feedback force is provided by the optical gradient force that we have thoroughly discussed in chapter 5. In an active feedback system the motion of the mechanical resonator is continuously monitored. Using the recorded signal a feedback force that has a distinct phase relation to the resonator vibration is generated. If we assume the mechanical resonator to be harmonic (with spring constant k, effective mass m and damping constant Γ, $F_{brown}(t)$ is the brownian force), then the system can

be modeled as:

$$kx(t) + \Gamma\dot{x}(t) + m\ddot{x}(t) = F_{brown}(t) + F_{fb,opt}(t) \tag{6.1}$$

The optical feedback force $F_{fb,opt}(t)$ can be thought of as providing an additional damping term $\Gamma_{opt}\dot{x}(t)$ which can be added to or subtracted from the intrinsic damping term at the left hand side of the equation.

6.3 Experimental implementation

An additional advantage of an active feedback scheme is its versatility: in principle it can be implemented with every device that allows a sufficient sensitive motion transduction and generation of a sufficiently strong optical force. Nevertheless we prefer the optomechanical device that allowed us to demonstrate attractive and repulsive forces (see subsection 5.6.2) for practical implementation. In this section we will first comment on this choice and afterwards discuss the full experimental set-up.

6.3.1 Optomechanical device choice

The exact phase relation between the oscillating beam and the feedback force is of crucial importance for controlling the sign of the feedback and switching between the amplifying and damping regimes. Of course this phase relation depends on the delay in the feedback loop, which cannot be altered easily in a flexible way. However the typical mechanical oscillation periods that we encounter in our optomechanical devices are in the range of 100-500 ns so tunable delays on the order of a few hundreds of nanoseconds are required to actively control the phase of the feedback force. The required delay can also be implemented in flexible way by simple wavelength tuning. To achieve this the phase (or sign) of the optical force needs to be tunable. In contrast with the other optomechanical structures we have implemented experimentally (a slot waveguide in a Fabry-Pérot resonator, a single-mode waveguide in ring resonator, an ordinary directional coupler, see section 5.6), this condition is fulfilled for the tunable force device.

To initiate the envisioned self-pulsating behavior a sufficiently strong initial vibration is required to provide the feedback loop with an input signal. The initial vibration is provided by the brownian force, which is known to be relatively weak (see section 4.2). Consequently for better detection of the vibration we require the preamplification technique that we have elaborated on in section 4.7.

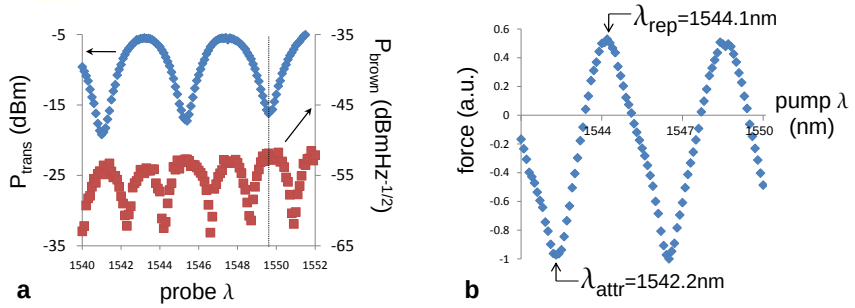

Figure 6.2: **Tunable force device. a**, Transmission spectrum of the tunable force device. Also the transduction spectrum (taken by measuring the brownian mechanical response at different probe wavelengths and no pump signal) is plotted. For the feedback experiments we set the probe wavelength to 1549.5 nm (dashed vertical line). **b**, Measured force when sweeping the pump length. For the feedback experiments we use the purely attractive force (λ_{attr}=1542.2 nm) and the repulsive force (λ_{rep}=1544.1 nm).

The device we use for our feedback experiments is not the same as the one we have introduced in chapters 4 and 5. Consequently we have to characterize the device again in terms of transmission, transduction and optical force response. These results are shown in Fig. 6.2. We also mention that the suspended waveguides have natural mechanical frequencies 5.98 MHz and 6.24 MHz.

6.3.2 Set-up

In Fig. 6.3 the pump-probe set-up with feedback loop is shown. First we note that the preamplification technique was implemented: an EDFA followed by an optical bandpass filter (2.4 nm bandwidth) is placed in front of the detector to amplify the probe signal. The obtained electrical signal is then used to drive an electro-optical modulator, which modulates a pump laser. The generated optical force that acts onto the optomechanical device closes the feedback loop. A delay line is implemented in the feedback loop. In practice the delay line consists of an additional optical fiber that can be varied in length between 0 and 31 m in steps of one meter. The delay of an optical fiber is approximately 5 ns per meter so we can scan a full range of 155 ns with a resolution of 5 ns.

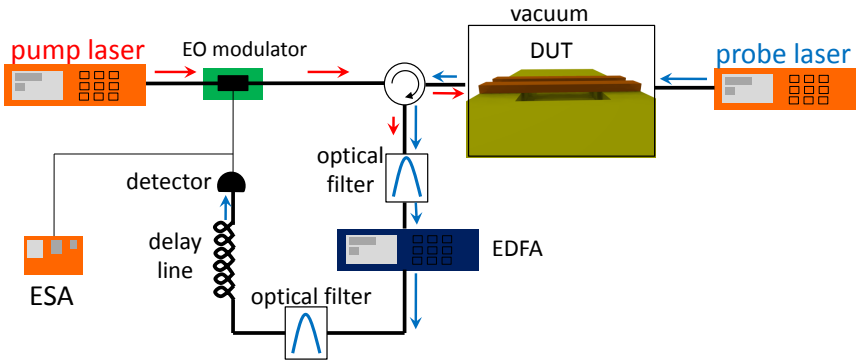

Figure 6.3: Experimental pump-probe set-up with feedback loop and enhanced detection scheme. The devices are placed in a vacuum chamber to reduce air damping.

6.4 Experimental results

In order to obtain regenerative oscillations the gain in the feedback loop needs to be sufficiently high and the phase of the force needs to be set properly (see equation 2.45). The gain can be controlled through the optical power that is injected by the pump laser, the phase can be controlled by either the length of the feedback loop or the chosen pump wavelength. In order to analyze the influence of the different parameters we will each time keep two out of three parameters (pump power, delay length and wavelength) constant and vary the other.

6.4.1 Pump power

In first instance we established an attractive optical force (λ_{attr}=1552.4 nm, see Fig. 6.2b) and fixed the feedback loop delay length such that the optical force provided a maximum amplification. The vibration was then measured for different optical pump powers (Fig. 6.4). For an optical power of $-14\,dBm$ (estimated power at the device) we observe that the apparent mechanical Q (≈10300) has more than doubled compared to the case without feedback (≈4760). When the optical power is increased to $-9\,dBm$ (and $-4\,dBm$) we observe a strong amplification of the oscillations.

In this case the peak linewidth of the mechanical oscillation is much smaller than the minimum achievable resolution bandwidth of the electrical spectrum analyzer (10 Hz). In fact the measured peak shape is no longer Lorentzian but rather a convolution of the Lorentzian shape we wish to

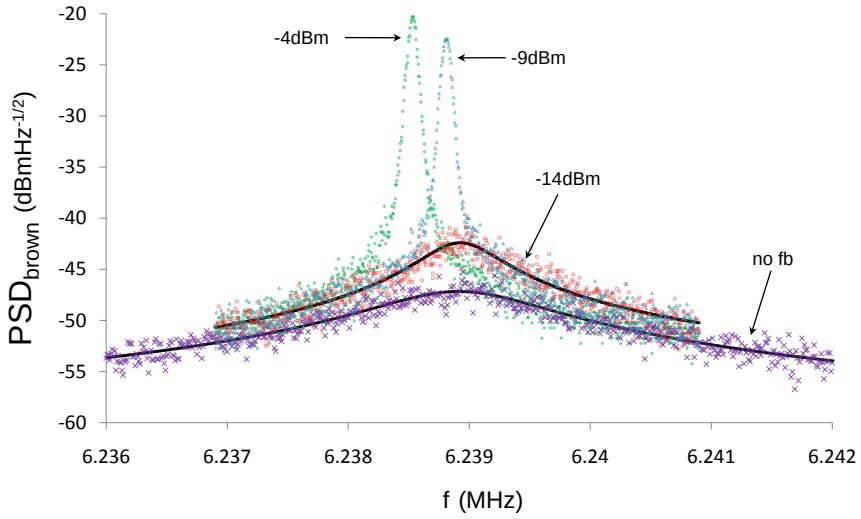

Figure 6.4: Feedback experiments for different optical pump powers (estimated power inside the device). The lowest (purple) trace (labeled 'no fb') originates from the thermal brownian vibration without any optical feedback force. When inserting $-14\,dBm$ in the device, the damping is more than halved and the apparent mechanical Q increases from 4760 to 10300 (values obtained through fits to a Lorentzian model). For higher optical feedback powers we observe strong, coherent oscillations. The measured responses are not Lorentzian because in fact we measure the Gaussian filter shape of the electrical spectrum analyzer. The black solid lines are fits to equation 2.47.

measure and the Gaussian shape of the electrical band pass filter from the electrical spectrum analyzer. Using this convolution model it is in principle still possible to fit a curve that matches the experimental data. However we found that such a fit does not permit a reliable extraction of the linewidth. We can only conclude safely that the linewidth must be much smaller than 10 Hz.

In principle taking a sufficient amount of samples in the time domain and performing a discrete fourier transform would allow to determine the peak width more accurately. The finitude of the time trace would cause the final result of the discrete fourier transform in the frequency domain to be convoluted with a sinc^2 window function with a 3 dB bandwidth of approximately $1.2\,\frac{f_s}{N}$ where f_s is the sampling frequency (needs to be at least twice as large as the mechanical resonance frequency according to the Nyquist sampling theorem) and N the number of samples. In order to resolve the Lorentzian peak the $sinc^2$ bandwidth needs to be smaller than the spectral width of the Lorentzian peak ($FWHM_{1.5dB}$) [7] so ($1.2\,\frac{2f_{mech}}{N} < 1.2\,\frac{f_s}{N} < FWHM_{1.5dB}$). From this we can derive a condition for the required number of samples in function of the mechanical Q: $2.4\,Q < N$. However implementation of this solution was not possible within the time frame of this work.

6.4.2 Delay length

In 6.5 the results of an experiment for different delay lengths in the feedback loop are shown. The pump wavelength (λ_{attr}=1542.2 nm for attractive force) and optical pump power are kept constant here. The length of the feedback loop was altered in steps of 5 ns until we found maximum damping (Q≈180, curve labeled '85 ns delay'). The damping is increased over a factor of almost 16 (initial Q=2900). In this case the optical force can be seen as an additional damping, which adds to the intrinsic damping of the system. Shortening the feedback loop with 85 ns corresponds approximately to a phase shift of π (mechanical oscillation period ≈168 ns). The exerted optical force is now subtracted from the intrinsic damping and consequently strongly amplified motion is found (curve labeled 'negative damping').

6.4.3 Wavelength tuning

Finally we show that in the proposed structure wavelength tuning can also be used to switch between the damping and amplifying regimes (Fig. 6.6). Again we set the delay length in order to achieve maximum damping for a

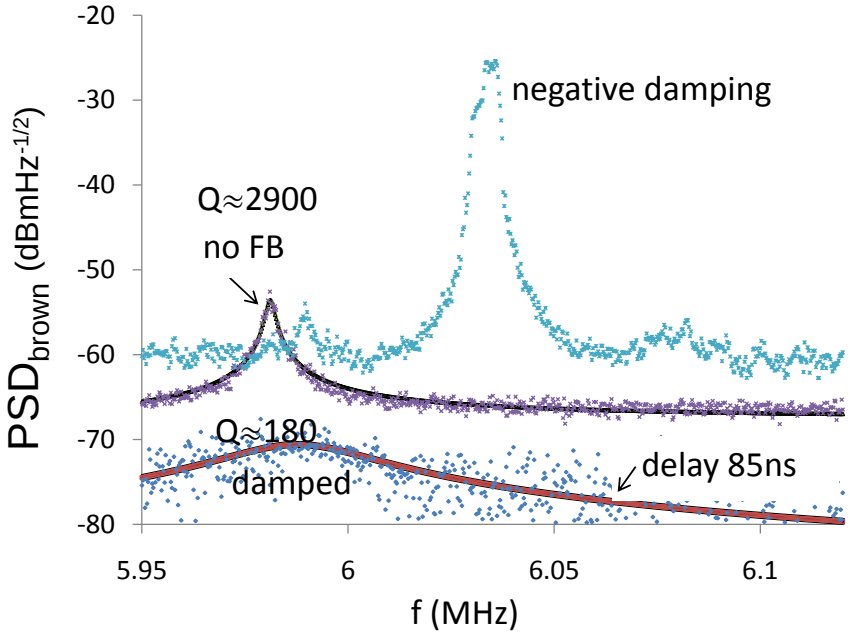

Figure 6.5: Feedback experiments for different delay lengths in the feedback loop. The length of the feedback loop was set to achieve maximum damping for λ_{attr}=1542.2 nm (Q≈180, curve labeled '85 ns delay'). The damping increased with a factor of 16 compared to the case without feedback (initial Q=2900). Shortening the feedback loop with 85 ns retrieved strongly amplified motion (curve labeled 'negative damping').

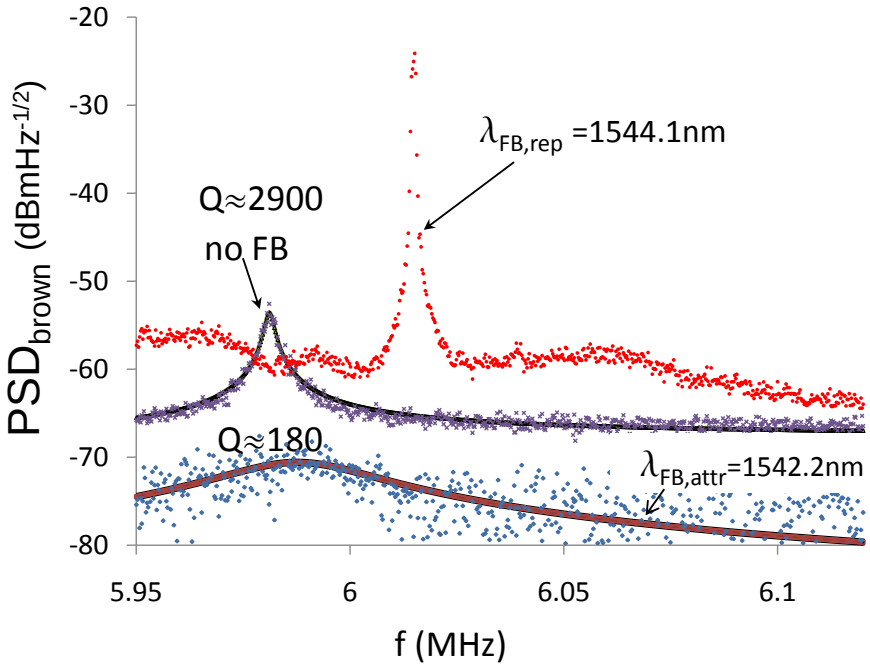

Figure 6.6: Simple wavelength tuning allows to switch from the damped regime (curve labeled 'λ_{attr}=1542.2 nm') to the regime of parametric instability (curve labeled 'λ_{rep}=1544.1 nm').

purely attractive force (curve labeled '$\lambda_{FB,attr}$=1542.2 nm'). Simple switching of the pump wavelength to 1544.1 nm (see Fig. 6.2b) is sufficient to get access to the regime of parametric instability (curve labeled '$\lambda_{FB,rep}$=1544.1 nm').

For all feedback experiments presented here also shifts of the resonance frequency were observed (see Fig. 6.4, 6.5 and 6.6). They might be related to the fact that the feedback force is not purely acting as a damping force, but also causes an optical spring force component.

Summarizing this chapter we have shown amplification and cooling of micromechanical oscillators by means of active optomechanical feedback. We demonstrated switching between the amplification and cooling regime by simple pump wavelength tuning. Integrated micromechanical oscillators might be a first step towards practical applications.

Bibliography

[1] T. J. Kippenberg and K. J. Vahala. Cavity optomechanics: Back-action at the mesoscale. *Science*, 321(5893):1172–1176, 2008.

[2] D. Kleckner and D. Bouwmeester. Sub-kelvin optical cooling of a micromechanical resonator. *Nature*, 444(7115):75–78, 2006.

[3] A. D. O'Connell, M. Hofheinz, M. Ansmann, Radoslaw C. Bialczak, M. Lenander, E. Lucero, M. Neeley, D. Sank, H. Wang, M. Weides, J. Wenner, John M. Martinis, and A. N. Cleland. Quantum ground state and single-phonon control of a mechanical resonator. *Nature*, 464(7289):697–703, 2010.

[4] M. Hossein-Zadeh and K. J. Vahala. An Optomechanical Oscillator on a Silicon Chip. *IEEE Journal of selected topics in Quantum Electronics*, 16(1):276–287, 2010.

[5] A. Vidic, D. Then, and C. Ziegler. A new cantilever system for gas and liquid sensing. *Ultramicroscopy*, 97(1-4):407–416, 2003.

[6] J. Tamayo, A.D.L. Humphris, A.M. Malloy, and M.J. Miles. Chemical sensors and biosensors in liquid environment based on microcantilevers with amplified quality factor. *Ultramicroscopy*, 86(1-2):167–173, 2001.

[7] J.-P. Martens. Signaaltheorie. Syllabus, UGent, 2003.

7 Conclusion and outlook

Uiteindelijk bereikt ook de slak de ark, niet waar? En weet, in de duisterste dagen kan je je nog steeds laven aan de borst van onze vriendschap.
Bram, Elewout, Koen, Marie, Wout (31 maart 2009)

7.1 Conclusion

THE work presented in this thesis is mainly focused on the exploration and demonstration of the optical gradient force as a novel actuation method for nanomechanical systems on a chip. We have first sketched the broad context in which this work fits: a general introduction on photonics, Micro-electro-Mechanical Systems (MEMS) and nanotechnology was given in chapter 1. We have explained that a powerful symbiosis between these fields exists and introduced the concept of Nano-Opto-Mechanical Systems (NOMS).

Since our main target reader group consists of electronic and photonic engineers a refresher on continuum mechanics is provided in chapter 2. In this chapter we have reviewed all the necessary concepts that are required to understand the mechanical aspects of our optomechanical devices.

The design and fabrication of nanophotonic passive structures in a silicon-on-insulator (SOI) wafer through Deep-Ultra-Violet lithography can be con-

sidered to be one of the core competences of the Photonics Research Group. A brief summary of this technology can be found in chapter 3. However since nano-optomechanical structures need to be freestanding (preferably with subμmeter gap sizes) some additional issues must be resolved. In particular critical-point-drying was presented as a solution for the stiction phenomenon. Stiction occurs during the drying cycle of fluids (e.g. wet etchants or rinsing water) that are in contact with the freestanding part of the device. It can cause the destruction of the device through unwanted sticking of the freestanding structure to a neighboring surface.

Accurate small displacement sensing in integrated optomechanical structures was discussed in chapter 4. We found that both index sensitivity and phase sensitivity are important parameters that govern the overall sensing performance. Index sensitivity describes how strongly the effective index of a certain waveguide type changes with displacement. We have investigated a few waveguide configurations (single-mode waveguide with substrate, slotted waveguide and a pair of parallel single-mode waveguides). We found that in the case of small gaps a field polarization that is parallel to the direction of movement is beneficial for sensitive motion detection. Phase sensitivity describes how efficient a (motion induced) phase change is translated into a (measurable) output power change of the transducer. This conversion is achieved by means of an optical resonator or interferometer. We concluded that optical resonators with high finesse are beneficial. By analyzing the dominant noise factors in the detection scheme we also found that preamplification of the optical probe signal prior to detection is highly beneficial in some cases.

Experimental results for the displacement sensitivity in the $fm\sqrt{Hz^{-1}}$ range were achieved. However our theoretical calculations show that there is still plenty of room for improvement (through smaller gaps, proper polarization). We also introduced the brownian thermal force in chapter 4. The thermomechanical noise in micromechanical oscillators allows for calibration of other forces. Hence we have defined a detection and calibration scheme for optical forces.

Subsequently in chapter 5 we discussed the main results of this work and demonstrated optical forces on a chip in various configurations: a slotted waveguide in a cavity, an out-of-plane moving waveguide in a ring resonator and forces between parallel waveguides. In this last structure we also showed tuning between attractive and repulsive forces by simple pump wavelength tuning. We pointed out a remarkable correlation between ef-

fective optomechanical actuation and sensitive motion detection.

Finally in chapter 6 we demonstated a system with active optomechanical feedback. In this scheme the recorded vibration is fed back to the mechanical oscillator as an optical force. Both sensitive detection and efficient actuation are required to establish a sufficiently strong feedback signal. Dependent on the sign of the feedback the thermomechanical motion can be damped or enhanced. In the latter case the regime of parametric instability might be reached. In this regime the feedback is sufficiently strong to overcome the intrinsic damping and strong coherent oscillations occur. We also showed that the control over damping and amplifying regimes could be controlled through simple wavelength tuning.

7.2 Outlook

For sure from the scientific point of view the future of optomechanics is undoubtedly very bright. Nobody can really predict whether the field of optomechanics will produce some commercial killer applications, but the scientific value is unquestionable. The remarkable convergence between nanoscale miniaturization in photonics and mechanics and the opportunities that arise from combining these fields are simply too disruptive to ignore. Not surprisingly the number of publications in the field is rapidly growing. As we have explained in chapter 1 optomechanics might open the door towards all kinds of fascinating quantum mechanics phenomena. However on the shorter term also practical applications might not be out of reach (see section 1.3.2). Especially in applications where GHz mechanical oscillators are desired (e.g. mass sensing, reference oscillators and filters) optomechanics might save the day. The unprecedented displacement sensitivity and actuation efficiency that potentially could be established within nano-optomechanical structures might provide the key to overcome the dramatically increasing stiffness in high frequency oscillators (stiffness increases quadratically with mechanical frequency).

The findings presented in this work have set the trail for a new class of nanophotonic structures, interacting with each other through light induced forces. Whether integrated optomechanical devices will be as successful and disruptive as their integrated electrical counterparts (Micro-electro mechanical systems) is an exciting question to be answered in the next decade.